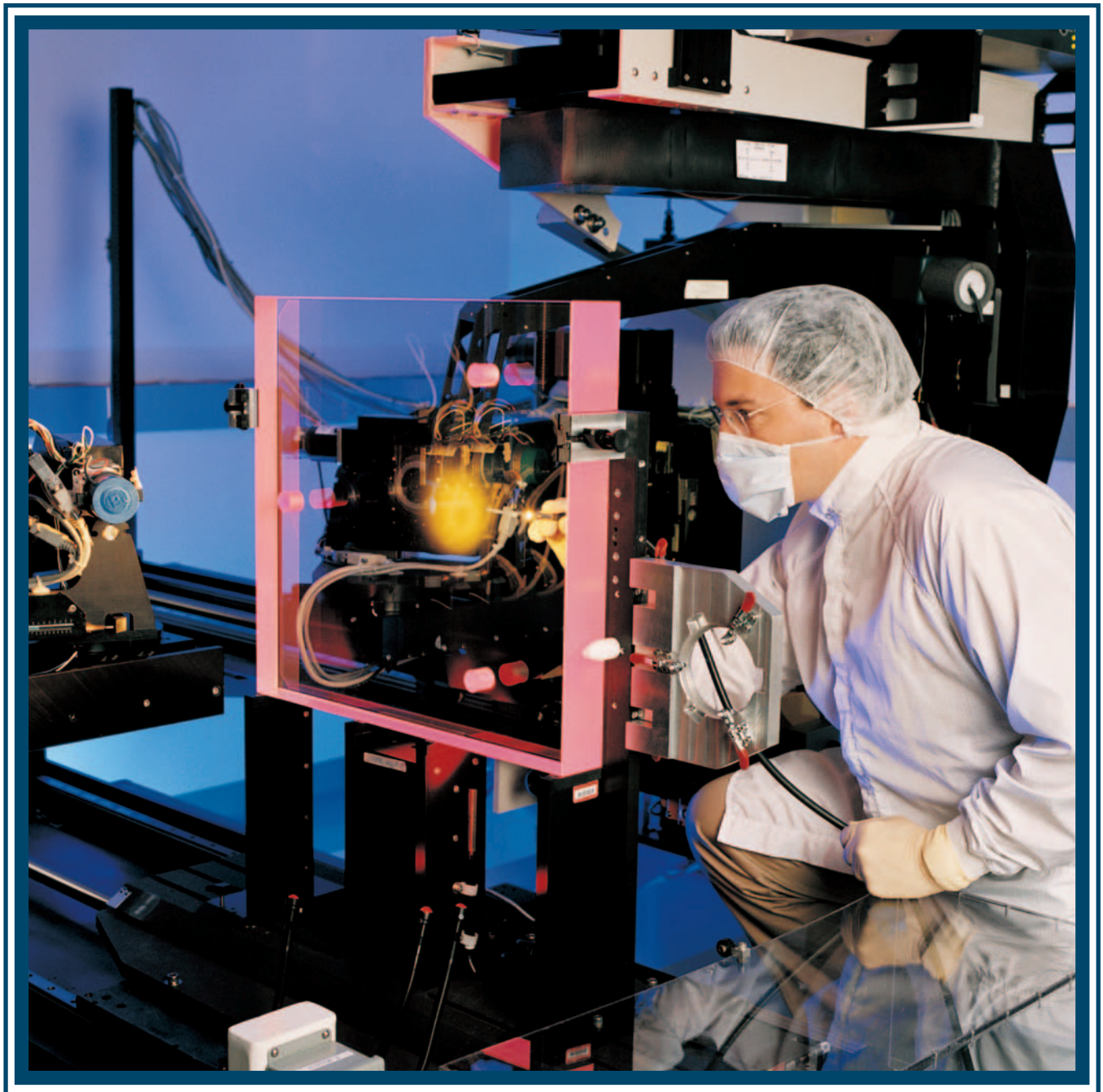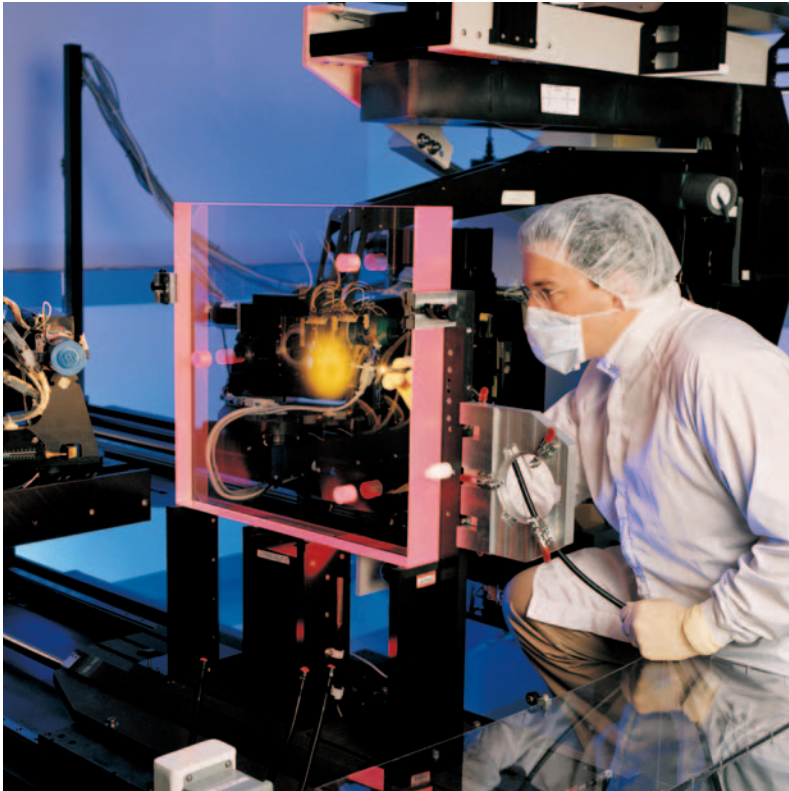# LLE Review

Quarterly Report

UR
LLE

About the Cover:

Multilayer coatings on large substrates with increasingly complex spectral requirements are essential for a number of optical systems, placing stringent requirements on the error tolerances of individual layers. This issue features an article (p. 67) describing the method used to deposit highly uniform thin-film coatings on nearly meter-sized optical substrates appropriate for the National Ignition Facility (NIF). Both the cover photo and the photo to the left show Research Engineer James Oliver inspecting a NIF LM7B mirror on the LLNL-supplied Bauer photometer. This instrument maps transmission and reflection of an optical component over its clear aperture for a given angle and polarization for the standard NIF operating wavelengths (1053, 527, and 351 nm). When measuring an appropriately designed optical coating, the photometer may be used to create a high-resolution, low-noise map of film-thickness nonuniformities.

For questions or comments, contact Mark J. Guardalben, *Editor*, Laboratory for Laser Energetics, 250 East River Road, Rochester, NY 14623-1299, (585) 275-3418.

Worldwide-Web Home Page: http://www.lle.rochester.edu/

LLE Review

Quarterly Report

UR
LLE

Contents

In Brief

This volume of the LLE Review, covering January–April 2003, features "Optimization of Deposition Uniformity for Large-Aperture NIF Substrates in a Planetary Rotation System" by J. B. Oliver and D. Talbot (p. 67). For the National Ignition Facility (NIF), coating thickness nonuniformity must not exceed 0.5% peak-to-valley over a 0.85-m aperture. This article describes the design and performance of a thin-film-deposition system used to produce multilayer dielectric thin-film coatings with highly uniform thickness over a full NIF aperture. By using a theoretical model to optimize deposition parameters, uniformity measurements performed on a mapping laser photometer demonstrate nonuniformities of 0.45% over a 0.89-m aperture, after discounting a roll-off effect that may be eliminated by modification of the coating tooling. This result significantly exceeds the uniformity requirement for the NIF coatings.

Additional highlights of research presented in this issue include the following:

- C. Stoeckl, R. E. Bahr, B. Yaakobi, W. Seka, S. P. Regan, R. S. Craxton, J. A. Delettrez, R. W. Short, J. Myatt, A. V. Maximov along with H. Baldis of LLNL (p. 76) use multiple OMEGA laser beams to study the two-plasmon-decay instability, which is the predominant source of suprathermal electrons in direct-drive inertial confinement fusion experiments. The authors show for the first time that the total overlapped intensity governs the scaling of the suprathermal-electron generation regardless of the number of overlapped beams, in contrast to conventional theories that are based on the single-beam approximation.

- R. Epstein (p. 81) examines the classical Rayleigh–Taylor instability of the interface separating two homogeneous inviscid fluid layers undergoing uniform acceleration, giving particular attention to the effects of uniform isentropic compression of the fluids and geometrical convergence of the interface and to the role of these effects in the implosion of inertial confinement fusion (ICF) capsules. The formulation presented makes a formal distinction between perturbation behavior under acceleration and perturbation behavior as modified by compression and by convergence of a cylindrical or spherical interface.

- K. Anderson and R. Betti (p. 91) develop the theoretical basis for laser-induced adiabat shaping in ICF spherical targets by a technique referred to as "relaxation." In this approach, the density profile of the capsule's shell is shaped using a weak prepulse followed by a main pulse with a high-intensity foot. The required laser pulse shape is easier to implement on current laser systems than the alternate technique described in the article. Rayleigh–Taylor growth rates are reduced without significantly degrading 1-D capsule performance.

- S. G. Lukishova (The Institute of Optics) and A. W. Schmid (LLE) along with A. J. McNamara, R. W. Boyd, and C. Stroud, Jr. of The Institute of Optics (p. 97) demonstrate the operation of a single-photon source—a key hardware element of quantum information technologies—via photon antibunching in the fluorescence of single terrylene molecules embedded in a cholesteric liquid crystal host. Planar-aligned cholesteric layers provide a one-dimensional photonic band gap, allowing an enhancement of the source efficiency.

- B. Yaakobi, T. R. Boehly, F. J. Marshall, D. D. Meyerhofer, R. Epstein, T. J. B. Collins, and D. Salzmann along with B. A. Remington and S. Pollaine of LLNL (p. 107) study the properties of compressed titanium due to laser-launched shocks by use of extended x-ray absorption fine structure (EXAFS). The EXAFS absorption spectrum is produced when backlighting a CH-coated Ti foil by the spectrally smooth radiation from a CH shell imploded on the 60-beam OMEGA laser system. Fitting an EXAFS model to the data indicates compression by a factor of 1.3, in agreement with shock-speed measurements and with hydrodynamic simulations. The rate of decay of the modulation with wave number is shown to include a significant contribution from static disorder, in addition to thermal vibration, due possibly to an α-Ti to ω-Ti crystal phase transition.

- Filling and cooling thin-walled (<3-μm) cryogenic capsules with deuterium–tritium fuel is a critical phase of operation for providing direct-drive targets. Permeation filling at room temperature to high pressures subjects the capsules to a buckling force. In addition, during cooling to 20 K, buckling and burst forces develop due to transient thermal gradients, thermal expansion differences, and changing permeability of the capsule wall. E. L. Alfonso, R. Q. Gram, and D. H. Harding (p. 118) quantify the forces on the capsule by modeling the thermal conditions inside the permeation cell. Results of cooldown cycles of OMEGA cryogenic targets agreed well with the simulation, and a cooling program was devised whereby the time for a capsule to reach the frozen state was reduced by 30%.

- A qualitative understanding of the greenhouse effect has long been available through models based on globally and time-averaged quantities. L. E. Schmidt (University of Rochester), H. L. Helfer, and R. S. Knox (LLE and University of Rochester) (p. 128) examine a simple 864-cell climatological model that reproduces yearly average temperatures obtained earlier from one of these global models and predicts a locally distributed nonradiative flux when observed temperatures are employed as input data. The model emphasizes vertical radiative energy transport within each cell and is a useful stepping stone for learning about radiative energy transfer into and out of Earth's atmosphere.

Mark J. Guardalben
Editor

Optimization of Deposition Uniformity for Large-Aperture NIF Substrates in a Planetary Rotation System

Introduction

Large substrates for precision optical applications require the accurate, uniform deposition of multilayer thin-film coatings. Typically, this results in the use of electron-beam evaporation in a "box-coater" configuration, utilizing either simple or planetary rotation of the substrates. Simple rotation of the substrate minimizes the size of the necessary coating chamber but generally results in films with nonuniformity of 2% or greater,[1] an unacceptable level for the precise requirements of the National Ignition Facility (NIF). Typical planetary rotation systems, containing four to five individual substrate holders, or planets, tend to produce relatively uniform coatings but would necessarily be quite large in order to process optics of a significant size. To process large optics for the NIF, a counter-rotating planetary geometry was developed and implemented in a 72-in. electron-beam deposition system.[2] Although this rotation system utilizes planetary motion to reduce the effect of deposition fluctuations, the large optic sizes relative to the overall chamber size and geometry result in coatings with a significant degree of nonuniformity if regions of the vapor plume are not masked.

To achieve the goal of producing optical coatings with nonuniformities of approximately 0.5% (peak-to-valley) over apertures of 0.85 m, a careful model needs to be constructed to account for deposition sources, planetary configuration, planetary gearing, and uniformity masking. The model assumes that the chamber and source conditions are quite stable throughout the length of the deposition, requiring a highly deterministic process. The process uses metallic hafnia for high-index layers and granular silica for low-index layers to produce coatings with exceptional resistance to high-peak-power laser irradiation.[3,4] The use of hafnium metal as an evaporant is ideal due to the smooth melt surface, the low occurrence of nodular defects in the growing film, and the stable chemical composition of the melt throughout the length of the deposition. Silica deposition tends to pose some difficulties, but its use is necessitated by the lack of a suitable substitute for precision laser coatings; electron-beam sweep parameters, deposition rate, and oxygen backfill pressure were optimized to minimize process variability.

Background

The uniform deposition of a thin film applied over a surface from a point or surface source can essentially be characterized as an illumination problem, with the appropriate type of source characterization. The theoretical equations governing the amount of material deposited on a given area have been well established;[5–9] therefore the results specific to a given chamber configuration simply become a summation of incremental thickness contributions as the planet position is indexed through the chamber. Since the system under study uses electron-beam sources, the source may be considered to be of the directed surface source type, with

$$t = \left(\frac{m}{\pi\mu} \right) \left(\frac{\cos\phi \cos\theta}{r^2} \right), \qquad (1)$$

where t is the thickness of the film deposited, m is the total mass of the material emitted from the source, μ is the density of the film being deposited, ϕ is the angle normal to the surface of the source, θ is the angle normal to the substrate surface, and r is the distance from the source to the point on the substrate under evaluation (see Fig. 94.1). However, since the primary concern is uniformity of the deposited film, once the summation is performed for all of the incremental planar positions, the relative thicknesses will be normalized over the surface of the substrates being coated. When the thicknesses are normalized, the constants in Eq. (1) will cancel, resulting in the simplified expression

$$t = \frac{\cos\phi \cos\theta}{r^2}. \qquad (2)$$

The geometry may be further simplified to reflect that the source surface is parallel to that of the surface being coated; such a condition would not be appropriate for a tilted-plant
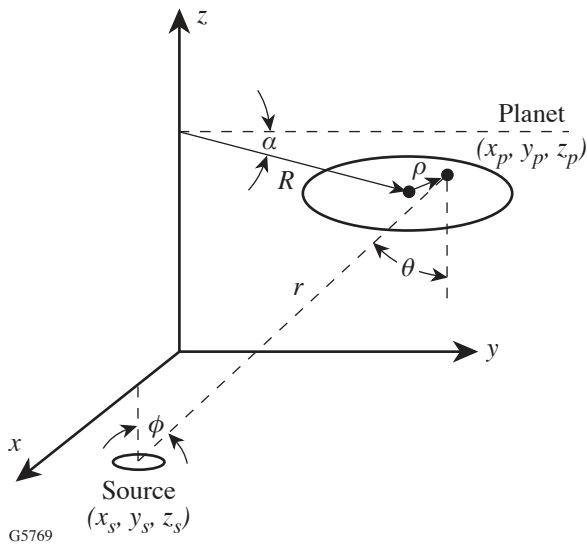
G5769

Figure 94.1
Basic planetary configuration as substrate undergoes rotations/revolution.

rotation but is applicable for a standard planetary with all surfaces being coated rotating in a plane. In this case,

$$t = \frac{\cos^2\theta}{r^2}. \tag{3}$$

This expression is appropriate for an ideal directed-surface source, but measurements of film uniformity indicate factors such as the form of the material being evaporated, the electron-beam sweep parameters, and the proximity of the source to the walls of the coating chamber possibly affecting the accuracy of this formula. In practice, the formula may be modified to[9]

$$t = \frac{\cos^n\theta}{r^2}, \tag{4}$$

where n is now a variable allowing the theoretical thickness distribution to be fit to that of the measured distribution. Converting this to coordinate geometry,

$$r = \sqrt{\left(x_p - x_s\right)^2 + \left(y_p - y_s\right)^2 + \left(z_p - z_s\right)^2} \tag{5}$$

and

$$\cos\theta = \frac{z_p - z_s}{\sqrt{\left(x_p - x_s\right)^2 + \left(y_p - y_s\right)^2 + \left(z_p - z_s\right)^2}}, \tag{6}$$

where the subscript "p" denotes the point on the planet and "s" denotes the source. Substitution and simplification then yield

$$t = \left\{ \frac{\left(z_p - z_s\right)^n}{\left[\left(x_p - x_s\right)^2 + \left(y_p - y_s\right)^2 + \left(z_p - z_s\right)^2\right]^{\frac{n+2}{2}}} \right\}. \tag{7}$$

The coordinates of the source(s), as well as the height of the substrates, will be measured quantities to be inserted into the deposition model. The x and y coordinates of a given point being tracked in the planetary must be calculated, based on Fig. 94.1. Given the relation as shown, the primary factor in determining the motion of a point on the planet will be the relative angular rotation of the planet to that of the revolution of the system, which is simply a function of the relative gear sizes for the solar and planet gears. This will be explored in greater detail later, but the motion of a point on the planet undergoing planetary rotation will trace out the path described by

$$x(\alpha) = R\cos\alpha + \rho\cos\left(\frac{\alpha N_s}{N_p}\right) \tag{8}$$

and

$$y(\alpha) = R\sin\alpha + \rho\sin\left(\frac{\alpha N_s}{N_p}\right), \tag{9}$$

where R is the radius of the planet orbit, ρ is the radial position of the point on the planet, α is the angular position of the planet in its orbit, and N_s and N_p are the number of teeth on the solar and planet gears, respectively. Since the planets are rotating in-plane, z_p will remain constant and the thickness contribution at any point in the planetary motion can now be calculated as a function of only α. A summation of the individual contributions throughout a number of revolutions, where α is incremented from 0 to 2π, and for a range of ρ from the center to the edge of the planet, will provide an overall uniformity distribution over the surface of the planet.

Coating efficiency is also of interest when configuring the planetary rotation system since configurations can be conceived that provide nearly ideal uniformity, but due to signifi-

cant offsets of the source from the center of rotation or excessive distances between the substrate and the source, the percentage of vaporized material condensing on the substrates is negligible. Therefore, since the desired result is to achieve a high degree of film uniformity while maximizing source material utilization, it is necessary to calculate the percentage of evaporated material being deposited on the substrate.

The motion of a typical planetary rotation describes an annulus in the plane of rotation since the planets orbit at a constant radius without crossing the center of the chamber. Since the planets in the counter-rotating configuration cross the center of the chamber, a disk replaces the annulus and the efficiency becomes the percentage of deposited material within this disk. The efficiency with which evaporated source material is used is equal to the integral of Eq. (4) over the area defined by the disk, divided by the integral of Eq. (4) over the hemisphere above the source, i.e., the range of θ from 0 to $\pi/2$. The integration over a hemisphere is straightforward, resulting in a normalization value of π:

$$\text{Efficiency} = \frac{1}{\pi} \int_{\substack{\text{over} \\ \text{disc}}} \int \frac{\cos^{n+1}\theta}{r^2} d\gamma \, d\theta. \tag{10}$$

The integration of an off-axis source, as shown in Fig. 94.2, is transformed to that of an on-axis source in order to easily and accurately express the limits of integration. Performing the transformation, the efficiency of the source is found to be

$$\text{Efficiency} = \frac{1}{\pi} \int_0^{2\pi} \int_0^{R+\rho_{max}}$$

$$\frac{h^{n+1} \, r' \, dr' \, d\gamma}{\left[r'^2 + 2r'D\cos\gamma + h^2 + D^2 \right]^{\frac{n+3}{2}}}, \tag{11}$$

where n is the exponent of the cosine as in Eq. (4), ρ_{max} is the maximum radial extent of the planet, and all other variables are as shown in Fig. 94.2. The efficiency can then be calculated for a range of source offsets for a given plantary geometry. The results of these efficiency calculations are shown for the counter-rotating geometry in Fig. 94.3.

G5771
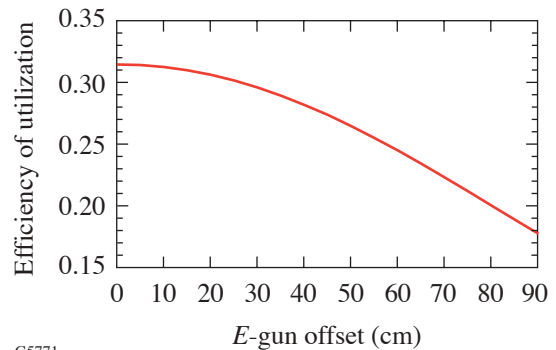
Figure 94.3
Efficiency of material utilization as a function of the offset of the source from the center of the coating chamber. An offset of 0 is for source location $(0, 0, z_s)$ in Fig. 94.1, with increasing offsets representing the movement of the source along the x axis. While there is a significant reduction in the efficiency of the material being evaporated, the reduction in the size of secondary masking may offset this loss.

G5770

Figure 94.2
Deposition efficiency is calculated by transforming the source location to a position on-axis with the rotation and integrating over the maximum area described by the planetary motion, a disk with radius $R + \rho_{max}$.

The efficiency of material utilization may be somewhat misleading since this considers only whether the material is available for use, not where the material would condense on the substrate and its impact on the film uniformity. To make an informed analysis of the actual material utilization, one must take into account any masking required to achieve a uniform deposition.

Measurement of Film Uniformity

Many different coating designs are required for the NIF, but all use the same evaporant materials with layer deposition times greater than 4 min, with a planetary revolution period of approximately 6 s. Therefore, the uniformity of the deposition process will be qualified for NIF specifications, assuming the deposition of similar layers will not deviate substantially from the measured uniformity.

To improve film uniformity, it is first necessary to accurately measure the achieved uniformity. A large-aperture scanning laser photometer installed at LLE is capable of mapping transmission and reflection performance of a NIF-sized (525 × 807-mm) optic (Fig. 94.4). Since this instrument measures photometric performance at a single wavelength, it is necessary to develop a correlation between transmission of the coating and film uniformity. Furthermore, to increase the accuracy of the measurement, the transmitted light should be highly sensitive to thickness nonuniformities, with a maximum range of transmitted light.

G5772

Figure 94.4
Scanning laser photometer at LLE. This system is capable of simultaneously measuring % T and % R over a 525 × 807-mm aperture, from 8° to 60°, at wavelengths of 1053, 527, and 351 nm. Results are presented as a 2-D intensity map of the surface, digitized to pixels of 1 to 5 mm.

A modified quarter-wave reflector was designed such that the edge of the reflectance band is approximately linear with respect to wavelength (Fig. 94.5). Since the photometer operates at 1053 nm, a slope of 1% T per nanometer correlates to a relationship of 1% T per 0.1% thickness nonuniformity. When a large coated substrate is then mapped on the photometer, changes in transmittance will indicate the shifting of the spectral performance of the coating to the left or right in

Fig. 94.5, for higher or lower values of % T respectively. If the slope of the reflectance band is verified on a spectrophotometer, the precise correlation of transmittance to thickness change can then be established for a given coating deposition since the percent wavelength shift of the coating performance will be equal to the percent change in coating thickness. This is typically adequate for initial uniformity efforts, although further reduction of nonuniformity may require coatings that have a more steeply sloped transmission profile and therefore are more sensitive to slight film nonuniformities.
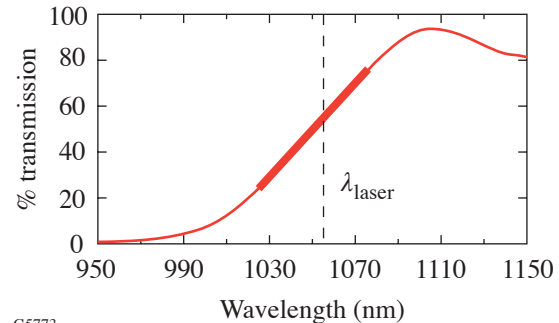
G5773

Figure 94.5
Modified quarter-wave reflector with linear transmission with respect to wavelength over the range $\lambda_0 \pm 2\%$. Provided the coating is deposited properly and all nonuniformities are less than 4% peak-to-valley, the resulting photometer transmittance map will directly correlate to film-thickness uniformity.

Planetary Gearing

The essence of a planetary rotation system in a vacuum coating chamber is that the substrate holder, or planet, will undergo planetary motion by rotating about its center axis while revolving about the center axis of the coating chamber. The planet will continue to move through the vapor plume of the evaporation source in this manner, allowing the deposited film thickness to become more uniform by averaging the different regions of the plume incident on each portion of the planet. The most basic system is a two-gear system, as depicted in Fig. 94.1. The center "solar gear" remains stationary, and the outer "planet gear" rotates while revolving about the center of the system.

Many thin-film-uniformity calculations assume that a sufficient number of revolutions take place during a layer deposition that the calculations of thickness uniformity can be reduced to an integration over the planet radius,[7] with the corresponding assumption that the film is "perfectly uniform" for constant planet radius. This would mean that all film nonuniformity would be only in the radial direction in a polar coordinate

system. In reality, the relative sizes of planetary and solar gears are critical to achieving high degrees of thickness uniformity. If the solar gear has a number of teeth equal to "N_s," and the planet gear has a number of teeth equal to "N_p," then the gear ratio is given by

$$\text{Gear ratio} = \frac{N_s}{N_p}. \tag{12}$$

This gear ratio determines the number of rotations the planet will make for each revolution of the planetary fixture, causing each point on the planet to trace out a cycloid during each revolution based on Eqs. (8) and (9). Beginning with the simplest case of a gear ratio equal to 1, it is apparent that successive revolutions of the planetary will trace identical circles since each revolution of the planet also corresponds to a single rotation; this eliminates the benefit of planetary motion since a given point will travel an identical path through the vapor plume, failing to average differing plume conditions [Fig. 94.6(a)]. Typically, the gear ratio is not equal to 1, but instead, due to planetary geometry, $N_s > N_p$. If the gear ratio is an integer greater than 1, identical cycloids will be traced out for each successive revolution, severely limiting the degree of random motion [Figs. 94.6(b)–94.6(f)]. It has been known for some time that the gear ratio must be non-integral,[5] such that the cycloid traced out is no longer a closed figure and therefore will not be repeated with each successive revolution.

(a) Ratio = 1   (b) Ratio = 2   (c) Ratio = 3

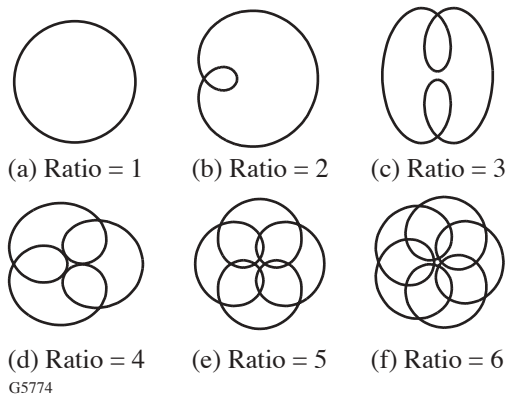(d) Ratio = 4   (e) Ratio = 5   (f) Ratio = 6

G5774

Figure 94.6
Cycloids traced out by an off-center point in a planetary rotation after one revolution with different integral gear ratios. Note that all figures are closed, requiring that the point will trace out an identical path for all successive revolutions.

The limitations on this next level of randomization can also be expanded by examining how quickly a given cycloid will be repeated. If the gear ratio is non-integral, this indicates that

the planet will not reach its starting angular orientation at the conclusion of one revolution of the planetary. Therefore, the cycloid traced out by the previous revolution cannot be repeated in the next revolution since the revolution did not trace out a closed figure. Each successive revolution will provide an opportunity for the planet orientation to achieve its starting position and therefore repeat its path through the vapor plume. The path will not repeat until

$$m\left(\frac{N_s}{N_p}\right) = \text{ an integer} \quad m = 1, 2, 3, \ldots, \tag{13}$$

where m is the number of revolutions of the planetary, since this represents an integral number of rotations of the planet and therefore closes the figure traced by the cycloid. Since N_s and N_p are both integers, the maximum possible number of revolutions before the system repeats is $m = N_p$. In the event that N_p and N_s have common factors, the ratio simplifies and repetition of the path through the vapor plume will occur at

$$m = \frac{N_p}{g}, \tag{14}$$

where g is the greatest common factor of N_p and N_s.

The previous condition requiring no common factors is sufficient to establish unique paths through the vapor plume, but again it is insufficient to minimize film nonuniformities in practice. Since the maximum number of paths is equal to N_p, every path will be used exactly once only for those layers of the appropriate thickness such that the deposition time is equal to N_p multiplied by the period of revolution of the planetary, or an integer multiple thereof. In practice, this condition is rarely if ever met due to variations in deposition rate, design layer thickness, and material being deposited. In this event, paths that are similar to one another are sufficient to cause greater degrees of nonuniformity, and the fewer the number of revolutions of the planetary, the greater the observed impact on uniformity. If the angular orientation of the planet is tracked and plotted at a fixed point in the revolution, such as the center of the door of the chamber, it can be shown how the paths relate to one another. As shown in Fig. 94.7 for the given values of $N_s = 237$ and $N_p = 71$, the planet starts with the arrow denoting its orientation at 0°. After one revolution, the planet has undergone 3 full rotations plus an additional partial rotation, resulting in a change in orientation of 121.69°. After the second revolution, the planet will again have undergone 3 complete rotations plus an additional 121.69°, resulting in an orientation

of 243.38°. The third revolution will nearly return the planet to its starting orientation, differing only by 5.1°. This will repeat for successive revolutions such that, for the given configuration, every 3 revolutions the planet will return to almost the same orientation. The graphs in Fig. 94.8, I(a)–I(c), plot the angular orientation of a planet as a function of the number of revolutions the planetary has undergone for different gear configurations. Tracking the planet in such a manner, it is possible to see that the planet assumes approximately the same angular orientation every 3 revolutions for configuration (a), every 4 revolutions for configuration (b), and every 13 revolutions for configuration (c). The graphs labeled II(a)–II(c) show the path traced by a point on the planet through 30 revolutions of the planetary rotation. Especially when depositing thin layers, this near-repetition is evident in the symmetry observed in the measured film uniformity. The surface plots in Row III of Fig. 94.8 provide experimental evidence of rotational nonuniformity due to inappropriate gearing, and 3-, 4-, and 13-way symmetries are apparent in the measured film thickness. As higher degrees of symmetry are reached, it becomes much more difficult to resolve these effects and the uniformity is significantly improved.

Uniformity Masking

Once a stable deposition system has been configured, with optimized planetary gearing, the residual thickness non-uniformities can be removed through the use of masking. Most planetary rotation geometries will result in the center of the planet having a thicker film deposited than the periphery; therefore the mask will be required to obscure a greater percentage of the center each revolution. There are multiple methods of masking the vapor plume, including large masks rotating in the opposite direction as that of the planetary,

G5793

Figure 94.7
Relative planar orientations versus revolutions of the planetary rotation. Every 3 revolutions, the planet assumes almost the same angular orientation, differing only by 5.1°.

G5775
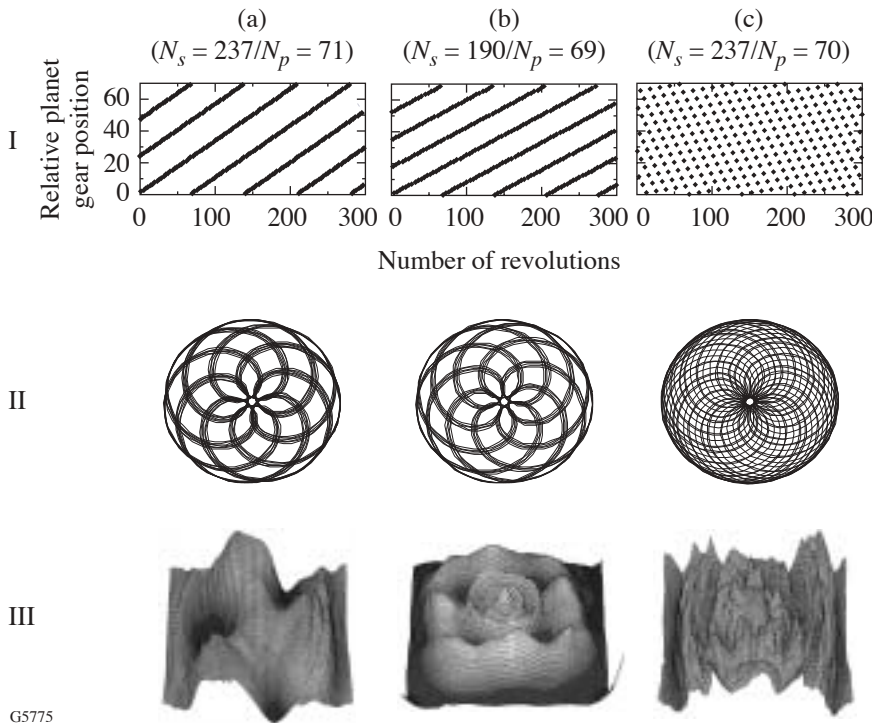
Figure 94.8
Comparison of the effects of different planetary gear ratios. The graphs in Row I track the angular orientation of a planet each time it passes a fixed point in the chamber, such as the center of the door, as a function of the number of revolutions of the planetary. Since a geared system is being analyzed, the possible angles correspond to a specific gear tooth number. Row II depicts the path of an off-center planetary point through 30 revolutions of the planetary. Row III depicts the measured film uniformity pattern on the mapping laser photometer. Gearing configuration (c) provides a greater degree of randomization through the vapor plume, yielding significant improvements in film uniformity.

individual masks for each planet that are rotated with the planetary, and fixed-position uniformity masks. The fixed-position masking is the lowest-maintenance, highest-mechanical-reliability system so is therefore preferred, provided it is capable of meeting the nonuniformity requirements of the coatings. A critical aspect of this masking system is the proper mounting of the masks in the coating chamber; the masks must be placed precisely in the position defined by the model, using a mounting structure that is stable and repeatable and that takes thermal expansion into account if the effect on mask placement warrants. Small changes in the mask shape can have a significant impact on the film uniformity, and care must be taken to avoid changes due to poor mounting.

A model was created to sum thickness contributions over the aperture of a planet as it undergoes planetary rotation, according to Eqs. (4)–(9) above. The model accounts for the motion of the planet due to the gearing and relies on plume shape fitting by varying n in Eq. (4). Masks are projected onto the plane in which the planet surface moves, providing a binary multiplier to the thickness contribution at that point. Mask shapes are determined by evaluating the film distribution and altering the mask width as needed at the appropriate radii in the planetary.

We have found that the optimal mask shapes for a standard planetary rotation system have a very smooth, continuous shape, providing minimal difficulty in manufacture, installation, or usage; this also results in an absence of high-frequency, high-gradient thickness changes. The primary focus of this work, however, was to improve uniformity over a large-aperture optic for the NIF laser system suspended in a counter-rotating planetary, as shown in Fig. 94.9. The fact that the optic crosses the center of the coating chamber, and may experience masking effects intended for a different radius on the optic, poses significant challenges in creating a suitable mask shape. In spite of this, the basic model is identical to that used for a standard planetary system, although the aperture over which the coating must be uniform is significantly larger.

The source placement and characteristics have a significant impact on the uniformity of the film thickness prior to the use of masking. As shown in Fig. 94.10, changes in the source placement can vary the degree of nonuniformity over a range of 17.6% to 2.4% for source positions of 0 to 90-cm offset from the center of the planetary, respectively, for a 90-cm-aperture optic in the counter-rotating planetary. Exact performance will be highly dependent upon the geometry of the particular planetary rotation. A source offset of 90 cm was the maximum considered since this would correspond to placing the source in the corner of the 72-in. coating chamber. Some of the standard arguments against placing the source a significant distance off-center in a planetary include the following:

1. The material utilization of the source will be significantly decreased.
2. The chamber walls will influence the vapor plume, causing undesirable effects.
3. The higher angles of the vapor plume, which are more erratic, will be used, resulting in reduced consistency of the uniformity.

G5789

Figure 94.9
Mask configuration implemented in a 72-in. coating chamber for a counter-rotating planetary. Multi-point quartz crystal monitoring is installed in the mask mounts, providing six thickness/rate measurements.
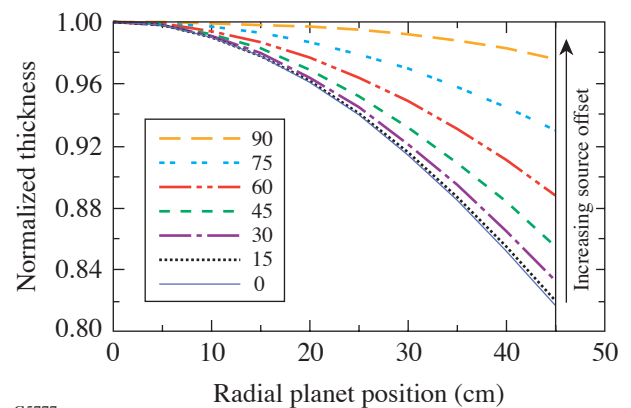
G5777

Figure 94.10
Theoretical uniformity of film deposition over the radius of the planet versus offset of the source position from the center of the coating chamber, for z_p–z_s = 1200 mm, R = 391 mm, and n = 1.6. By minimizing the nonuniformity of the deposited film, the degree of secondary masking may also be minimized.

While the material utilization is decreased, as shown in Fig. 94.3, the decrease in the amount of masking required to produce a uniform deposition results in an equivalent, or even improved, material utilization once the masked configuration is considered. Wall effects are possible, but it was decided to proceed with the configuration change and experimentally determine if this effect is significant. As demonstrated in the uniformity results shown below, as well as by laser-damage testing, the influence of the wall proximity was not an issue. As for the possibility of increased sensitivity, thickness uniformity was modeled for differing plume shapes once a masked configuration was developed for different radial offsets of the source. The model indicates that the uniformity is actually more stable for the source positions that are farther off-axis in the planetary, as shown in Fig. 94.11.

G5778

Figure 94.11

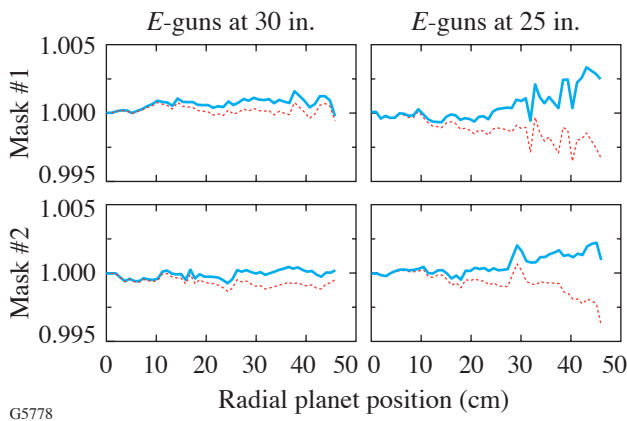Theoretical influence of source offset on the sensitivity of film uniformity to changes in the vapor plume distribution. Source distribution modeled as $\cos^{1.6}\theta$, with n varying ±0.2. Two significantly different mask designs are modeled, each with two source offsets, showing that the greater source offset is actually less sensitive to variations in the vapor plume.

Results

Uniformity masks have been produced for a number of different chamber configurations, and the experimental results have been mapped on the scanning laser photometer. First, a value of n in Eq. (4) is assumed in the model, appropriate masking is designed to correct the thickness nonuniformities, and a deposition is performed on a large-aperture substrate. The transmittance is then mapped on the laser photometer, the correlation of transmittance to thickness is determined based on a spectral measurement at one point in the planet, and the resulting nonuniformity is calculated. In order to improve

upon this result, the variable n must now be adjusted to best-fit the model to the experimentally determined nonuniformity. All other quantities, such as the source and substrate locations, mask shapes and locations, and planetary gearing, are physically measured quantities known to a high degree of precision. Once the model accurately predicts the results achieved, the model may be used to redesign the masks to correct the remaining nonuniformities, repeating the process until the degree of nonuniformity is acceptable. Typically, deviations in the best-fit process were found to be less than 0.1% except at the extremes of the substrates, where variations could reach 0.15%. Figure 94.12 illustrates the nonuniformity achieved for a 24-layer coating with layer thicknesses of approximately $\lambda/4$ at 900 nm in a 72-in. counter-rotating planetary. Edge roll-off is evident in the data due to shadowing of the coating tooling along the edges of the substrate. Typical model performance has yielded nonuniformity of less than 1% over the aperture of interest in one to two masking iterations. The primary goal—to achieve good uniformity over a full NIF aperture—was completed in two mask iterations, with a final film nonuniformity of 0.45% peak-to-valley, after removal of roll-off. Correction of tilt in the planet would allow this to be further reduced to 0.30%; while this is a 33% reduction in the nonuniformity, it is relatively insignificant compared to optic specifications, and the necessary modifications cannot be justified.

Conclusions

Highly uniform thin films for large-aperture, high-precision optical coatings have been deposited with stationary masking and planetary rotation utilizing the two-gear, counter-rotating configuration. Impacts on nonuniformity due to planetary gearing have been measured, the causes investigated, and appropriate corrections applied to minimize rotational non-uniformities in film thickness. The model developed has been shown to be effective in designing suitable masks to correct thickness nonuniformities. While further improvements are certainly possible through the use of rotating masks, friction-drive planetary rotation, or three-gear configurations, the simplicity and reliability of the current system make its continued use highly desirable. Furthermore, the results achieved significantly exceed the uniformity requirements for NIF laser coatings, despite the complexities of the counter-rotating planetary.

Further improvements to the uniformity masking model are planned in two primary areas: (1) a better description of the vapor plume to more accurately fit the measured results at higher angles and (2) automated optimization of the mask shape. The masking concept can also be further improved by

making the masks asymmetric, to account for differences in the shapes of the vapor plumes of the individual sources. The described configuration has been shown to work well for the deposition of layers >4-min duration, with a planetary period of approximately 6 s. It is expected that layers with significantly shorter deposition times will require higher planetary speeds or will necessitate the use of additional enhancements to the planetary/masking system, such as the use of rotating masks.

ACKNOWLEDGMENT

REFERENCES

1. I. C. Stevenson and G. Sadkhin, in *Proceedings of the 44th Annual Technical Conference of the Society of Vacuum Coaters* (Society of Vacuum Coaters, Albuquerque, NM, 2001), pp. 306–313.

2. D. J. Smith *et al.*, in *Proceedings of the 41st Annual Technical Conference of the Society of Vacuum Coaters* (Society of Vacuum Coaters, Albuquerque, NM, 1998), pp. 193–196.

3. B. Andre, L. Poupinet, and G. Ravel, J. Vac. Sci. Technol. A **18**, 2372 (2000).

4. R. Chow *et al.*, Appl. Opt. **32**, 5567 (1993).

5. B. S. Ramprasad and T. S. Radha, Thin Solid Films **15**, 55 (1973).

6. K. H. Behrndt, in *Transactions of the Tenth National Vacuum Symposium of the American Vacuum Society*, edited by G. H. Bancroft (The Macmillan Company, New York, 1963), pp. 379–384.

7. A. G. Zhiglinskiy and E. S. Putilin, Opt.-Mekh. Prom. **38**, 46 (1971).

8. H. A. Macleod, *Thin-Film Optical Filters*, 3rd ed. (IOP Publishing, Bristol, England, 2001), pp. 488–497.

9. A. Musset and I. C. Stevenson, in *Proceedings of the 31st Annual Technical Conference of the Society of Vacuum Coaters* (Society of Vacuum Coaters, Albuquerque, NM, 1988), pp. 203–209.

G5779

Figure 94.12
Film nonuniformity in both the counter-rotating and forward-rotating planets for a masked configuration with electron-beam sources at 76-cm offset from chamber center. Roll-off is evident along the length of the coating due to shadowing effects of the coating tooling. Discounting this effect, which may be eliminated by modification of the coating tooling, both uniformity maps exhibit 0.45% nonuniformity peak-to-valley. Furthermore, if the tilt evident in both surface plots is subtracted, since this is a result of the optic rotating out-of-plane, nonuniformity is reduced to 0.30%.

Multibeam Effects on Fast-Electron Generation
## from Two-Plasmon-Decay Instability

Two-plasmon-decay (TPD) instability has long been identified as a potential source for suprathermal electrons that can preheat the target fuel in direct-drive inertial confinement fusion (ICF) experiments, potentially impeding the assembly of sufficient fuel areal density for ignition.[1–4] TPD is a three-wave parametric instability in which an incident photon at frequency ω_0 decays into two electron-plasma waves (plasmons) with frequencies near $\omega_0/2$. Because of the resonant nature of this process, it is restricted to a small range of electron densities near the quarter-critical density. The instability threshold intensity is known to decrease and the saturation levels increase as the plasma density scale length increases.[5–8]

The basic theory of TPD was developed long ago[5,6] along with a number of numerical simulations;[7–13] however, experimental verification has been of a qualitative nature at best. Quantitative predictions for the suprathermal-electron generation are only now starting to emerge from simulations but have not yet been compared with experimental data.[13] Even though some experiments used multiple overlapping beams,[1] their analysis has always been made in the single-beam approximation. This was based on the belief that the single-beam intensity dominates the scaling of the TPD instability even in experiments with multiple overlapping beams.

This article presents for the first time clear evidence for strong overlapping-beam effects on suprathermal-electron generation in both spherical and planar experiments. TPD instability was found to scale predominantly with overlapped intensity, which is defined as the incoherent sum of the interaction-beam intensities. The single-beam intensity and the number of overlapped beams did not significantly affect the observed scaling. There are several characteristic signatures for TPD instability: $3\omega_0/2$ and $\omega_0/2$ emission in the scattered light,[4,14] a hard component (>20 keV) in the continuum x-ray bremsstrahlung spectrum,[15] an energetic tail in the suprathermal electron spectrum,[16] and K_α emission from cold material due to preheat.[17,18] On the OMEGA laser system[19] TPD instability is monitored using a $3\omega_0/2$ spectrometer and a time-resolved, scintillator-based, four-channel hard-x-ray detector

system.[20] The observed hard x rays can be attributed only to TPD instability since competing production mechanisms such as stimulated Raman scattering (SRS) are not seen in significant amounts in these experiments.[21,22] In addition, the electron temperatures inferred from the hard-x-ray signals are well above those measured for SRS,[23] and the $3\omega_0/2$ signature is seen in all of the reported experiments.

The experiments in spherical geometry used targets of varying diameters similar to those described in Ref. 24. Gas-filled CH targets (900- to 1100-μm diameter, ~27-μm wall thickness, and 20 atm of D_2 fill) were irradiated with 60 beams at 351-nm wavelength, with 1-ns square pulses and ~23-kJ total energy. All beams were smoothed by two-dimensional smoothing by spectral dispersion[25] with 1-THz bandwidth in the UV and polarization smoothing.[26] Standard OMEGA phase plates[27] were used throughout with a spot size of ~0.5-mm FWHM and a speckle-averaged peak intensity of ~2×10^{14} W/cm^2. The total overlapped intensity on target varied between 6.0×10^{14} W/cm^2 and 8.5×10^{14} W/cm^2, due to the varying target surface area, while the peak single-beam intensity on target was virtually unchanged. One-dimensional *LILAC*[28] hydrodynamic simulations show a rapidly growing radial density scale length at a quarter-critical density that reaches ~100 μm midway through the pulse. This is followed by a slower growth to ~150 μm at the end of the pulse. The coronal electron temperature is predicted to be relatively constant, with a typical value of ~2.5 keV. Figure 94.13 shows the hard-x-ray and $3\omega_0/2$ signatures of the TPD instability from the spherical experiments as a function of overlapped intensity. The suprathermal-electron temperature as inferred from the hard-x-ray spectrum[20] changes very little, which is consistent with earlier observations.[2,3] In contrast, the measured hard-x-ray energy scales exponentially with overlapped intensity as exp ($I_{14}/1.2$), where I_{14} is the intensity in units of 10^{14} W/cm^2. This behavior strongly suggests that the TPD instability in the OMEGA implosion experiments scales primarily with the overlapped intensity rather than the single-beam intensity. Even though the overlapped intensity varies by only 30%, the hard-x-ray signature from the suprathermal elec-
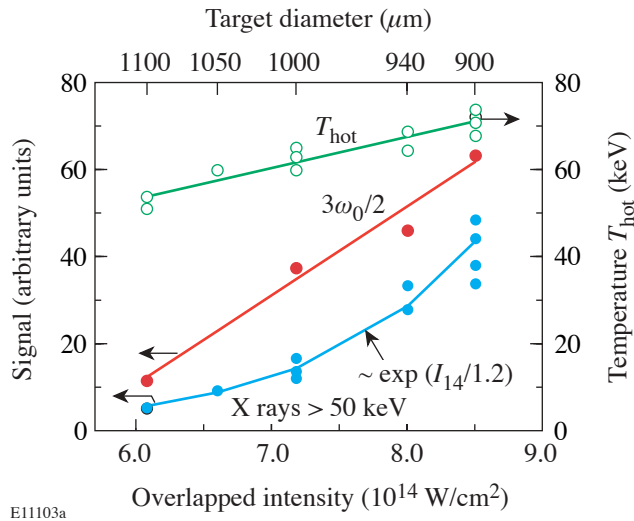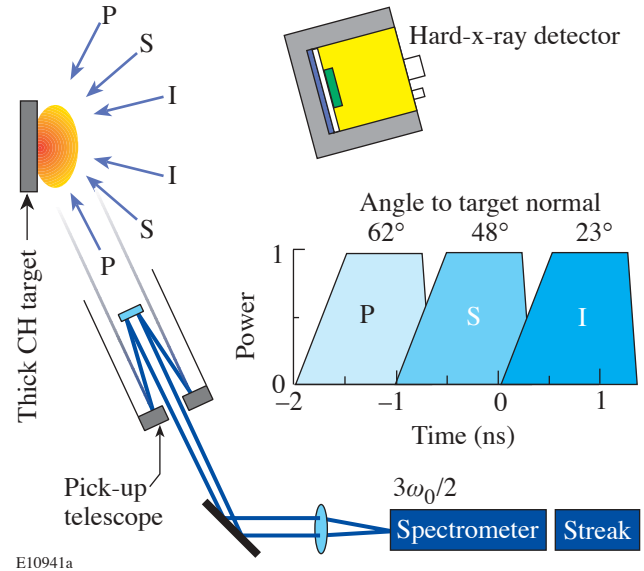
Figure 94.13
Signatures from TPD instability observed in a spherical implosion experiment on OMEGA using targets of varying diameter. The hard-x-ray (>50-keV) signal, the $3\omega_0/2$ emission, and the suprathermal-electron temperature inferred from the hard-x-ray spectrum scale with the total overlapped intensity. The peak single-beam intensity is kept constant.

trons changed by a factor of 10 and the $3\omega_0/2$ signature varied by a factor of 5.

Future direct-drive ignition experiments on the National Ignition Facility (NIF)[29] are expected to generate longer scale lengths (~500 μm) at a higher overlapped laser intensity (1.3×10^{15} W/cm^2). Since these conditions are potentially more vulnerable to suprathermal-electron generation, a set of dedicated planar experiments was carried out at longer scale lengths closer to those expected on the NIF. The experimental layout (Fig. 94.14) was similar to that of Ref. 30. CH targets of 100-μm thickness and 5-mm diameter were sequentially irradiated with nine primary (P) beams, followed by six secondary (S) beams and two to six interaction (I) beams. The interaction beams were incident at ~23° to the target normal, and the P and S beams were at ~62° and ~48°, respectively. The beam-smoothing conditions were identical to the spherical experiments. The P and S beams had standard phase plates that were defocused (~1-mm FWHM) with speckle-averaged peak intensities of ~5 × 10^{13} W/cm^2. The six interaction beams used either standard phase plates at nominal focus (~2 × 10^{14} W/cm^2) or high-intensity phase plates (~0.25-mm FWHM) at 8 × 10^{14} W/cm^2. The individual beam energies were varied between 180 and 360 J, and the laser pulse shape was well approximated by a 500-ps ramp followed by a 1-ns flat portion. Two-dimensional hydrodynamic *SAGE*[31] simulations, which

generally replicate these experimental configurations very well,[21] predict typical electron temperatures of ~2.5 keV and a relatively constant electron-density scale length of ~350 μm for six overlapped interaction beams with standard phase plates. For six high-intensity interaction beams, the predicted electron temperatures rise to ~4.5 keV with density scale lengths reduced to ~180 μm. Simulations for fewer than six overlapped beams generally show similar scale lengths at lower temperatures.

Figure 94.14
Schematic layout of planar experiments using three sets of laser beams: nine primary (P) beams, six secondary (S) beams, and two to six interaction (I) beams. The pulse sequence, pulse shape, and approximate angles of incidence are indicated. The TPD instability is monitored using a streaked optical $3\omega_0/2$ spectrometer and a time-resolved, scintillator-based, four-channel hard-x-ray detector system (only one channel is shown).

Figure 94.15 shows the time-resolved hard-x-ray signal (>50 keV) from a spherical implosion (a) and a planar experiment using six overlapped beams with standard phase plates (b), with the same overlapped intensity of ~10^{15} W/cm^2. In both cases the signal is significantly delayed with respect to the laser pulse and vanishes rapidly at the end of the laser pulse. This delay is not fully understood, but the difference between the spherical and planar experiments is probably due to the pre-existing scale length at the start of the interaction beam for the planar case. The highly nonlinear scaling of the TPD instability with intensity can be observed in the strong amplification of the laser-intensity variations.
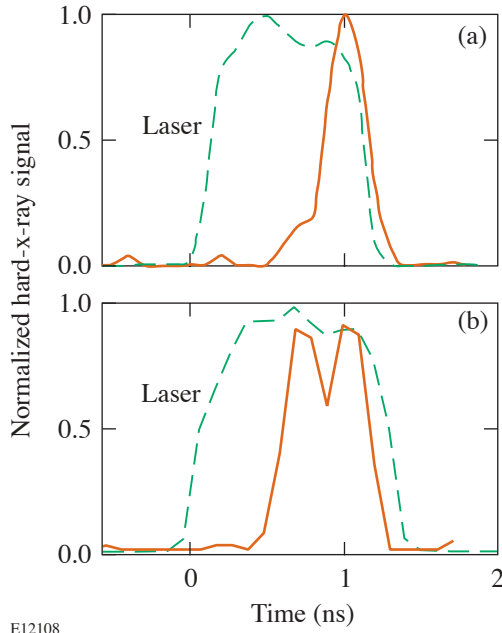
E12108

Figure 94.15

Time-resolved hard-x-ray (>50-keV) emission (solid line) from a spherical implosion experiment (a) and a planar long-scale-length experiment using six beams with standard phase plates (b). The time history of the laser pulse (dashed line) is shown for comparison. The overlapped laser intensity was ~10^{15} W/cm^2 in both cases.

Figure 94.16 shows time-integrated hard-x-ray signals for $E_x > 50$ keV (normalized to the total interaction-beam energy for the planar experiments with both standard and high-intensity phase plates. The pointing accuracy (~50-μm rms) of the overlapping beams is the dominant contribution to the error for the overlapped intensity. The measurement error of the hard-x-ray signal is <10%, about the size of the symbols used. Even though the plasma conditions vary considerably in both scale length and temperature, the hard-x-ray signal is primarily a function of overlapped interaction-beam intensity. The number of overlapped beams and the single-beam intensity seem to be of almost no importance. Remarkably all data can be fit to a universal exponential scaling ~exp ($I_{14}/0.7$) below an intensity of 10^{15} W/cm^2, even stronger than that observed in spherical geometry. Above $10^{15}$ W/cm^2 the scaling of the hard-x-ray signal with intensity changes significantly and is much weaker. The fact that the overlapped intensity governs the scaling of TPD is most easily seen by comparing the signals from six overlapped beams with standard phase plates at an intensity of 11.2×10^{14} W/cm^2 to those of three beams with standard phase plates at an intensity of 5.7×10^{14} W/cm^2. If single-beam intensity were to govern suprathermal-electron

generation, three beams would produce the same hard-x-ray signal per kJ of laser energy as six beams, but actual experiments show >60× reduction, which means that the hard-x-ray signals are actually below the detector threshold.

An absolute measurement of the hard x rays is necessary to infer the heating of the targets from suprathermal electrons. Because the absolute calibration of the hard-x-ray detectors is not very accurate,[20] the detectors have been cross-calibrated with preheat measurements using K_α spectroscopy[32,33] on CH targets with embedded high-Z layers. These layers consisted of 5 μm of titanium followed by 40 μm of vanadium, covered with 20 μm of CH on all sides to avoid direct laser interaction. Consequently the generation of suprathermal electrons is the same as in the primary experiments. The titanium layer absorbs the coronal x radiation without significantly affecting the suprathermal electrons, which then excite K_α radiation in the vanadium layer. The total energy in the vanadium K_α line observed on the back of the target is a good measure of the energy deposited by the electrons and thus the preheat.[32] Thus calibrated, the signals from the hard-x-ray detectors can be used to infer the level of preheat of the CH planar targets. The inferred fractional preheat (preheat energy
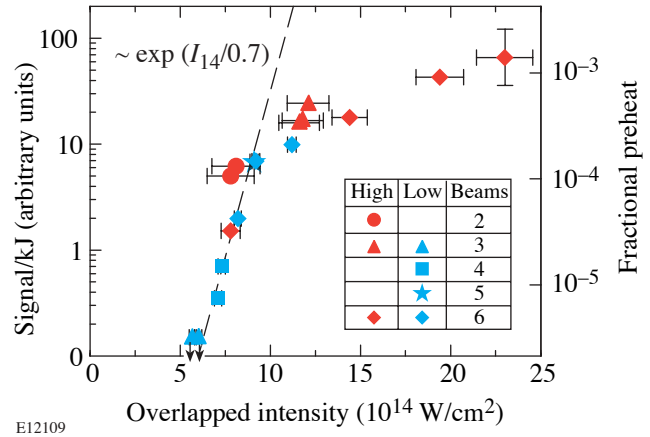
E12109

Figure 94.16

Time-integrated hard-x-ray signals ($E_x > 50$ keV) as a function of overlapped interaction-beam intensity for planar experiments. Two to six beams are used with both standard and high-intensity phase plates at beam energies between 180 and 360 J. The error for the intensity is determined by the beam-pointing accuracy of ~50-μm rms of the overlapping beams. The relative error of the hard-x-ray signal is about the size of the symbols used (<10%). An exponential scaling ~exp ($I_{14}/0.7$) below an overlapped intensity of 10^{15} W/cm^2 (dashed line) is shown for comparison. The axis on the right corresponds to the estimate of the target preheat based on the calibration using K_α spectroscopy. The uncertainty of the calibration (~50%) is indicated with the error bar on the far-right data point.

normalized to incident laser energy) is shown on the right axis of Fig. 94.16. The uncertainty of these numbers is determined by the accuracy of the K_α cross-calibration of ~50%. It is encouraging that the preheat level lies below 0.1% for intensities around 1.3×10^{15} W/cm^2, the peak intensity required for NIF direct-drive experiments.

In conclusion, experimental evidence from both spherical and long-scale-length planar experiments shows clearly that the total overlapped intensity governs the scaling of the suprathermal-electron production while the single-beam intensity is of lesser importance. Presently no theoretical explanation of this behavior exists, but simulations of the nonlinear saturated stage of the TPD instability[12] suggest that the spectrum of the plasma waves broadens considerably, which makes it conceivable that overlapping beams might act on the same plasmon. The exponential scaling seen in both experiments at overlapped intensities below 10^{15} W/cm^2 is even stronger in the planar case than that observed in the spherical experiments. This may be due to the presence of a long ($>100\,\mu$m) and slowly evolving density scale length right from the start of the interaction beam in the planar experiments, which is correlated with an earlier onset of hard-x-ray emission, as compared to the spherical experiments. The origin of the consistently observed change in scaling with intensity of the fractional-preheat levels above 10^{15} W/cm^2 for all studied plasma density scale lengths and temperatures remains unclear at this time. There could potentially be a correlation with the filamentation instability, which has a similar threshold.[34] Nevertheless, this observation increases the confidence that the preheat levels from suprathermal electrons are manageable for direct-drive ignition experiments on the NIF.

ACKNOWLEDGMENT

REFERENCES

1. D. W. Phillion *et al.*, Phys. Rev. Lett. **49**, 1405 (1982).

2. D. M. Villeneuve, R. L. Keck, B. B. Afeyan, W. Seka, and E. A. Williams, Phys. Fluids **27**, 721 (1984).

3. C. Rousseaux *et al.*, Phys. Fluids B **4**, 2589 (1992).

4. W. Seka, R. E. Bahr, R. W. Short, A. Simon, R. S. Craxton, D. S. Montgomery, and A. E. Rubenchik, Phys. Fluids B **4**, 2232 (1992).

5. C. S. Liu and M. N. Rosenbluth, Phys. Fluids **19**, 967 (1976).

6. A. Simon, R. W. Short, E. A. Williams, and T. Dewandre, Phys. Fluids **26**, 3107 (1983).

7. A. B. Langdon, B. F. Lasinski, and W. L. Kruer, Phys. Rev. Lett. **43**, 133 (1979).

8. B. F. Lasinski and A. B. Langdon, Lawrence Livermore National Laboratory, Livermore, CA, UCRL-50021-77, 4-49 (1978).

9. L. V. Powers and R. L. Berger, Phys. Fluids **27**, 242 (1984).

10. *Ibid.*, **28**, 2419 (1985).

11. R. L. Berger and L. V. Powers, *ibid.*, 2895 (1985).

12. D. F. DuBois, D. A. Russell, and H. A. Rose, Phys. Rev. Lett. **74**, 3983 (1995).

13. D. A. Russell and D. F. DuBois, Phys. Rev. Lett. **86**, 428 (2001).

14. J. Meyer and Y. Zhu, Phys. Rev. Lett. **71**, 2915 (1993).

15. R. L. Keck, L. M. Goldman, M. C. Richardson, W. Seka, and K. Tanaka, Phys. Fluids **27**, 2762 (1984).

16. N. A. Ebrahim *et al.*, Phys. Rev. Lett. **45**, 1179 (1980).

17. B. Yaakobi, I. Pelah, and J. Hoose, Phys. Rev. Lett. **37**, 836 (1976).

18. J. D. Hares *et al.*, Phys. Rev. Lett. **42**, 1216 (1979).

19. T. R. Boehly, D. L. Brown, R. S. Craxton, R. L. Keck, J. P. Knauer, J. H. Kelly, T. J. Kessler, S. A. Kumpan, S. J. Loucks, S. A. Letzring, F. J. Marshall, R. L. McCrory, S. F. B. Morse, W. Seka, J. M. Soures, and C. P. Verdon, Opt. Commun. **133**, 495 (1997).

20. C. Stoeckl, V. Yu. Glebov, D. D. Meyerhofer, W. Seka, B. Yaakobi, R. P. J. Town, and J. D. Zuegel, Rev. Sci. Instrum. **72**, 1197 (2001).

21. S. P. Regan, D. K. Bradley, A. V. Chirokikh, R. S. Craxton, D. D. Meyerhofer, W. Seka, R. W. Short, A. Simon, R. P. J. Town, B. Yaakobi, J. J. Caroll III, and R. P. Drake, Phys. Plasmas **6**, 2072 (1999).

22. R. L. McCrory, R. E. Bahr, T. R. Boehly, T. J. B. Collins, R. S. Craxton, J. A. Delettrez, W. R. Donaldson, R. Epstein, V. N. Goncharov, R. Q. Gram, D. R. Harding, P. A. Jaanimagi, R. L. Keck, J. P. Knauer, S. J. Loucks, F. J. Marshall, P. W. McKenty, D. D. Meyerhofer, S. F. B. Morse, O. V. Gotchev, P. B. Radha, S. P. Regan, W. Seka, S. Skupsky, V. A. Smalyuk, J. M. Soures, C. Stoeckl, R. P. J. Town, M. D. Wittman, B. Yaakobi, J. D. Zuegel, R. D. Petrasso, D. G. Hicks, and C. K. Li, in *Inertial Fusion Sciences and Applications 99*, edited by C. Labaune, W. J. Hogan, and K. A. Tanaka (Elsevier, Paris, 2000), pp. 43–53.

23. R. P. Drake *et al.*, Phys. Rev. A **40**, 3219 (1989).

24. D. D. Meyerhofer, J. A. Delettrez, R. Epstein, V. Yu. Glebov, V. N. Goncharov, R. L. Keck, R. L. McCrory, P. W. McKenty, F. J. Marshall, P. B. Radha, S. P. Regan, S. Roberts, W. Seka, S. Skupsky, V. A. Smalyuk, C. Sorce, C. Stoeckl, J. M. Soures, R. P. J. Town, B. Yaakobi, J. D. Zuegel, J. Frenje, C. K. Li, R. D. Petrasso, D. G. Hicks, F. H. Séguin, K. Fletcher, S. Padalino, M. R. Freeman, N. Izumi, R. Lerche, T. W. Phillips, and T. C. Sangster, Phys. Plasmas **8**, 2251 (2001).

25. S. Skupsky, R. W. Short, T. Kessler, R. S. Craxton, S. Letzring, and J. M. Soures, J. Appl. Phys. **66**, 3456 (1989).

26. T. R. Boehly, V. A. Smalyuk, D. D. Meyerhofer, J. P. Knauer, D. K. Bradley, R. S. Craxton, M. J. Guardalben, S. Skupsky, and T. J. Kessler, J. Appl. Phys. **85**, 3444 (1999).

27. T. J. Kessler, Y. Lin, J. J. Armstrong, and B. Velazquez, in *Laser Coherence Control: Technology and Applications*, edited by H. T. Powell and T. J. Kessler (SPIE, Bellingham, WA, 1993), Vol. 1870, pp. 95–104.

28. M. C. Richardson, P. W. McKenty, F. J. Marshall, C. P. Verdon, J. M. Soures, R. L. McCrory, O. Barnouin, R. S. Craxton, J. Delettrez, R. L. Hutchison, P. A. Jaanimagi, R. Keck, T. Kessler, H. Kim, S. A. Letzring, D. M. Roback, W. Seka, S. Skupsky, B. Yaakobi, S. M. Lane, and S. Prussin, in *Laser Interaction and Related Plasma Phenomena*, edited by H. Hora and G. H. Miley (Plenum Publishing, New York, 1986), Vol. 7, pp. 421–448.

29. P. W. McKenty, V. N. Goncharov, R. P. J. Town, S. Skupsky, R. Betti, and R. L. McCrory, Phys. Plasmas **8**, 2315 (2001).

30. W. Seka, H. A. Baldis, J. Fuchs, S. P. Regan, D. D. Meyerhofer, C. Stoeckl, B. Yaakobi, R. S. Craxton, and R. W. Short, Phys. Rev. Lett. **89**, 175002 (2002).

31. R. S. Craxton and R. L. McCrory, J. Appl. Phys. **56**, 108 (1984).

32. B. Yaakobi, C. Stoeckl, T. Boehly, D. D. Meyerhofer, and W. Seka, Phys. Plasmas **7**, 3714 (2000).

33. B. Yaakobi, C. Stoeckl, T. R. Boehly, R. S. Craxton, D. D. Meyerhofer, and W. D. Seka, in *26th European Conference on Laser Interaction with Matter*, edited by M. Kalal, K. Rohlena, and M. Siñor (SPIE, Bellingham, WA, 2001), Vol. 4424, pp. 392–401.

34. Laboratory for Laser Energetics LLE Review **91**, 93, NTIS document No. DOE/SF/19460-458 (2002). Copies may be obtained from the National Technical Information Service, Springfield, VA 22161.

On the Bell–Plesset Effects: The Effects of Uniform Compression and Geometrical Convergence on the Classical Rayleigh–Taylor Instability

Introduction

This article considers a simple treatment of the Rayleigh–Taylor (RT) instability of incompressible perturbations of the interface between two homogeneous fluids undergoing acceleration due to a pressure gradient, including the effects of uniform compression and geometrical convergence. The growth rate for incompressible linear perturbations of a planar interface between incompressible fluids is well known from the work of Rayleigh[1] and Taylor[2] and has become a classic textbook result.[3,4] When the perturbed interface undergoes compression or geometrical convergence, such as in the case of an interface embedded in a collapsing cylinder or sphere, the perturbation growth is modified. These modifications have been referred to collectively[5,6] as Bell–Plesset (BP) effects.[7,8] Both RT and BP effects are known to be important to the outcome of implosion experiments in inertial confinement fusion (ICF).[9–11] The purpose of this article is to formulate and analyze BP effects in a simple way that reveals a wide range of behavior in a variety of geometries.

The term "accelerationless growth" has also been used for BP effects. This terminology acknowledges that interface perturbations would evolve due to convergence and compression in the absence of the buoyant force that drives the RT instability, but, as will be shown below, the modified RT growth does not separate naturally into an acceleration-driven RT contribution and an accelerationless contribution. Nevertheless, the chosen formulation clarifies the physical distinction between RT and BP effects. To be precise, the term "accelerationless" will be used below only to denote perturbation growth in the limit of no RT growth.

The description developed in this article is based on the very similar methods of Bell[2] and Plesset,[3] combining Plesset's treatment of interfaces with an arbitrary density jump, rather than only free surfaces, and Bell's inclusion of uniformly compressible background flow. We also adopt Bell's choice of a mass perturbation amplitude in order to obtain perturbation equations of a particularly simple and useful form. In cases where the local convergence and compression rates are con-

stant over useful time intervals, the perturbation solutions evolve exponentially, and scaling of the perturbation with the interface density and radius can be derived.

The Background Flow

To begin the perturbation calculation describing RT growth, we postulate one-dimensional irrotational unperturbed background flow in planar, cylindrical, and spherical geometries where an interface separates homogeneous fluids of contrasting uniform densities $\rho_1(t)$ and $\rho_2(t)$. The interface is at coordinate position $R(t)$, and the subscripts 1 and 2 denote the half-spaces at coordinate values less than or greater than $R(t)$, respectively. The fluid motion is fully specified by the interface history $R(t)$ and the rate of compression $\gamma_\rho(t)$. From this point on, $R(t)$, $\gamma_\rho(t)$, and other functions of time alone will be written without explicitly indicating the time dependence. This rate of compression is assumed to apply everywhere, or, in other words,

$$\gamma_\rho = \dot{\rho}_1/\rho_1 = \dot{\rho}_2/\rho_2. \tag{1a}$$

Similarly, the convergence rate is written as

$$\gamma_R = \dot{R}/R. \tag{1b}$$

For the cylindrical and spherical cases, R is the radius of the surface, while for a planar interface, the radius is effectively infinite, and $\gamma_R = 0$.

The unperturbed flow velocity is

$$v(x,t) = -(x - R)\gamma_\rho + \dot{R} \tag{2a}$$

in planar geometry,

$$v(r,t) = \dot{R}\left(\frac{R}{r}\right) + \left(\frac{\gamma_\rho}{2}\right)\left(\frac{R^2}{r^2} - 1\right)r \tag{2b}$$

in cylindrical geometry, and

$$v(r,t) = \dot{R}\left(\frac{R^2}{r^2}\right) + \left(\frac{\gamma_\rho}{3}\right)\left(\frac{R^3}{r^3} - 1\right)r \qquad (2c)$$

in spherical geometry. These velocities can be derived from the velocity potential functions

$$\Phi(x,t) = \Phi_0(t) - (x-R)\dot{R} + (x-R)^2\,\gamma_\rho/2 \qquad (3a)$$

in planar geometry,

$$\Phi(r,t) = \Phi_0(t) - \left(R\dot{R} + \gamma_\rho\,R^2/2\right)\ln r + \left(\gamma_\rho/4\right)r^2 \qquad (3b)$$

in cylindrical geometry, and

$$\Phi(r,t) = \Phi_0(t) + \frac{R^2\dot{R}}{r} + \left(\frac{\gamma_\rho}{3}\right)\left(\frac{r^2}{2} + \frac{R^3}{r}\right) \qquad (3c)$$

in spherical geometry using

$$\vec{v} = -\vec{\nabla}\Phi.^4 \qquad (4)$$

These flows can be obtained from the Euler equation in one dimension

$$\frac{\partial v}{\partial t} + v\frac{\partial v}{\partial x} = -\frac{\partial U(x)}{\partial x} - \frac{1}{\rho}\frac{\partial p(x,t)}{\partial x}, \qquad (5)$$

given the appropriate pressure $p(x,t)$ and external potential field $U(x,t)$. In planar geometry, it is easy to verify that the desired flow is obtained from the pressure

$$p(x,t) = p_0 - \rho g_P(x-R) + \rho\left(\dot{\gamma}_\rho - \gamma_\rho^2\right)(x-R)^2\big/2 \qquad (6a)$$

and the external potential field

$$U(x,t) = U_0 - g_U x, \qquad (7)$$

where

$$g_P = -\frac{1}{\rho}\frac{\partial p(R,t)}{\partial x}$$

and

$$g_U = -\frac{\partial U(R)}{\partial x}$$

are the separate components of the fluid acceleration at the unperturbed interface position due to pressure and the external potential, respectively. Using

$$\dot{R} = v(R,t), \qquad (8)$$

the Euler equation gives

$$\ddot{R} = g_U + g_P. \qquad (9)$$

In cylindrical geometry, the required combination of pressure and potential field is

$$U + \frac{p}{\rho} = \left(U + \frac{p}{\rho}\right)_{r=R} - \left[R\ddot{R} + \dot{R}^2 + \gamma_\rho R\dot{R}\right]\ln r$$

$$+ \left[\frac{\dot{\gamma}_\rho}{2} - \left(\frac{\gamma_\rho}{2}\right)^2\right]r^2$$

$$- \frac{1}{2}\left[\frac{\dot{R}^2}{2} + \gamma_\rho R\dot{R} - \left(\frac{\gamma_\rho}{2}\right)^2 R^2\right]\left(\frac{R^2}{r^2}\right), \qquad (6b)$$

and in spherical geometry, the required combination is

$$U + \frac{p}{\rho} = \left(U + \frac{p}{\rho}\right)_{r=R} + \frac{\ddot{R}R^2}{r} - \left(\frac{2R\dot{R}^2}{r} - \frac{4}{3}\gamma_\rho\frac{R^2\dot{R}}{r}\right)$$

$$\times\left(1 - \frac{R^3}{4r^3}\right) - \left(\frac{\gamma_\rho}{3}\right)^2\frac{r^2}{2}\left(1 - \frac{R^3}{r^3}\right)^2$$

$$+ \left(\frac{\dot{\gamma}_\rho}{3}\right)\frac{r^2}{2}\left(1 + \frac{2R^3}{r^3}\right). \qquad (6c)$$

Again, in both the latter cases, Eq. (9) is obtained from the Euler equation.

The one-dimensional background flow in planar geometry conserves mass everywhere according to

$$\vec{\nabla} \cdot \vec{v} = -\gamma_\rho, \tag{10a}$$

but, for arbitrary convergence and compression rates, a line source is required for cylindrical flow,

$$\vec{\nabla} \cdot \vec{v} = -\gamma_\rho + \dot{m}\delta^{(2)}(r), \tag{10b}$$

where

$$\frac{\dot{m}}{\pi\rho R^2} = 2\gamma_R + \gamma_\rho, \tag{11a}$$

and a point source is required for spherical flow,

$$\vec{\nabla} \cdot \vec{v} = -\gamma_\rho + \dot{m}\delta^{(3)}(r), \tag{10c}$$

where

$$\frac{3\dot{m}}{4\pi\rho R^2} = 3\gamma_R + \gamma_\rho. \tag{11b}$$

The cylindrical and spherical velocities given by Eqs. (2b) and (2c) can be written simply in terms of $\dot{m}$ as

$$v(r,t) = \frac{\dot{m}}{2\pi r\rho} - \gamma_\rho \frac{r}{2} \tag{12a}$$

and

$$v(r,t) = \frac{\dot{m}}{4\pi\rho r^2} - \gamma_\rho \frac{r}{3}. \tag{12b}$$

To consider a broad range of BP effects, it is important to be able to specify the compression and convergence rates independently, and this requires the mass source $\dot{m}$ at $r = 0$. Imposing $\dot{m} = 0$ restricts the problem to either constant cylindrical mass, $2\gamma_R + \gamma_\rho = 0$, or constant spherical mass, $3\gamma_R + \gamma_\rho = 0$. According to Eqs. (6), placing a mass source at $r = 0$ to create desired background flows introduces unphysical pressures at $r = 0$. These flows are unlikely to resemble any intended application globally, but they suffice for the perturbation calculations if they are reasonably descriptive of conditions in the neighborhood of the density jump because discrepant

flow beyond a few perturbation wavelengths from the density jump will be largely decoupled from the perturbations.

It is worth noting a curious property of Eq. (6a) for the pressure driving the planar flow. For planar flow that is either converging or diverging at a constant rate $\dot{\gamma}_\rho = 0$, the pressure does not depend on the sign of γ_ρ; in both cases, the pressure driving the flow exerts a diverging force, even if the flow is converging. In both cases, the distinction between diverging and converging flow comes from the initial conditions of the flow, not the pressure.

Perturbation Equations

To obtain the equations of motion for the incompressible perturbations of these interfaces, we follow the calculation of Plesset for a spherical interface.[8] Following the work of Bell,[7] we generalize Plesset's method to include cylindrical and planar geometries and to include compression of the unperturbed background flow at a spatially uniform rate.

The velocity potential function Φ describing irrotational flow with uniform mass density is governed by the Bernoulli theorem[4,12]

$$\frac{p}{\rho} + U + \frac{1}{2}|v^2| - \frac{\partial \Phi}{\partial t} = 0, \tag{13}$$

where all the quantities have been defined above. The velocity potential includes the potential for the background flow plus the potential perturbation $\Phi_{\text{total}} = \Phi + \phi_\ell(\vec{x}, t)$. The subscript ℓ denotes the harmonic order of the perturbation mode corresponding to $\cos(2\pi\ell y/L)$, $\cos(\ell\theta)$, or $Y_\ell^m(\theta, \phi)$ transverse harmonic dependence in planar, cylindrical, and spherical geometry, respectively. The perturbation is assumed to be incompressible, which requires

$$\nabla^2\phi_\ell = 0. \tag{14}$$

Imposing vanishing boundary conditions on ϕ_ℓ at large distances from the interface and continuity at the origin, if applicable, we obtain solutions for each side of the interface for planar, cylindrical, and spherical geometries:

$$\phi_{\ell\pm}(\vec{x}, t) = b_{\ell\pm}(t)e^{\pm 2\pi\ell x/L} \cos(2\pi\ell y/L), \tag{15a}$$

$$\phi_{\ell\pm}(\vec{x}, t) = b_{\ell\pm}(t)r^{\pm\ell} \cos(\ell\theta), \tag{15b}$$

and

$$\phi_{\ell\pm}(\vec{x},t) = b_{\ell\pm}(t) r^{[\ell,-(\ell+1)]} Y_\ell^m(\theta,\phi). \qquad (15c)$$

For the planar perturbation, we have imposed a zero boundary condition at $y = 0$ and $y = L$ so that the set of perturbation modes would form a discrete spectrum with an integer index ℓ, preserving a unity of notation among the three geometries with no loss of generality. For planar and cylindrical geometry, we have disregarded z-dependent perturbations.

The position of the perturbed interface is $r = r_s(t)$, where

$$r_s(t) = R + a_\ell(t)\cos(2\pi\ell y/L), \qquad (16a)$$

$$r_s(t) = R + a_\ell(t)\cos(\ell\theta), \qquad (16b)$$

and

$$r_s(t) = R + a_\ell(t) Y_\ell^m(\theta,\phi) \qquad (16c)$$

for planar, cylindrical, and spherical geometries, respectively. The interface displacement a_ℓ is the spatial amplitude of the perturbation.

Whenever it is clear in the following development that a coordinate-dependent expression applies to all three geometries, the symbol r will be used to denote the coordinate in the direction of the unperturbed flow, rather than repeat the exact same expression using the Cartesian coordinate symbol x for planar flow.

An ordinary second-order differential equation for a_ℓ is obtained from Eq. (13), first by evaluating P on both sides of the interface in terms of the perturbed velocity potential to first order in small distances from the unperturbed interface. These expressions for P are then matched at the interface $r = r_s$. A required expression for the function $b_{\ell\pm}$ in terms of the amplitude a_ℓ is obtained by equating the interface velocity to the fluid velocity at the interface:

$$\frac{dr_s}{dt} = -\frac{\partial\left[\Phi(r_s,t) + \phi_{\ell\pm}(r_s,t)\right]}{\partial r}. \qquad (17)$$

This matching of pressures eliminates δp_ℓ, leaving an ordinary homogeneous second-order differential equation for a_ℓ.

Equations (6) show that one can write a pressure that produces the desired background flow. For the purposes of constructing linear equations for flow perturbations near $r = R$, the linear approximation

$$U(x,t) \approx U_0 - rg_U, \quad p(x,t) \approx p_0 - (r-R)\rho g_p \qquad (18)$$

suffices. As Eq. (9) for the interface acceleration suggests, the background flow does not depend on the potential and the pressure gradients separately, only their sum. The RT growth rate, however, depends most directly on g_p and not g_U. In the absence of pressure gradients $g_p = 0$, the fluid is in a state of free fall, where there are no buoyant forces to drive the RT instability.

To begin constructing the expression for pressure continuity at the perturbed interface, we begin by rewriting Eq. (13) as

$$\frac{P(r,t) + \delta p_\ell}{\rho} = -U_0 + rg_U - \frac{1}{2}\left|v^2\right| + \frac{\partial\Phi}{\partial t}. \qquad (19)$$

All quantities are evaluated at $r = r_s$ by expanding them to first order in the perturbation about the unperturbed interface position $r = R$. We evaluate the pressures in the fluid half-spaces $r < R$ and $r > R$, denoted by subscripts 1 and 2, respectively. Matching the harmonic components of the pressure perturbation $\delta p_{\ell 1} = \delta p_{\ell 2}$ gives the perturbation equations, which are

$$\left(-\gamma_\rho + \frac{d}{dt}\right)\frac{d}{dt}(a_\ell\rho) = \gamma_0^2(a_\ell\rho), \qquad (20a)$$

$$\left(-\gamma_\rho + \frac{d}{dt}\right)\frac{d}{dt}(a_\ell\rho R) = \gamma_0^2(a_\ell\rho R), \qquad (20b)$$

and

$$\left(-\gamma_\rho - \gamma_R + \frac{d}{dt}\right)\frac{d}{dt}(a_\ell\rho R^2) = \gamma_0^2(a_\ell\rho R^2) \qquad (20c)$$

for planar, cylindrical, and spherical geometry, respectively. The resulting perturbation equations assume this simple and transparent form when written in terms of the "mass" amplitude z_ℓ, where

$$z_\ell = a_\ell \rho, \quad z_\ell = a_\ell \rho R, \quad \text{or} \quad z_\ell = a_\ell \rho R^2 \qquad (21)$$

for the three chosen geometries. The interface density ρ can be the mean density $\rho = (\rho_1 + \rho_2)/2$ or any other fixed linear combination of ρ_1 and ρ_2. Since a uniform compression rate applies everywhere, according to Eq. (1a), the only effect of alternative choices for the interface density is to introduce a constant factor into the definition of the mass amplitude [Eq. (21)]. The units of z_ℓ are mass only for spherical geometry. They are mass per area for planar geometry and mass per axial length for cylindrical geometry. In this form, the "driving" terms are proportional to the RT growth rates γ_0, where

$$\gamma_0^2 = k \frac{(\rho_2 - \rho_1)}{(\rho_2 + \rho_1)} g_p, \qquad (22a)$$

$$\gamma_0^2 = \frac{\ell}{R} \frac{(\rho_2 - \rho_1)}{(\rho_2 + \rho_1)} g_p, \qquad (22b)$$

and

$$\gamma_0^2 = \frac{\ell(\ell+1)}{R} \frac{(\rho_2 - \rho_1)}{[\ell \rho_2 + (\ell+1)\rho_1]} g_p \qquad (22c)$$

for the three geometries. Equation (22a) is the familiar "classical" RT growth rate for incompressible planar flow. The spherical results [Eqs. (20c) and (22c)] are equivalent to the result of Plesset[8] for incompressible fluid ($\gamma_\rho = 0$), even though they are not easily recognized as such. For the special case of a free surface (either $\rho_1 = 0$ or $\rho_2 = 0$), Eqs. (20) and (22) become Bell's[7] final result.

The driving terms are easily identified as being the only terms containing either an acceleration or a density jump, both of which are required for the buoyant force driving the RT effect. Compared with alternative formulations,[8,11] Eqs. (20) and (22) display a more physically meaningful isolation of the RT effect into a single term. Even though the RT effect can be

isolated in this way, the total perturbation growth rates do not separate naturally into RT and BP contributions. The form of Eqs. (20) does allow equations governing accelerationless growth to be obtained by setting $\gamma_0 = 0$, but the accelerationless limit cannot be simply combined with the classical RT growth rate to obtain a correct result.

Equations (20) are easily solved over time intervals where the compression and convergence rates, γ_ρ and γ_R, respectively, and the RT growth rate γ_0 are constant. The resulting solution pairs are exponential in time with constant growth rates,

$$\gamma_\pm = \frac{1}{2}\gamma_\rho \pm \sqrt{\gamma_0^2 + \frac{1}{4}\gamma_\rho^2} \qquad (23a)$$

for both planar and cylindrical geometry and

$$\gamma_\pm = \frac{1}{2}(\gamma_\rho + \gamma_R) \pm \sqrt{\gamma_0^2 + \frac{1}{4}(\gamma_\rho + \gamma_R)^2} \qquad (23b)$$

for spherical geometry. Since γ_0^2 can be negative, the growth rates can be complex, giving perturbations exhibiting exponential or sinusoidal behavior, or both. In characterizing an interface as stable or unstable, Plesset argues that exponential behavior suggests unbounded growth of one of the solutions, which indicates instability. Conversely, oscillation suggests stability. Even though Eqs. (20c) and (22c) are consistent with the corresponding equations of Plesset,[8] one can draw different conclusions about the criteria for stability based solely on the inspection of the respective equations. Except for the case of planar incompressible flow, exponential growth, for example, does not necessarily imply net growth. Equations (23) can be a guide in formulating general stability criteria for intervals where γ_ρ, γ_R, and γ_0 are constant, but there are other approaches. In the next section where BP effects in the large-γ_0 limit are considered, the solutions appear as products of power-law factors of R and ρ and a factor that is exponential in $\gamma_0 t$. If one does not regard power-law density and radius scaling behavior as either stable or unstable, then the question of stability is simply the question of the sign of γ_0^2, without regard for BP effects.

Solving fully time-dependent perturbation equations [Eqs. (20) and (22)] provides a more complete and thus more correct description of RT growth than the common practice of

estimating unstable growth from an exponential growth factor, such as

$$a(t) = a(0) \exp\left[\int_0^t \gamma(t')\,dt'\right], \qquad (24)$$

where the positive growth rate is used in the integrand. The fully time-dependent solution permits specifying amplitudes with arbitrary initial values and time derivatives, while the growth factor implies a particular initial condition. For example, the solution pair for incompressible planar flow has equal and opposite growth rates, so a solution with a static initial amplitude is composed initially of equal parts of the growing and decaying components of the general solution. Equation (24), on the other hand, attributes the entire initial amplitude to the growing component of the full solution. As a result, the growth-factor solution will become too large by a factor of 2 if it is used to represent growth of a perturbation that is initially static. More generally, if the acceleration changes abruptly from one constant value to another, matching the solutions before and after the change cannot be done without considering the fully time-dependent solution. A second advantage of the fully time-dependent formulation is that Richtmyer–Meshkov–like[13] behavior is obtained for impulsive acceleration. For an acceleration with an appropriate oscillating component, the fully time-dependent formulation exhibits the dynamic stabilization effect obtained by Betti *et al.*,[14] another effect that cannot be described by an exponential growth factor.

Equations (20) and (22) were originally derived for use in a perturbation growth model for a saturable multimode model of RT instability[16] applicable to simulations of inertial confinement fusion experiments.[15]

Scaling

In this section, we shall examine both the mass and spatial perturbation amplitudes in two limits where the BP effects appear entirely as scaling factors with power-law dependences on the interface density and radius. The first is the accelerationless limit of small γ_0, and the second is the limit of rapid RT growth, relative to the compression and convergence rates. As will be shown below, the accelerationless BP effects are different from BP effects occurring in combination with the RT instability.

In the limit where the interface acceleration vanishes, or when the density jump at the interface vanishes, γ_0 approaches zero. In this limit, assuming constant compression and convergence rates, the pairs of solutions are of the form $z_\pm \propto \exp(\gamma_\pm t)$, where

$$\gamma_\pm = [\gamma_\rho, 0] \qquad (25a)$$

for both planar and cylindrical geometry and

$$\gamma_\pm = [\gamma_\rho + \gamma_R, 0] \qquad (25b)$$

for spherical geometry. The leading-order RT corrections to Eqs. (25) are second order in γ_0. From assuming that γ_ρ and γ_R are constants, we have $R \propto \exp(\gamma_R t)$ and $\rho \propto \exp(\gamma_\rho t)$ and the solution pairs are

$$z_\pm \propto [\rho, 1] \qquad (26a)$$

for planar and cylindrical geometry and

$$z_\pm \propto [\rho R, 1] \qquad (26b)$$

for spherical geometry. For uniform compression of a constant cylindrical mass $M = \rho R^2$ or spherical mass $M = \rho R^3$, the solutions $z_{M\pm}$ are

$$z_{M\pm} = [R^{-2}, 1] \qquad (27)$$

for both cylindrical and spherical geometry. The spatial amplitudes are related to the mass amplitudes according to Eq. (21), which gives

$$a_\pm = [1, \rho^{-1}], \qquad (28a)$$

$$a_\pm = [R^{-1}, (\rho R)^{-1}], \qquad (28b)$$

and

$$a_\pm = [R^{-1}, (\rho R^2)^{-1}]. \qquad (28c)$$

For uniform compression of a constant cylindrical mass or spherical mass, the solutions $a_{M\pm}$ are

$$a_{M\pm} = \left[R^{-1}, R \right] \qquad (29)$$

for both cylindrical and spherical geometry.

While the accelerationless limit gives a view of the BP effects in the absence of RT growth, a more interesting limit is that of a dominant RT effect or, equivalently, of large ℓ where we have $\gamma_0 \gg \gamma_\rho$, $\gamma_0 \gg \gamma_R$, and $\gamma_0^2 \gg \dot{\gamma}_0$. In this limit, Eqs. (23) become, to leading order in the small numbers γ_ρ/γ_0 and/or γ_R/γ_0,

$$\gamma_\pm \approx \frac{1}{2}\gamma_\rho \pm \gamma_0 \qquad (30a)$$

for both planar and cylindrical geometry and

$$\gamma_\pm \approx \frac{1}{2}\left(\gamma_\rho + \gamma_R\right) \pm \gamma_0 \qquad (30b)$$

for spherical geometry. In an imploding sphere, such as in the deceleration phase of an ICF implosion experiment,[17,18] for example, we estimate the magnitude of the small parameter of this limit by writing the classical growth rate as

$$\gamma_0^2 \approx \ell A \frac{\ddot{R}}{R}, \qquad (31)$$

where A is the Atwood number

$$A \equiv \frac{(\rho_2 - \rho_1)}{(\rho_2 + \rho_1)}. \qquad (32)$$

For the purpose of characterizing a large-ℓ limit, it is sufficient to assign a single time scale τ to all time derivatives,

$$\ddot{R} \sim R/\tau^2, \quad \dot{R} \sim R/\tau, \quad \dot{\rho} \sim \rho/\tau, \qquad (33)$$

so that the small number in this limit is

$$\gamma_\rho/\gamma_0 \sim \gamma_R/\gamma_0 \sim (\ell A)^{-1/2}, \qquad (34)$$

which is small for the large mode numbers of interest in ICF implosions.[17] In this limit, the solution pairs are

$$z_\pm \propto \rho^{1/2} e^{\pm\gamma_0 t} \qquad (35a)$$

for planar and cylindrical geometry and

$$z_\pm \propto \rho^{1/2} R^{1/2} e^{\pm\gamma_0 t} \qquad (35b)$$

for spherical geometry. For uniform compression of a constant cylindrical mass or spherical mass, the solutions $z_{M\pm}$ are

$$z_{M\pm} = R^{-1} e^{\pm\gamma_0 t} \qquad (36)$$

for both cylindrical and spherical geometry. The corresponding spatial amplitudes are

$$a_\pm = \rho^{-1/2} e^{\pm\gamma_0 t}, \qquad (37a)$$

$$a_\pm = \rho^{-1/2} R^{-1} e^{\pm\gamma_0 t}, \qquad (37b)$$

and

$$a_\pm = \rho^{-1/2} R^{-3/2} e^{\pm\gamma_0 t}. \qquad (37c)$$

For uniform compression of a constant cylindrical mass or spherical mass, the solutions $a_{M\pm}$ are

$$a_{M\pm} = e^{\pm\gamma_0 t}, \qquad (38)$$

which is an interesting example of a spatial amplitude evolving virtually free of any BP effects.

In this large-ℓ limit, the BP effects appear separately from the RT growth factors as scaling factors in powers of ρ and/or R that are the same for both solutions of each pair. The fact that the BP effects are the same for both solutions is a property unique to the large-ℓ limit. Except in this one limit, Eqs. (23) predict different BP effects for the two solutions.

Discussion

In the accelerationless limit where $\gamma_0 = 0$, the density and radius scaling of the perturbation solutions of constant mass amplitude are readily visualized. These solutions are the second solutions of Eqs. (26) and (27) and their spatial-amplitude

counterparts in Eqs. (28) and (29). The spherical cases are illustrated schematically in Fig. 94.17, where a layer of fluid is highlighted to suggest the "peak-to-valley" extent of the perturbation. Figure 94.17(a) shows an incompressible spherical layer thickening as it converges to maintain constant density, and Fig. 94.17(b) shows the same layer compressing in proportion to the radius of the uniformly compressing homogeneous sphere in which it is embedded. It is important to remember that this solution of constant mass amplitude is obtained only with appropriate initial conditions. The general solution for arbitrary initial conditions exhibits a more complicated mixture of behaviors. The fact that the convergence and compression effects are different for the two solutions in each pair is the rule, not the exception. It is a unique property of the opposite limit, where the RT rate is much larger than the compression and convergence rates, that both solutions exhibit the same BP scaling with density and radius.

growth for an incompressible spherical shell ($\gamma_\rho = 0$), for a uniformly compressing sphere ($3\gamma_R + \gamma_\rho = 0$), and for the incompressible planar limit ($\gamma_R = \gamma_\rho = 0$) with no BP effects. Figure 94.18(a) shows results obtained by applying a static initial condition to the spatial amplitude, and Fig. 94.18(b) shows the same results obtained by applying a static initial condition to the mass amplitude. The RT growth rate was set to $\gamma_0^2 = 4\ddot{R}/R$, choosing $\ell A = 4$ to create an intermediate case between the accelerationless and the large-growth limits. The results show that BP effects vary in importance, depending on which compressibility assumption is made, and that they are sensitive to the choice of initial condition. If the amplitude is initialized as a static mass amplitude, the incompressible shell growth is particularly large. These results should not be ex-

(a)
Incompressible shell

(b)
Compressing core

$$\frac{d\rho}{dt} = 0 \rightarrow a_\ell \propto R^{-2}$$

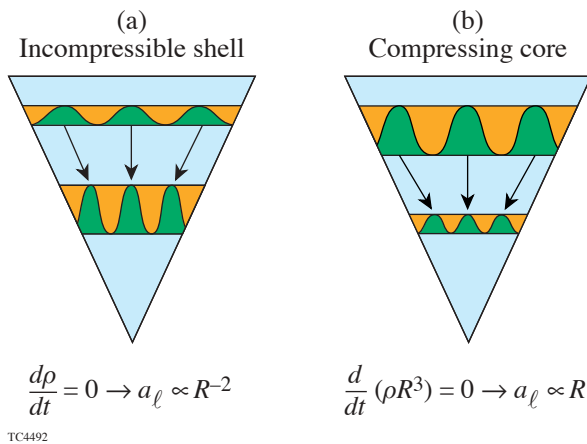$$\frac{d}{dt}(\rho R^3) = 0 \rightarrow a_\ell \propto R$$

TC4492

Figure 94.17
The cases of a perturbed surface embedded in an incompressible shell and a compressible sphere suggest, respectively, $a_\ell \propto R^{-2}$ and $a_\ell \propto R$ scaling of the spatial amplitude in the absence of a Rayleigh–Taylor growth term. Each of these solutions are paired with another independent solution, however, and the scaling behavior is more complicated if contributions from these other solutions are introduced by the initial conditions of the amplitude.

TC4493

Figure 94.18
Significant differences in perturbation growth are obtained for different compressibility cases and with different initializations. Results for perturbations of an incompressible shell (I) and a compressible sphere (C) are shown, compared with the results of the "classical" Rayleigh–Taylor model, or the incompressible planar approximation (P), where convergence and compression effects are ignored. The importance of initial conditions is seen by comparing results obtained using (a) static initial spatial amplitudes and (b) static initial mass amplitudes.

A simple demonstration of the importance of BP effects and the differences obtained from alternative initial conditions are shown in Fig. 94.18. The two plots show the growth of the spatial amplitude of a perturbation of an imploding, decelerating spherical interface. The implosion parameters correspond roughly to those of ICF capsule implosions near peak compression. The surface is assumed to compress by a radial factor of 10 while decelerating uniformly at 2.0×10^{16} cm/s^2 from a radius of 400 μm. The perturbation growth was calculated by direct integration of Eq. (20c). Each plot shows the amplitude

pected to conform closely to the scaling results [Eqs. (37c) and (38)] because the compression, convergence, and RT rates are not constant and γ_0^2 does not occur close to either of the scaling limits of the previous section, but Eq. (38) does suggest that the amplitudes from the compressible sphere and incompressible planar models should tend to agree as they seem to do in both plots. Also, Eq. (37c) suggests that the BP effect on the amplitude of a spatial perturbation of a spherical surface converging by a factor of 10 should increase the amplitude over the other two cases by about 1.5 decades, which is approximately what is seen in Fig. 94.18(b).

Actual ICF implosions are, of course, more complicated than this simple illustration. The deceleration of the compressing core occurs during a brief "deceleration" phase following a longer "coasting" phase between the period of acceleration due to the driver and the onset of deceleration by the compressing core. The coasting phase can be characterized crudely by an incompressible shell in the accelerationless limit ($\gamma_\rho = 0$ and $\gamma_0 = 0$), and the deceleration phase would resemble, in contrast, the case of the uniformly compressing sphere ($3\gamma_R + \gamma_\rho = 0$). In a realistic simulation, the convergence and compression rates vary continuously, and the true description of an unstable surface will be somewhere between the limits of an incompressible shell and a uniformly compressible sphere of constant mass.

Overall, BP effects in the accelerationless limit and in the limit where the RT growth is dominant exhibit distinct differences in the nature of the effects and in their importance. Between these two scaling limits, the latter is the more applicable limit when analyzing observations of hydrodynamic instability in ICF implosion experiments.

The BP effects have been called the "Bell–Plesset instability,"[6] which is not a correct description. They may be better described as a scaling behavior, for example, but they are certainly not a true instability in the sense that the RT instability is a true instability whose growth is driven by positive feedback that grows in proportion to its amplitude.

Summary and Conclusion

A formal description of the BP effects of compression and geometric convergence on the RT instability has been obtained. Even though the chosen model is restricted to incompressible perturbations of an interface separating homogeneous fluids and to a spatially uniform compression rate for the entire fluid, the model is general enough to encompass a usefully broad range of behavior. Results for three geometries (planar,

cylindrical, and spherical) are presented in parallel, and the fluid is allowed to compress and converge independently. The governing perturbation equations [Eqs. (20) and (22)] are only slightly modified from the classical RT equations as given by Eqs. (20a) and (22a) for incompressible ($\gamma_\rho = 0$) planar flow whose solutions exhibit simple exponential or sinusoidal evolution of the interface distortion. The RT growth rates for the three chosen geometries are very similar and, as expected, become identical in the limit of large harmonic order ℓ or k, where $k = \ell/L$. The first of two modifications of the planar incompressible RT equation that add the BP effects is to write it in terms of a mass amplitude. It is not surprising that the perturbation equations would be simplified by writing them in terms of a mass amplitude because an embedded perturbed interface would simply compress and converge with the flow, with the peak-to-valley displacement of the interface demarcating a layer of constant mass. The second modification is to add a first-time-derivative term appropriate for the chosen geometry, which results in a pair of growth rates that differ by more than just a sign flip.

With constant compression, convergence, and growth rates, the simple form of Eqs. (20) leads to BP effects expressible as power-law scaling with density and radius. These scalings vary, depending on the underlying geometry, the assumed interdependence of the compression and convergence rates, and which limit of either slow [Eqs. (25)–(29)] or rapid [Eqs. (30)–(33)] RT growth applies. In the limit of slow RT growth or, equivalently, in the limit of true accelerationless growth, each solution in a pair has its own distinct BP scaling, and only one solution of the pair exhibits the constant mass amplitude expected for an embedded surface. The scaling behavior is distinctly different for RT growth that is much faster than the convergence and/or compression. While rapid RT growth might amount to several e foldings in, for example, an ICF implosion, the BP effects can be much smaller and still amount to a significant effect. In this limit, the BP scaling becomes identical for each of the pair of solutions. While the variety of scalings among the solutions is simpler where RT growth dominates, the scaling is neither as intuitive nor as recognizable as the constant mass amplitude solution of the accelerationless limit. Perhaps the most surprising result is Eq. (38), indicating no first-order BP effect at all for the uniform compression of a constant spherical or cylindrical mass.

Even though the underlying assumptions behind the results shown here are somewhat restrictive, this presentation of a unified body of results for several geometries and flow characteristics hopefully has conveyed a clearer sense of the origin,

nature, and the surprising diversity of BP effects and their tendency to defy any simple characterization applicable over a wide range of circumstances.

ACKNOWLEDGMENT

REFERENCES

1. Lord Rayleigh, Proc. London Math Soc. **XIV**, 170 (1883).

2. G. Taylor, Proc. R. Soc. London Ser. A **201**, 192 (1950).

3. S. Chandrasekhar, *Hydrodynamic and Hydromagnetic Stability*, International Series of Monographs on Physics (Dover Publications, New York, 1981), Chap. X, pp. 428–480.

4. L. D. Landau and E. M. Lifshitz, *Fluid Mechanics* (Pergamon Press, London, 1959).

5. J. B. Beck, "The Effects of Convergent Geometry on the Ablative Rayleigh–Taylor Instability in Cylindrical Implosions," Ph.D. thesis, Perdue University, 1996.

6. W. W. Hsing and N. M. Hoffman, Phys. Rev. Lett. **78**, 3876 (1997).

7. G. I. Bell, Los Alamos National Laboratory, Report LA-1321 (1951).

8. M. S. Plesset, J. Appl. Phys. **25**, 96 (1954).

9. W. W. Hsing *et al.*, Phys. Plasmas **4**, 1832 (1997).

10. V. N. Goncharov, P. McKenty, S. Skupsky, R. Betti, R. L. McCrory, and C. Cherfils-Clérouin, Phys. Plasmas **7**, 5118 (2000).

11. P. Amendt *et al.*, Phys. Plasmas **10**, 820 (2003).

12. A. L. Fetter and J. D. Walecka, *Theoretical Mechanics of Particles and Continua*, International Series in Pure and Applied Physics (McGraw-Hill, New York, 1980).

13. R. D. Richtmyer, Commun. Pure. Appl. Math. **XIII**, 297 (1960).

14. R. Betti, R. L. McCrory, and C. P. Verdon, Phys. Rev. Lett. **71**, 3131 (1993).

15. R. Epstein, J. A. Delettrez, and C. P. Verdon, presented at the 27th Annual Anomalous Absorption Conference, Vancouver, BC, Canada, 1–5 June 1997.

16. S. W. Haan, Phys. Rev. A **39**, 5812 (1989).

17. P. W. McKenty, V. N. Goncharov, R. P. J. Town, S. Skupsky, R. Betti, and R. L. McCrory, Phys. Plasmas **8**, 2315 (2001).

18. D. D. Meyerhofer, J. A. Delettrez, R. Epstein, V. Yu. Glebov, V. N. Goncharov, R. L. Keck, R. L. McCrory, P. W. McKenty, F. J. Marshall, P. B. Radha, S. P. Regan, S. Roberts, W. Seka, S. Skupsky, V. A. Smalyuk, C. Sorce, C. Stoeckl, J. M. Soures, R. P. J. Town, B. Yaakobi, J. Frenje, C. K. Li, R. D. Petrasso, F. H. Séguin, K. Fletcher, S. Padalino, C. Freeman, N. Izumi, R. A. Lerche, T. W. Phillips, and T. C. Sangster, Plasma Phys. Control. Fusion **43**, A277 (2001).

Laser-Induced Adiabat Shaping by Relaxation in Inertial Confinement Fusion Implosions

Introduction

In direct-drive inertial confinement fusion (ICF), a spherical shell of cryogenic deuterium–tritium is imploded by direct laser irradiation. As the shell accelerates inward, the outer surface is unstable due to the Rayleigh–Taylor (RT) instability, which causes a large shell distortion leading to significant degradation in capsule performance. Controlling the seeds and the growth rates of the RT instability during the acceleration phase is essential for the success of ICF implosions. The main damping mechanism of the instability growth during the acceleration phase is the ablative mass flow[1,2] off the shell's outer surface since the RT growth rates for cryogenic DT can be approximated as[2] $\Gamma \approx 0.94\sqrt{kg} - 2.7\,kV_a$, where g is the shell acceleration, k is the instability wave number, and V_a is the ablation velocity. The latter represents the propagation speed of the heat front into the imploding shell and is inversely proportional to the shell density at the ablation front, $V_a = \dot{m}/\rho_a$, where $\dot{m}$ is the mass ablation rate per unit area and ρ_a is the shell density at the ablation front. While the ablation rate is solely dependent on the laser intensity $\left(\dot{m} \sim I^{1/3}\right)$, the density is related to the local value of the entropy (also referred to as the "adiabat") $\rho_a = \left(p_a/S_a\right)^{1/\gamma}$, where p_a is the ablation pressure, S_a is the ablation-front adiabat, and $\gamma = 5/3$ is the adiabatic index. For a fixed laser wavelength, the ablation pressure depends on the laser intensity $p_a \sim I^{2/3}$, leading to a scaling of the ablation velocity $V_a \sim S_a^{3/5} I^{-1/15}$, which is almost solely dependent on the ablation-front adiabat. The ablation velocity increases for larger values of the adiabat, leading to lower growth rates and improved stability. The 1-D capsule performance degrades, however, as the adiabat increases. Indeed, the energy required for ignition[3] in a 1-D implosion is approximately proportional to S_{dec}^2, and the shell areal density at stagnation decreases for larger S_{dec} (here S_{dec} is the in-flight shell adiabat at the beginning of the deceleration phase).

It is important to emphasize that the 1-D capsule performance is affected by the shell adiabat at the beginning of the deceleration phase (S_{dec}) only when the laser is turned off and mass ablation off the outer shell surface has ceased. Since a large portion of the shell mass is ablated off during the acceleration phase, the 1-D shell performance during the deceleration phase depends on the adiabat of the unablated shell. On the contrary, the ablative stabilization during the acceleration phase depends on the adiabat at the ablation front (S_a), that is, the adiabat of the ablated portion of the shell. It follows that a desirable adiabat shape would exhibit a minimum on the rear surface and a maximum on the ablation front. The idea of adiabat shaping was first introduced in Ref. 4, where the shaping is induced by the interaction of soft x rays with an ablator material having multiple absorption lines and radiation penetration depths. The first target design of such kind[5] makes use of the x rays produced by a thin gold overcoat and by the carbon radiation in a wetted-foam ablator. Even though such a clever design[4,5] can produce the desired shaping, significant complications arise from the target-manufacturing aspect, based on wetted-foam technology.

In this article, we show that it is possible to shape the shell adiabat with only a minor modification of the laser pulse without requiring any change to the shell structure. Adiabat shaping can easily be performed by relaxing the density profile of the shell with a weak laser prepulse followed by a power shutoff. The adiabat is shaped when the main pulse is turned on, driving a strong shock through the relaxed profile. The adiabat profiles are usually steep, leading to a large increase in the ablation velocity. We refer to this technique as relaxation (RX). A good degree of adiabat shaping can also be accomplished by using a strong prepulse driving a very strong shock in the shell. When the laser power is lowered, the shock decays, leaving behind a shaped-adiabat profile. Shaping by a decayed shock (DS) was first proposed in Ref. 6 by Goncharov et al. and is described only briefly here for the purpose of comparison. We refer to Ref. 6 for a more detailed description of the DS technique. Instead, we focus our attention primarily on the RX adiabat shaping requiring only a weak prepulse and therefore easily implementable on current laser systems. Another advantage of the RX technique is that the main pulse starts with a high-intensity foot leading to a low contrast ratio for the main pulse laser power, better conversion efficiency, and therefore

more energy on target. Unlike the DS, the RX-induced adiabat shape is not unique and can be tuned by changing the laser prepulse and main pulse. The benefits of RX shaping have also been confirmed by a series of recent simulations by Perkins[7] *et al.* and may also explain the improved stability observed in the simulations of Lindl and Mead.[8] Furthermore, the use of a laser prepulse may also lead to a reduced level of imprinting.[9]

Analysis of Adiabat Shapes

Both the DS and RX techniques require a prepulse (strong and weak, respectively) launching a decaying strong shock in the shell. We assume that the prepulse produces a constant pressure (P_{prep}) of duration (t_{prep}). The strong shock launched by the pressure $p_* = P_{\text{prep}}$ compresses the shell material to a density $\rho_* \simeq 4\,\rho_0$ (here ρ_0 is the initial shell density) and sets the adiabat of the shocked material to a constant value $S_* = p_*/\rho_*^{5/3}$. After the interval t_{prep}, the laser intensity (and therefore the applied ablation pressure) is greatly reduced, causing a rarefaction wave to propagate from the ablation front toward the shock front. We define with $t = 0$ the time corresponding to the end of the prepulse and launching of the rarefaction wave. Since the leading edge of the rarefaction wave travels faster than the shock, the shock front is overtaken by the rarefaction wave at time $t_* \simeq 0.81\,t_{\text{prep}}$ corresponding to an areal density $m_* = t_*\sqrt{\gamma p_* \rho_*}$. After the shock is overtaken by the rarefaction wave ($t > t_*$), both the shock strength and the adiabat of the shocked material decrease. The analysis is greatly simplified by working in the Lagrangian frame of reference and by using the areal density $m = \int_{r_0}^{r} \rho(r',t)dr'$ as the spatial coordinate, with r and r_0 representing the position of the fluid elements and the outermost Langrangian point, respectively.

For the DS case, it is important to determine the entropy shape caused by the decaying shock. Using the normalized variables ρ/ρ_*, p/p_*, t/t_*, $u/\sqrt{\gamma p_*/\rho_*}$, and m/m_*, it is easy to show that the equations of motion and the initial and boundary conditions depend only on γ, suggesting that the normalized adiabat $\hat{S} = S/S_*$ is a universal function of $z = m/m_*$ with a shape depending only on γ. It follows that $\hat{S}(z)$ can be determined once and for all from a single one-dimensional simulation. For $\gamma = 5/3$, the normalized adiabat $\alpha \equiv P(\text{Mb})\big/2.18\,\rho\big(g/\text{cm}^3\big)^{5/3}$ is flat for $m < m_*$ and follows approximately a power law for $m > m_*$:

$$\alpha_{m_* < m < m_{\text{sh}}} \approx \alpha_b\left(m_{\text{sh}}/m\right)^{1.3}, \qquad (1)$$

where m_{sh} is the total shell areal density and α_b is the rear-surface adiabat that determines the 1-D performance. It is

important to notice that while the adiabat shape is independent of the prepulse characteristics, the front-surface adiabat $\alpha_f = \alpha_b\left(m_{\text{sh}}/m_*\right)^{1.3}$ increases by lowering m_*. This can be accomplished by a short, intense prepulse. After the strong prepulse, the standard main pulse immediately follows, driving the shell to the desired implosion velocity.

For the RX case, the prepulse shock is weaker than the DS case, leading to a negligible entropy variation. During the power shutoff, the rarefaction trailing edge expands outward and the shocked material relaxes. Both the pressure and density profiles develop a monotonically increasing profile up to the shock front. The adiabat shaping occurs later in time when the laser is turned on again and the foot of the main pulse starts (see Fig. 94.19 for a typical laser pulse). At this time (t_{foot}) a strong shock is launched and supported by the pressure of the foot of the main pulse (P_{foot}). The shock travels through the relaxed profiles and initially interacts with the low-pressure material of the rarefaction trailing edge. Because of the large pressure ratio before and after the shock front, the shock strength is initially very high and the shell's outer surface is set on a high adiabat. As the shock travels up the pressure (and density) profile, the pressure of the unshocked material increases and the shock strength decreases, leading to a lower adiabat. When the shock driven by the main pulse merges with the shock launched by the prepulse at the shell's rear surface, the adiabat acquires the desired shape with large values on the outer surface and low values on the inner surface.
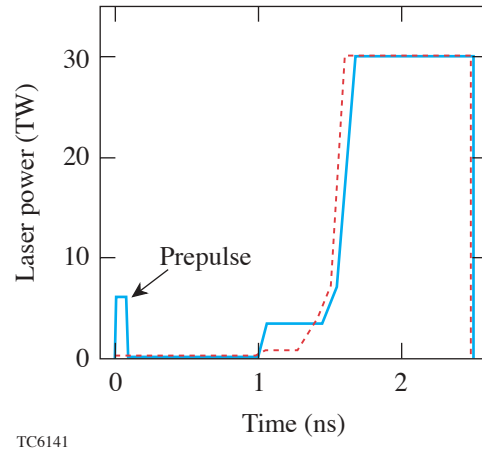

TC6141

Figure 94.19
Laser pulse for a flat adiabat (dashed) and for adiabat shaping by relaxation (RX) (solid).

The adiabat shape can be calculated analytically for the two limiting cases: (a) a long prepulse launching a rarefaction wave that catches the shock just before the shell's rear surface ($m_* \simeq m_{\mathrm{sh}}$) and (b) a short prepulse with a rarefaction wave catching the shock near the front surface ($m_* \ll m_{\mathrm{sh}}$). In case (a), the relaxed density profile just before the main shock launch follows a power law of the areal density $\rho \sim m^{0.75}$. The propagation of the main shock through such a profile can be calculated analytically, leading to the following entropy profile after the main shock:

$$\alpha \approx \alpha_b \left(m_{\mathrm{sh}}/m\right)^{1.25}. \tag{2}$$

Observe that the adiabat shape follows a power law similar to the decaying shock case [Eq. (1)] except for the absence of the flat-adiabat region for $m < m_*$, therefore extending the large adiabat profile through the entire shell. In case (b), the relaxed density profile just before the main shock can also be approximated with a power law of the areal density but with a higher exponent $\rho \sim m^{1.45}$ for $m > m_*$ (here $m_* \ll m_{\mathrm{sh}}$). When the exponent exceeds unity, the hydro equations for the main shock propagation cannot be solved exactly. Instead, an approximate solution can be found by assuming that the pressure profile behind the shock is linear in the areal density. A straightforward manipulation of the hydro equations leads to the following adiabat shape behind the main shock:

$$\alpha = \alpha_b \left(\frac{m_{\mathrm{sh}}}{m}\right)^{2.4} \frac{1 + \Theta(m/m_*)}{1 + \Theta(m_{\mathrm{sh}}/m_*)},$$

$$\tag{3}$$

$$\Theta(\xi) = \frac{2.64\,\xi^2 - 8.1\xi^{1.45} + 6.4\,\xi - 1}{\left(1 - \xi\right)^2}.$$

Observe that the adiabat profile given by Eq. (3) approaches the power law $\alpha \sim m^{-2.4}$ for $m_* \to 0$ and is quite steeper than the one produced by the decaying shock [Eq. (1)], leading to larger values of the adiabat at the ablation front and larger ablation velocities.

Prepulse Design Formulas

The shock-merging condition on the rear surface is a necessary condition for an optimum RX shaping. Indeed, it is easy to show that when the two shocks (main and prepulse) merge inside the shell, the transmitted shock sets the rear surface on

an adiabat that is about five times larger than the desired value. Furthermore, if the prepulse shock reaches the rear surface before the main shock, then the back of the shell relaxes and the main shock travels through a decreasing pressure profile, acquiring strength and setting the rear surface on a very high adiabat. The condition of shock merging on the rear surface is an important constraint for a successful adiabat shaping. Assigning the rear-surface adiabat and satisfying the shock-merging requirement are the two conditions needed to determine the starting time and the intensity (i.e., pressure) of the foot of the main laser pulse. A dimensional analysis indicates that four dimensionless parameters can be identified: $\hat{T} = t_{\mathrm{foot}}/t_{\mathrm{prep}}$, $\hat{P} = P_{\mathrm{foot}}/P_{\mathrm{prep}}$, $\hat{m} = m_*/m_{\mathrm{sh}}$, and $\hat{S} = S_*/S_b$, where $S_* = p_*/\rho_*^{5/3}$ and the $*$ indicates the prepulse hydrodynamic variables. Using the two constraints and a set of numerical simulations in the strong shock regime with different prepulse durations and prepulse pressures, we have constructed a power-law relation among the dimensionless parameters ($\hat{P} \sim \hat{m}^{0.26}\hat{S}^{0.95}$ and $\hat{T} \sim \hat{S}^{0.08}/\hat{m}^{1.76}$), leading to the following simple formulas:

$$P_{\mathrm{foot}}^{\mathrm{Mb}} \approx 22.5 \left[\frac{100}{\Delta_{\mathrm{sh}}^{\mu m}}\right]^{0.26} \left(\frac{\alpha_b}{3}\right)^{0.95} \left[\frac{t_{\mathrm{prep}}^{\mathrm{ns}}}{0.1}\right]^{0.26}$$

$$\left[\frac{P_{\mathrm{prep}}^{\mathrm{Mb}}}{10}\right]^{0.18} \left[\frac{\rho_0^{\mathrm{g/cm}^3}}{0.25}\right]^{1.45},$$

$$\tag{4}$$

$$t_{\mathrm{foot}}^{\mathrm{ns}} \approx 2.5 \left[\frac{\Delta_{\mathrm{sh}}^{\mu m}}{100}\right]^{1.76} \left(\frac{\alpha_b}{3}\right)^{0.08}$$

$$\left[\frac{0.1}{t_{\mathrm{prep}}^{\mathrm{ns}}}\right]^{0.76} \left[\frac{10}{P_{\mathrm{prep}}^{\mathrm{Mb}}}\right]^{0.96} \left[\frac{\rho_0^{\mathrm{g/cm}^3}}{0.25}\right].$$

Observe that the prepulse characteristics can be arbitrarily chosen. For a given prepulse (P_{prep} and t_{prep}) and assigned shell thickness Δ_{sh}, density, and rear-surface adiabat (α_b), Eqs. (4) yield the starting time and initial intensity of the foot of the main pulse to within 20%.

Rayleigh–Taylor Growth Rates

1. Analytic Results

The growth rates Γ of the ablative RT in the presence of finite shell entropy gradients can be calculated using a sharp boundary approximation[10] that is valid for $kL_s \sim kd \gg 1$, where $k = \ell/R$ is the mode wave number, R is the in-flight radius, d is the target thickness, and $L_s = -S/S'$ is the entropy gradient scale length. The main difference from the standard ablative RT analysis[1,2,10] is in the spatial behavior of the perturbation, which decays slower in the overdense shell as a result of the finite entropy gradient $\tilde{v} \sim \exp\left(-k\hat{h}x\right)$ [instead of the standard exp $(-kx)$], where x is the distance from the ablation front and $\hat{h}$ is the solution to the following transcendental equation:

$$\hat{h}^2 \simeq 1 - \frac{g/\gamma L_s}{\left(\Gamma + k\hat{h}V_a\right)^2} + \frac{1}{\gamma k L_s}. \tag{5}$$

The last term on the right-hand side is negligible for $kL_s \gg 1$. It has been introduced *ad hoc* to recover the growth rates of long wavelengths that are not affected by either ablation or entropy gradients. Observe that the effect of finite entropy gradients *per se* is destabilizing $\left(\hat{h} < 1\right)$; however, the overall effect of adiabat shaping is stabilizing due to the large increase in ablation velocity. In the limit of $kd \gg 1$, the RT relation reduces to

$$A\Gamma^2 + B\Gamma kV_a + Ck^2V_a^2 - D\left(kg - k^2 V_a V_b\right) = 0, \tag{6}$$

where $A = \hat{h} + \hat{\rho}_b$, $B = \left(1 + \hat{h}\right)^2$, $C = \hat{h}\left(1 + \hat{h}\right)$, and $D = \left(1 - \hat{\rho}_b\right)$ with V_b and $\hat{\rho}_b$ representing the blowoff velocity and normalized density as defined in Eq. (6) of Ref. 2. Equations (5) and (6) must be solved simultaneously to determine the growth rate. It is important to note that an additional instability develops for finite L_s. This is a convective instability driven by the entropy gradients. The convective mode is internal to the shell and poses a serious threat to shell stability only when it grows sufficiently fast and develops the eigenfunction of a wide vortex stretching over a large portion of the shell. Its growth is typically much slower than the RT growth except for short wavelengths when $\Gamma \to \sqrt{g/\gamma L_s}$. Two-dimensional simulations (below) have indicated, however, that this mode grows to a very low amplitude simply because wide vortices are not seeded in the short-wavelength regime. Nevertheless, it is important to investigate the growth of the convective mode on a case-by-case basis since some target designs with extreme adiabat shaping may develop stronger convective instabilities.

2. Simulation Results

The results above are applied to a typical OMEGA cryogenic shell with an inner radius of 345 μm and a DT-ice layer of 85 μm. The shell is driven by a 30-kJ laser pulse (dashed curve in Fig. 94.19) yielding approximately 5.4×10^{14} neutrons on a flat, $\alpha \simeq 3$ adiabat according to a one-dimensional simulation performed with the code *DRACO*.[11] We apply adiabat shaping to the same shell through relaxation, keeping $\alpha_b \simeq 3$ on the rear surface. We use an 85-ps square prepulse with a pressure of 20 Mb and derive the corresponding mainpulse time and foot pressure from Eq. (4), yielding $P_{foot} \approx$ 25 Mb and $t_{foot} \approx 1.2$ ns. The pulse in Fig. 94.19 (solid) shows approximately such characteristics when simulated with *DRACO*. The resulting shaped adiabat is shown in Fig. 94.20 (solid) and compared with the theoretical predictions (dotted) from Eq. (3). The 1-D performances of the flat- and shaped-adiabat implosions in terms of yield and peak areal density are within 30% and 7%, respectively. The ablation velocity during the flattop portion of the laser pulse is shown in Fig. 94.21 indicating that the shaped-adiabat implosion exhibits a considerably larger ablation velocity. Figure 94.22 shows the reduction in growth rate versus the mode number ℓ, as given by a series of 2-D *DRACO* simulations. The growth rates are calculated toward the end of the laser flattop when the growth is clearly exponential. Figure 94.22 also shows a comparison with the theoretical growth rates from Eqs. (5) and (6) calculated with 1-D average values obtained from *DRACO*: $\langle g \rangle \simeq 345$ μm/ns^2 and $\langle V_a \rangle \simeq 4.2$ μm/ns^2 for the flat adiabat, and $\langle g \rangle \simeq 345$ μm/ns^2, $\langle V_a \rangle \simeq 6.4$ μm/ns and $L_s \simeq 6$ μm for the
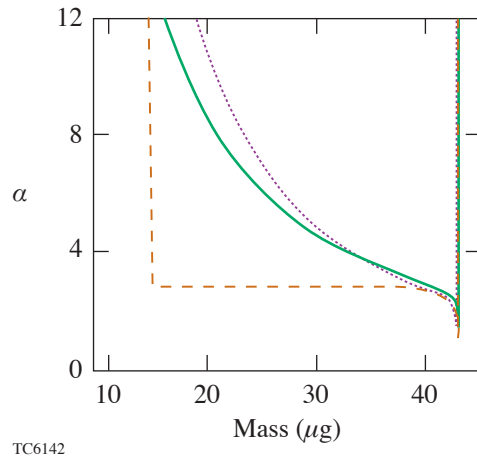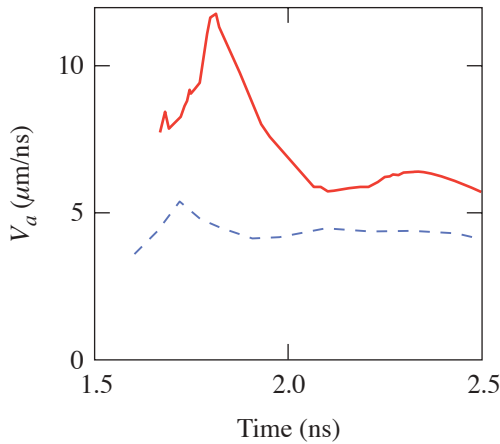

TC6142

Figure 94.20

Flat adiabat (dashed) and shaped adiabat (solid) profiles induced by the pulses of Fig. 94.19. The dotted curve is the result of Eq. (3).

shaped adiabat. The large reduction in growth rates induced by the high ablation velocity indicates that adiabat shaping can significantly improve the stability of imploding shells.

The anomalous behavior of the growth rate in modes $\ell \sim 200$ shown in Fig. 94.22 is due to a resonant interaction of the RT mode with the convective mode. When the vorticities of the convective and RT modes have the same sign, they add constructively, thereby amplifying the growth rate of the surface perturbation. Figure 94.23 shows radial lineouts of the vortic-

ity for the shaped mode $\ell = 200$ case at two times. The first snapshot (a) is at the beginning of the convective–RT interaction. One can clearly see the RT mode at the ablation front and a larger amplitude convective mode just inside the ablation front. The second snapshot (200 ps later) shows a significant amplification of the RT vorticity as the ablation surface penetrates into the convective cell. This interaction occurs to varying extents at modes of all wavelengths; however, it is most noticeable in regimes where neither mode dominates. Note that under the right circumstance, this convective–RT
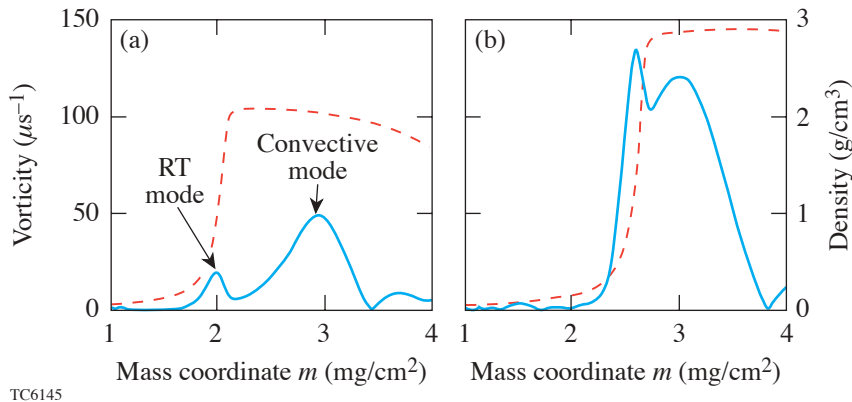

TC6143
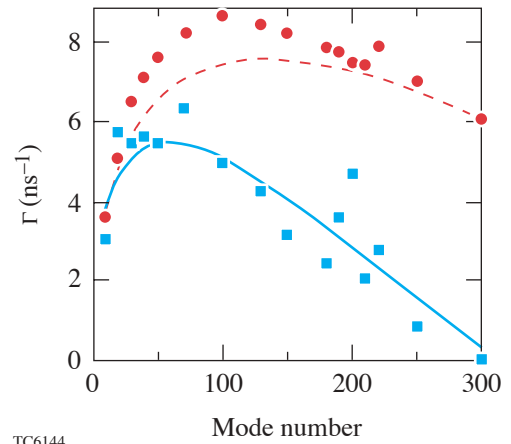
Figure 94.21
Time evolution of the ablation velocities during the power flattop for the flat-adiabat (dashed) and shaped-adiabat (solid) implosions.

TC6144

Figure 94.22
RT growth rates versus mode number ℓ for the flat adiabat from *DRACO* (circles) and from Eqs. (5) and (6) (dashed) and for the shaped adiabat from *DRACO* (squares) and from Eqs. (5) and (6) (solid).

TC6145

Figure 94.23
Vorticity (solid line) and density (dashed line) for the shaped-adiabat, $\ell = 200$ case (a) at the beginning of the convective–RT mode interaction and (b) 200 ps later.

interaction may also be destructive, leading to lower-than-expected growth rates.

We have developed the theoretical basis (adiabat profiles, laser pulses, RT-growth rates) for laser-induced adiabat shaping by relaxation and have shown that RT growth rates can be reduced without significantly degrading 1-D capsule performances.

ACKNOWLEDGMENT

REFERENCES

1. S. E. Bodner, Phys. Rev. Lett. **33**, 761 (1974); H. Takabe *et al.*, Phys. Fluids **28**, 3676 (1985); J. Sanz, Phys. Rev. Lett. **73**, 2700 (1994).

2. R. Betti, V. N. Goncharov, R. L. McCrory, and C. P. Verdon, Phys. Plasmas **5**, 1446 (1998).

3. M. C. Herrmann, M. Tabak, and J. D. Lindl, Nucl. Fusion **41**, 99 (2001); A. Kemp, J. Meyer-ter-Vehn, and S. Atzeni, Phys. Rev. Lett. **86**, 3336 (2001); R. Betti, K. Anderson, V. N. Goncharov, R. L. McCrory, D. D. Meyerhofer, S. Skupsky, and R. P. J. Town, Phys. Plasmas **9**, 2277 (2002).

4. J. H. Gardner, S. E. Bodner, and J. P. Dahlburg, Phys. Fluids B **3**, 1070 (1991).

5. S. E. Bodner *et al.*, Phys. Plasmas **7**, 2298 (2000); L. Phillips *et al.*, Laser Part. Beams **17**, 225 (1999).

6. V. N. Goncharov, "Improved Performance of Direct-Drive ICF Target Designs with Adiabat Shaping Using an Intensity Picket," to be published in Physics of Plasmas.

7. L. J. Perkins, M. Tabak, J. Lindl, D. Bailey, J. Harte, A. Schmitt, S. Obenschain, and R. Betti, Bull. Am. Phys. Soc. **47**, 101 (2002).

8. J. D. Lindl and W. C. Mead, Phys. Rev. Lett. **34**, 1273 (1975).

9. T. J. B. Collins and S. Skupsky, Phys. Plasmas **9**, 275 (2002).

10. A. R. Piriz, J. Sanz, and L. F. Ibañez, Phys. Plasmas **4**, 1117 (1997).

11. D. Keller, T. J. B. Collins, J. A. Delettrez, P. W. McKenty, P. B. Radha, B. Whitney, and G. A. Moses, Bull. Am. Phys. Soc. **44**, 37 (1999).

Demonstration of a Room-Temperature Single-Photon Source for Quantum Information: Single-Dye-Molecule Fluorescence in a Cholesteric Liquid Crystal Host

Introduction

Quantum information in the form of quantum communications and quantum computing (see Refs. 1–33) is currently an exceedingly active field. Numerous theoretical concepts promise powerful quantum-mechanics-based tools[34] that, to date, wait for realization pending the arrival of reliable hardware.[1–33] A *single-photon source* (SPS)[35] that efficiently produces photons with *antibunching* characteristics[36–38] is one such pivotal hardware element for quantum information technology. Using an SPS, secure quantum communication will prevent any potential eavesdropper from intercepting a message without the receiver noticing.[25,30,39–41] In another implementation, an SPS becomes the key hardware element for quantum computers with linear optical elements and photodetectors.[42–52] Again, its practical realization is held back in part because of the difficulties in developing robust sources of antibunched photons on demand. In spite of several solutions for SPS's presented in the literature, significant drawbacks remain. The drawbacks are the reason for current quantum communication systems being baud-rate bottlenecked, causing photon numbers from ordinary photon sources to attenuate to the single-photon level (~0.1 photon per pulse on average).[25,39,41] An efficient (with an-order-of-magnitude-higher photon number per pulse) and reliable light source that delivers a train of pulses containing one, and only one, photon is a very timely challenge. To meet this challenge, several issues need to be addressed, from achieving full control of the quantum properties of the source to easy handling and integrability of these properties in a practical quantum computer and/or communication setup. In addition, in quantum information systems it is desirable to deal with single photons synchronized to an external clock, namely, *triggerable* single photons.[53] *Polarization states* of single photons are also important since they enable polarization-qubit encoding of information.

The critical issue in producing single photons in another way than by trivial attenuation of a beam is the *very low concentration of photon emitter*s dispersed in a host, such that within a laser focal spot only one emitter becomes excited, emitting only one photon at a time. In initial demonstrations of resonance-fluorescence photon antibunching,[54] SPS's possessed a random photon-emission time.[54–63] Single photons "on demand," i.e., triggerable single photons, were obtained only recently.[53,64–76] De Martini *et al.*[64] used an active microcavity excited by a mode-locked laser. In experiments by Kim *et al.*,[65] Imamoglu *et al.*,[66] and Moreau *et al.*,[67] a single-photon turnstile device utilized Coulomb blockade of tunneling for electrons and holes in a mesoscopic double-barrier *p–n* junction. Single photons were generated at the modulation periodicity of the junction voltage. Michler *et al.*[68] and Santory *et al.*[69] demonstrated single-photon devices using pulsed-laser excitation of a single AlGaAs quantum dot. Electrically driven single photons (also at cryogenic temperatures as in Refs. 65–69) were obtained by Yuan *et al.*[70,71] Experiments by Brunel *et al.*,[72] Lounis and Moerner,[73] and Treussart *et al.*[74] were based on an entirely different system, namely single dye molecules embedded at low concentration within organic single-crystal platelets or covered by a polymer layer. Single photons were triggered either by a combination of cw laser excitation and an electronic signal[72] or by short-pulse laser irradiation.[73,74] Most of these sources, e.g., Refs. 65–71, operate reliably only at liquid He temperature—a major impediment to widespread use. To date, three approaches are known to be eligible for *room-temperature* SPS implementation, two inorganic and one organic. The first inorganic, room-temperature approach involves a mono-/polycrystal diamond and one of its color centers.[59–61,75,76] The second inorganic approach uses single-colloidal CdSe/ZnS quantum dots (Michler *et al.*,[77] Lounis *et al.*,[78] and Messin *et al.*[79]). The alternative, organic approach,[58,62,63,72–74] based on numerous previous experiments around liquid-He temperature,[80–83] uses a vapor-phase-sublimated host crystal of para-terphenyl doped with an emitting species, terrylene.[62,73]

As acceptable as these approaches may be strictly on quantum-optics grounds, all suffer from shortcomings that will delay quantum information from gaining a technology foothold in the near future. None of these sources is used in practical, civilian systems. Their specific shortcomings include the following: (1) Polarization of single photons varies

from one emitter to another (nondeterministic); (2) single photons are produced with *very low efficiency* and *polluted* by additional photons at about the same frequency from the host material;[53] and (3) alternatives such as color centers in diamond and colloidal CdSe/ZnS quantum dots possess unacceptably long fluorescence lifetimes (for instance, the diamond color center has a 11.6-ns and 22.7-ns fluorescence lifetime in mono- and polycrystal, and CdSe-ZnS quantum dots have a fluorescence lifetime of ~22 ns).

The organic, room-temperature SPS approach is based on using a chromophore molecule as the single emitter. The key advantage of chromophore molecules is that their excited-state lifetime of only a few nanoseconds permits excitation repetition rates above ~100 MHz. In *amorphous* media such molecules tend to be *unstable*: they are blinking at various characteristic time intervals, change their spectral behavior, and can be easily bleached. Recently, however, single terrylene molecules have been doped into *p*-terphenyl molecular *crystals* (10^{-11} moles of terrylene per mole of *p*-terphenyl) prepared by a sublimation procedure that produced tiny platelets.[62,73] In this host, the chromophore is protected from exposure to diffusing quenchers (such as oxygen) and benefits from strong phonon emission into the host, preventing rapid thermal decomposition of the chromophore under intense irradiation. In Ref. 73 it was found that for "thick" *p*-terphenyl crystals (~10 μm), this system becomes extremely photostable, allowing hours of continuous illumination of individual molecules without photobleaching. It assures long-term spectral stability and reproducibility from one terrylene absorber to the next.[84,85] Pumped by periodic, short-pulse laser radiation, single photons were generated at predetermined times at pump-pulse-repetition rates within the accuracy of the emission lifetime (~3.8 ns). Technical implementation of this system is difficult because these monoclinic, sublimation-produced microcrystals are stress sensitive and fragile. In addition, terrylene's molecular dipole moment in the *p*-terphenyl host crystal takes on an orientation perpendicular to the platelet's surface (i.e., perpendicular to the incident light's E field).[73] This, in turn, leads to poor coupling with the polarized excitation light, prompting poor fluorescence emission even at high excitation intensities (saturation intensity is about 1 MW/cm^2 at room temperature). In spite of the elegance of the terrylene/*p*-terphenyl experiments, this technology must be considered unrealistic for practical application. Its weak point is also a background from "ordinary photons" from out-of-focus molecules or Raman scattering because of the very high pumping intensities required. Emitted photons are not polarized *deterministically* (there is no known efficient method for aligning

rapidly a multitude of micrometer-sized, monoclinic crystallites relative to one another). Note that noncrystalline, amorphous hosts, e.g., polymers,[63] neither (1) offer the same spectral stability in single-molecule emission even in the case of terrylene, nor (2) provide long-time protection against bleaching. To date, *no crystal hosts* other than the fragile, sublimated *p*-terphenyl flakes have been proposed in *single-molecule room-temperature* experiments.

This article describes some new approaches toward implementing an efficient, deterministically polarized SPS on demand: (1) using *liquid crystal hosts* (including liquid crystal polymers) to preferentially align the emitter molecules for maximum excitation efficiency (deterministic molecular alignment will also provide deterministically polarized output photons); (2) using planar-aligned cholesteric (chiral-nematic) liquid crystal hosts[86] as 1-D photonic-band-gap microcavities[87–91] tunable to the dye fluorescence band;[92–93] and (3) using liquid crystal technology to prevent dye bleaching.

Cholesteric-Liquid-Crystal, 1-D Photonic-Band-Gap Materials

In planar cholesterics (Fig. 94.24) that for visualization purposes can be described as consisting of, but in reality not comprising, a layered structure, the axes of the molecular director (far-right set of arrows in Fig. 94.24) rotate monotonically to form a periodic helical structure with pitch P_0.[86] With few exceptions, liquid crystal media are non-chiral and require
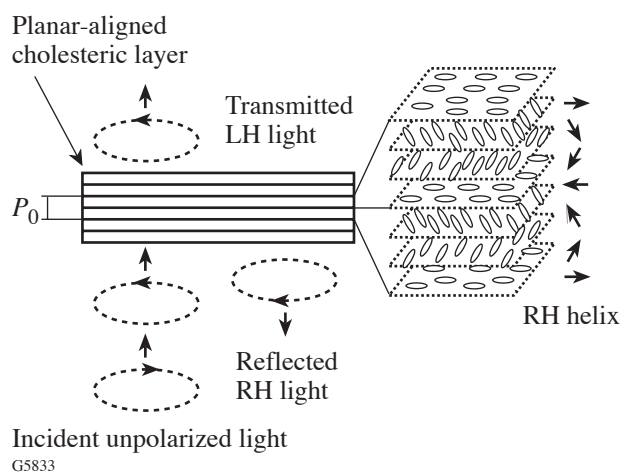
Figure 94.24
Transmission and reflection by a cholesteric liquid crystal layer near selective reflection conditions.

additives to induce the chiral order. Dependent on the chirality-inducing additive, the final structure may show either a right- or a left-handed sense of rotation.

When a solid cholesteric is flipped on its side and inspected by a high-resolution tool such as an atomic force microscope, the periodic pitch becomes observable through height variations along the helical axis. For instance, Fig. 94.25 shows such a topography for a Wacker cyclo-tetrasiloxane-oligomer cholesteric liquid crystal (OCLC)[94] platelet. Periodic stripes in the image correspond to one-half of the pitch length.
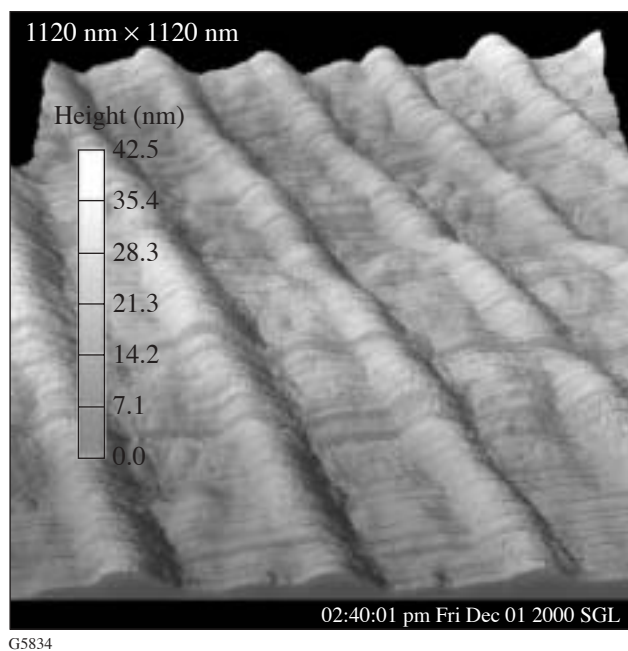

G5834

Figure 94.25
Perspective view of the AFM topographical image of a planar-aligned Wacker OCLC layer (1.12-μm $\times$ 1.12-μm scan).

For liquid crystal thicknesses ≥ 10 μm, the reflectance of normally incident, circularly polarized light with electric-field vector rotation opposite to the rotation of molecules in the helical structure (Bragg condition) approaches 100% within a band centered at $\lambda_0 = n_{av}P_0$, where $n_{av} = (n_e + n_0)/2$ is the average of the ordinary and extraordinary refractive indices of the medium. This is the so-called selective reflection of cholesteric liquid crystals. The bandwidth is $\Delta\lambda = \lambda_0 \Delta n / n_{av}$, where $\Delta n = n_e - n_0$. Such a periodic structure can also be viewed as a 1-D photonic crystal, with a bandgap within which propagation of light is forbidden. For emitters located within such a structure, the rate of spontaneous emission is suppressed within the spectral stop band and enhanced near the band

edge.[95] Several groups have reported lasing in photonic band-gap material hosts, including cholesteric liquid crystals,[95–98] with spectral emission features underscoring the validity of this concept. Generation of strongly circularly polarized photoluminescence from planar layers of glass-forming chiral-nematic liquid crystals was also reported.[92–93] Light-emitting dopants at 0.2-wt% concentration were embedded in these liquid crystals. The degree of circularly polarized photoluminescence, i.e., its asymmetry,[92–93]

$$G_e \equiv 2(I_L - I_R)/(I_L + I_R), \qquad (1)$$

where I_R and I_L denote the right- and left-handed emission intensity, respectively (see Fig. 94.26), was found to be equal to maximum value [~ -2 (Refs. 92 and 93)].
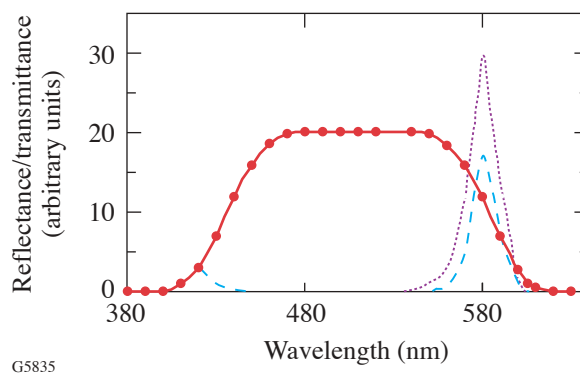

G5835

Figure 94.26
Tutorial schematic of the wavelength dependence between the photonic stop-band reflectance (solid line), dye photoluminescence intensity (dotted line), and photoluminescence polarization asymmetry G_e inside the band (dashed line).

Matching of λ_0 of cholesteric liquid crystal with a dye-fluorescence band will be the subject of a future article. In our current experiments, Wacker OCLC (see Fig. 94.27) with λ_0 outside the terrylene-dye-fluorescence band was doped with terrylene (Fig. 94.28) at an extremely low concentration such that the final sample contained only a few molecules per μm^2 irradiation area. Cast from solution on single microscope cover-glass slips, the samples ranged in thickness from ~50 nm to several micrometers. In some experiments, we also used terrylene-doped layers of monomeric cyanobiphenyl liquid crystal 5CB with chiral additive CB15. The 5CB liquid crystal layers were placed between two microscope cover-glass slips separated by glass-bead spacers.

To minimize false fluorescence contributions by contaminants during single-molecule-fluorescence microscopy, rigorous cleaning of glass substrates is mandatory. For this purpose, the microscope glass slips (Corning, 0.17-mm thickness) were etched in a piranhas solution and rinsed in deionized water. Proper terrylene concentration for single-molecule fluorescence microscopy was established by iterative trial and error. In sequential dilution steps of terrylene in chlorobenzene solvent, solutions were spun onto glass slips, and for each concentration, confocal fluorescence microscopy determined the final emitter concentration per irradiation volume. Once single molecules were predominantly observed, the dilution endpoint was reached. This final terrylene solution was mixed with Wacker OCLC starting material (8% weight concentra-

tion of oligomer). For planar alignment, standard buffing procedures could not be employed at the risk of introducing dirt particles. Two alternate methods were found satisfactory: either the film was *flow aligned* by letting the OCLC solution run down a vertically inclined glass slip, or a special glass cylinder was rolled unidirectionally across a spin-coated OCLC layer heated to the isotropic state. Figure 94.29 shows an optical microscope image of a planar-aligned OCLC layer with "oily streak" defects typical for a planar structure of cholesteric liquid crystals (both monomeric and oligomeric/polymeric).[99–101] The influence of the oily streak defects on a single-molecule fluorescence will be considered in future work. We mention them here to show evidence of a planar structure of OCLC prepared by our group.
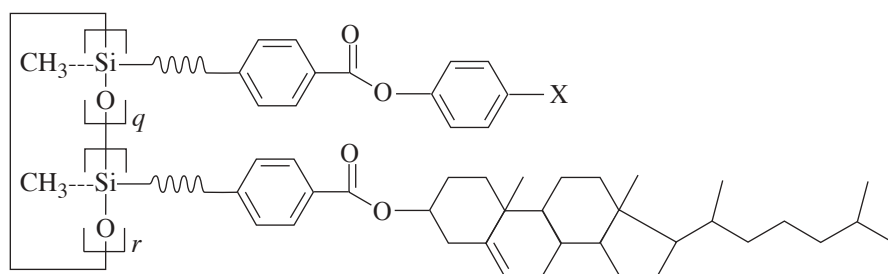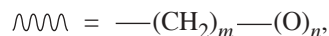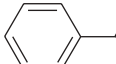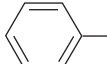

Figure 94.27
Molecular structure of Wacker siloxane OCLC (from Ref. 94).

$\wedge\wedge\wedge\wedge$ = —$(CH_2)_m$—$(O)_n$,

where m = 3, 4, 5, 6, 8, 10 and n = 0, 1;

$q + r$ = 3, 4, 5, 6, or 7 and $q/(q + r)$ = 0 to 1

X = Cl, OMe, O$(CH_2)_3$H, ⬡—⬡—CN or ⬡—$(CH_2)_p$H, where p = 2, 4, or 5

G5836

Figure 94.28
Molecular structure of terrylene dye.

|← —— 1 mm —— →|

G5838

Figure 94.29
Optical microscopy of "oily streak" defects of planar-aligned Wacker OCLC layer.

Experimental Setup for Single-Dye-Molecule Fluorescence Microscopy and Antibunching Correlation Measurements

Photon antibunching correlation measurements are carried out using the setup shown in Figs. 94.30 and 94.31. The terrylene-doped liquid crystal sample is placed in the focal plane of a 0.8-N.A. microscope objective (Witec alpha-SNOM platform). The sample is attached to a piezoelectric, XYZ translation stage. Light emitted by the sample is collected by a confocal setup using a 1.25-N.A., oil-immersion objective together with an aperture formed by the core of a multimode optical fiber. The cw, spatially filtered (through a single-mode fiber), linearly polarized (contrast 10^5:1), 532-nm diode-pumped Nd:YAG laser output excites single molecules. In focus, the intensities used are of the order of several kW/cm^2. The collection fiber is part of a non-polarization-sensitive 50:50 fiber splitter that forms the two arms of a Hanbury Brown and Twiss correlation setup[102] (Fig. 94.31). Residual, transmitted excitation light is removed by two consecutive dielectric interference filters yielding a combined rejection of better than six orders of magnitude at 532 nm. The fluorescence band maximum of terrylene molecules used in our experiments lies in a spectral region near 579 nm with a bandwidth of ~30 nm.

Photons in the two Hanbury Brown and Twiss arms are detected by identical, cooled avalanche photodiodes in single-photon-counting Geiger mode. The time interval between two consecutively detected photons in separate arms is measured by a 68-ns-full-scale time-to-digital converter using a conventional start–stop protocol. Within this converter's linear range, the time uncertainty in each channel corresponds to 25 ps.

It has been proven experimentally (see, e.g., Refs. 62 and 63) that a very good approximation of the autocorrelation function $g^{(2)}(\tau)$ comes directly from the coincidence counts (event distribution) $n(\tau)$, for relatively low detection efficiency and therefore low counting rate. That is why we consider that $n(\tau)$ is proportional to the autocorrelation function $g^{(2)}(\tau)$. For single photons, $g^{(2)}(0) = 0$, indicating the absence of pairs, i.e., antibunching.

Experimental Results

1. Single-Dye-Molecule Fluorescence in a Cholesteric Liquid Crystal Host

Figure 94.32 shows terrylene-dye-molecule-fluorescence images obtained by confocal fluorescence microscopy: (a) single terrylene molecules embedded in a Wacker OCLC host ($\lambda_0 = 2.2~\mu$m); (b) clusters of terrylene molecules spin

G5839

Figure 94.30
Witec alpha-SNOM microscope with a laser.
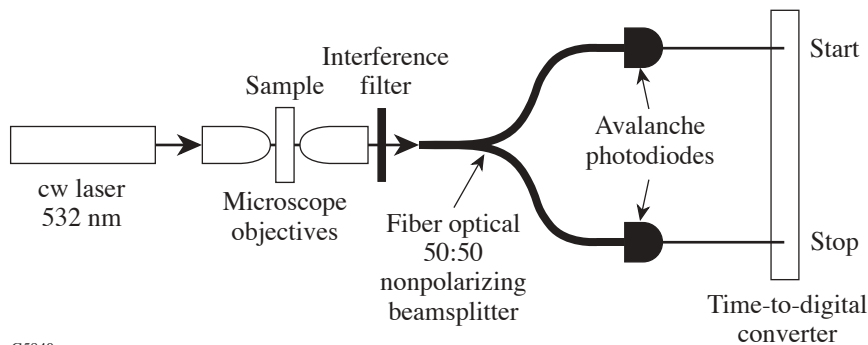
G5840

Figure 94.31
Experimental setup for photon antibunching correlation measurements.

coated from chlorobenzene solution onto a bare cover-glass slip. For both images, the scan direction is from left to right and line by line from top to bottom. The scan dimensions are $10\,\mu m \times 10\,\mu m$. Most single molecules in our samples exhibited fluorescence blinking in time, with a period ranging from several milliseconds up to several seconds. In Fig. 94.32, this "blinking" behavior by single molecules manifests itself as bright and dark horizontal stripes in image (a). These features are absent in emission images from clusters (b).

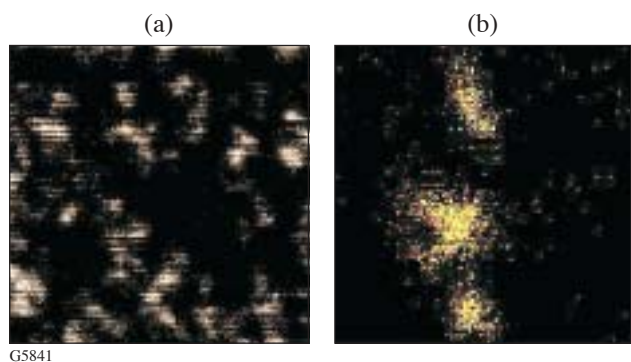(a)   (b)

G5841

Figure 94.32
Terrylene molecule fluorescence: (a) single-molecule fluorescence from the OCLC host; (b) fluorescent-molecule clusters on a bare surface. Resolution of the optical system is ~0.5 μm.

Blinking is a common phenomenon and convincing evidence of the single-photon nature of the source. Several mechanisms are suggested to explain the blinking behavior: for instance, "shelving" (triplet blinking) to the long-living state, and fluctuations in the photo-physical parameters of the molecule and its local environment.[103] By modeling the molecule as a three-level system (singlet ground state S_0, excited-state level S_1, and triplet state T_1) as depicted in Fig. 94.33, "triplet blinking" can be explained by a population of T_1 level that is often a dark state in fluorescent dyes.
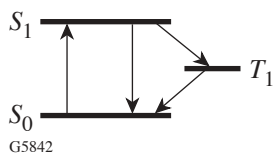

S_1

T_1

S_0

G5842

Figure 94.33
Three-level model for molecular fluorescence.

2. Photon Antibunching Correlation Measurements

Figure 94.34 shows a coincidence-count histogram $n(\tau)$ from (a) host-free single terrylene molecules (left) and (b) an

assembly of many uncorrelated molecules within the excitation volume [Fig. 94.32(b)]. The scan speed is ~3 s per line (512 pixels). The left histogram exhibits a dip at $\tau = 0$. The measured signal-to-background ratio of our experiments ranges from 2 to 30, so the probability that a photon from the background triggers a coincidence with a photon from the molecule is very low. Because $n(\tau)$ is proportional to the autocorrelation function $g^{(2)}(\tau)$, $n(0) \sim 0$ means that $g^{(2)}(0) \sim 0$ in our experiments. Two fluorescence photons are not observed within an arbitrarily short time interval. This fluorescence antibunching is due to the finite radiative lifetime of the molecular dipole and is therefore clear proof that we observed the emission of one, and only one, molecule. The histogram on the right from a multiple of uncorrelated molecules shows no such dip at $\tau = 0$, i.e., no antibunching.
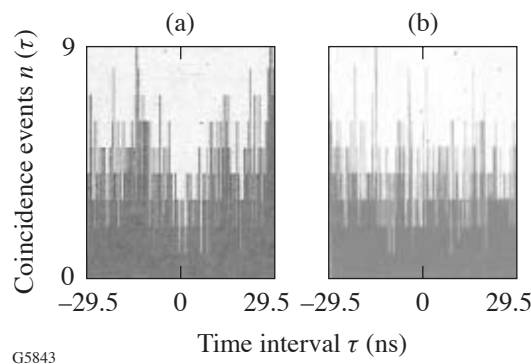

Figure 94.34
Histograms of conicidence events of single-terrylene-molecule fluorescence on a bare glass substrate (a) and from an assembly of several uncorrelated molecules within the excitation volume (b).

To eliminate any potential for leaked excitation light causing the dip at $\tau = 0$, the sample was replaced with a bare glass slide and one blocking interference filter was removed. The coincidence histogram for this condition is depicted in Fig. 94.35(b). No antibunching is observed. Two interference filters attenuated excitation light so strongly that no counts other than dark counts of avalanche photodiodes were observed during the same time interval.

Figure 94.36 shows the results of doping terrylene into liquid crystals. The histogram of coincidence events $n(\tau)$ [Fig. 94.36(a)] exhibits a dip at $\tau = 0$ indicating photon antibunching in the fluorescence of the single molecules in the Wacker OCLC host; no antibunching is observed in the fluorescence from an assembly of several uncorrelated molecules in the same host, different sample [Fig. 94.36(b)]. The histogram in Fig. 94.36(a) is noteworthy in that it demonstrates that

several *single* molecules can sequentially contribute to an antibunching histogram without loss of $\tau = 0$ contrast, as in practice the long integration time and competing molecule-bleaching events make obtaining an entire, good-contrast histogram from only one molecule too much a matter of luck. When the initial single molecule was bleached, the sample was advanced to another single molecule while the photon-correlation count continued. This finding is crucial for future device implementation.
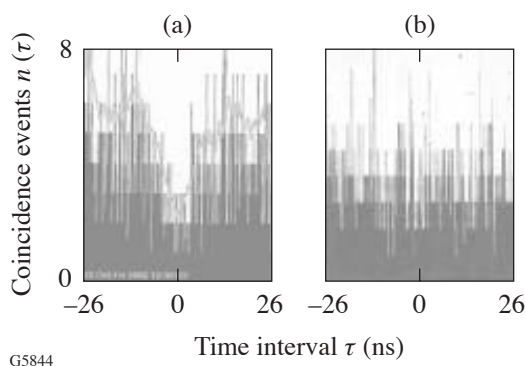

G5844

Figure 94.35
The histograms of concidence events of the single-terrylene-molecule fluorescence on a bare glass substrate (a) and of the radiation of excited green laser beam (b).
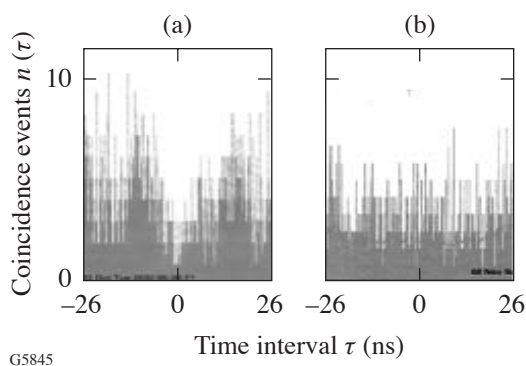

G5845

Figure 94.36
The histograms of concidence events of the single-terrylene-molecule fluorescence in a Wacker OCLC host (a) and of an assembly of several uncorrelated molecules (b).

3. Preventing Dye Bleaching in Liquid Crystal Hosts

Practical device implementation also depends on photo-chemical stability of both emitters and hosts. We increased terrylene fluorescence stability in monomeric liquid crystal hosts by saturating the liquid crystals with helium in a sealed

glovebox for 1 h. Oxygen, which is mostly responsible for dye bleaching, is displaced by helium during this procedure. Ground-state oxygen can form highly reactive singlet oxygen by quenching a triplet state of the dye. The singlet oxygen can then react with its surroundings, including dye molecules. Figure 94.37 shows fluorescence-bleaching results of terrylene molecules at two-orders-of-magnitude-higher concentration than in single-molecule experiments in different liquid crystal hosts: either immobilized in an oligomer cholesteric liquid crystal or dissolved in monomeric cyanobiphenyl 5CB saturated with helium (both at identical excitation intensity and identical terrylene volume concentration). Over the course of more than 1 h, *no* dye bleaching was observed in the *oxygen-depleted* liquid crystal host (upper curve).

G5846
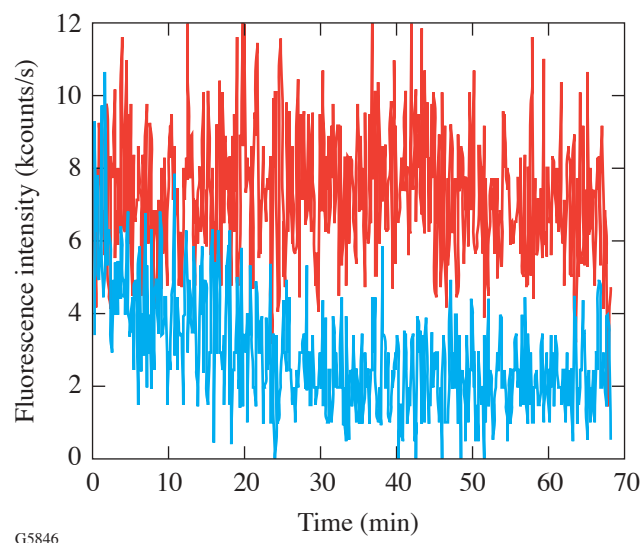
Figure 94.37
Fluorescence bleaching behavior of an assembly of terrylene molecules as a function of time and in two different liquid crystal hosts.

Dye bleaching is not a critical impairment for an efficient SPS, but it is an important factor for device simplicity and cost. When one molecule is bleached, the system can be rapidly realigned to utilize another isolated dye molecule, allowing practically continuous source action (see left histograms on Figs. 94.34–94.36).

Both well-known liquid crystal hosts are photochemically stable and do not absorb excitation light. In addition, incident intensities are too low for two-photon absorption processes. The absorption by a single molecule is insufficient for significant host heating.

Conclusion

A robust, room-temperature single-photon source based on fluorescence from a single dye molecule (fluorescence antibunching) was demonstrated for the first time for liquid crystal hosts. Planar-aligned, 1-D photonic-band-gap structures in dye-doped cholesteric oligomer were prepared. Avoiding bleaching of the terrylene dye molecules for excitation times >1 h was achieved by innovative preparation procedures. Liquid crystal hosts further increase the efficiency of the source (1) by aligning the dye molecules along a direction preferable for maximum excitation efficiency; and (2) by tuning a 1-D photonic-band-gap microcavity of planar-aligned cholesteric liquid crystal to the dye fluorescence band. Source-efficiency issues will be addressed in a subsequent article.

Future work will be directed toward increasing the efficiency, life, and polarization purity of the single-photon source by improved selection of dye, liquid crystal, and the photonic-band-gap structure matching with the dye-fluorescence band. A pulsed laser source will be used to create a real quantum cryptography system with a cholesteric-liquid-crystal, single-photon source on demand.

REFERENCES

1. M. A. Nielsen and I. L. Chuang, *Quantum Computation and Quantum Information* (Cambridge University Press, Cambridge, England, 2001).

2. J. Gruska, *Quantum Computing*, Advanced Topics in Computer Science Series (McGraw-Hill, London, 1999).

3. M. Brooks, ed. *Quantum Computing and Communications* (Springer, London, 1999).

4. C. P. Williams and S. H. Clearwater, *Explorations in Quantum Computing* (TELOS, Santa Clara, CA, 1998).

5. D. Deutsch, *The Fabric of Reality* (Penguin, London, 1998); T. Siegfried, *The Bit and The Pendulum: From Quantum Computing to M Theory—The New Physics of Information* (Wiley, New York, 2000).

6. S. Singh, *The Code Book: The Science of Secrecy from Ancient Egypt to Quantum Cryptography* (Anchor Books, New York, 2000).

7. J. R. Brown, *Minds, Machines, and Multiverse: The Quest for the Quantum Computer* (Simon & Schuster, New York, 2000).

8. P. Kumar, G. M. D'Ariano, and O. Hirota, eds. *Quantum Communication, Computing and Measurement 2* (Kluwer Academic/Plenum Publishers, New York, 2000).

9. D. Bouwmeester, A. K. Ekert, and A. Zeilinger, eds. *The Physics of Quantum Information: Quantum Cryptography, Quantum Teleportation, Quantum Computation*, 1st ed. (Springer, Berlin, 2000).

10. H.-K. Lo, T. Spiller, and S. Popescu, eds. *Introduction to Quantum Computation and Information* (World Scientific, Singapore, 1998).

11. S. L. Braunstein, *Quantum Computing: Where Do We Want to Go Tomorrow?* (Wiley-VCH, Weinheim, 1999).

12. S. L. Braunstein, H.-K. Lo, and K. Pieter, *Scalable Quantum Computers: Paving the Way to Realization*, 1st ed. (Wiley-VCH, Berlin, 2001).

13. G. J. Milburn, *The Feynman Processor: Quantum Entanglement and the Computing Revolution*, Frontiers of Science (Perseus Books, Reading, MA, 1998).

14. N. Gisin *et al.*, Rev. Mod. Phys. **74**, 145 (2002); S. Ya. Kilin, Usp. Fiz. Nauk **42**, 435 (1999).

15. A. Steane, Rep. Prog. Phys. **61**, 117 (1998).

16. D. Aharonov, in *Annual Reviews of Computational Physics. VI*, edited by D. Stauffer (World Scientific, Singapore, 1999), pp. 259–346.

17. A. Galindo and M. A. Martin-Delgado, Rev. Mod. Phys. **74**, 347 (2002).

18. D. P. DiVincenzo, Science **270**, 255 (1995).

19. A. K. Ekert and R. Jozsa, Rev. Mod. Phys. **68**, 733 (1996).

20. J. Preskill, Course information for Physics 219/Computer Science 219 available at http://theory.caltech.edu/~preskill/ph229 (California Institute of Technology, Pasadena, CA, 2000).

21. A. Y. Kitaev, Russ. Math. Surv. **52**, 1191 (1997).

22. The Center for Quantum Computation (Oxford) (http://www.qubit.org).

23. The International Conference on Quantum Information (ICQI) and the Eighth Rochester Conference on Coherence and Quantum Optics (CQO8) Rochester, NY, 10–16 June 2001; see http://www.optics.rochester.edu/~stroud/conference.

24. G. Giedke, "What is Quantum Information Processing?," available at www.magiqtech.com/products/whatisqip.php.

25. P. L. Knight and R. W. Boyd, eds., J. Mod. Opt. (Special Issue: Quantum Communication) **41** (12) (1994); G. Rarity, P. R. Tapster, and P. M. Gorman, eds., J. Mod. Opt. (Special Issue: Technologies for Quantum Communications) **48** (13) (2001); P. G. Kwiat, ed., New J. Phys. (Focus on Quantum Cryptography) **4** (2002).

26. S. Braunstein and H.-K. Lo, eds., Fortschr. Phys. (Special Focus Issue: Experimental Proposals for Quantum Computation) **48** (9–11) (2000).

27. I. Chuang, Nature **420**, 25 (2002); Quantum Information and Computation **1** (1) (2001).

28. C. H. Bennett, Phys. Today **48**, 24 (1995).

29. I. Walmsley and P. Knight, Opt. Photonics News, November 2002, 42.

30. W. P. Risk and D. S. Bethune, Opt. Photonics News, July 2002, 26.

31. A. Zeilinger, Phys. World **11**, 35 (1998).

32. M. A. Nielsen, Sci. Am. **287**, 67 (2002).

33. See http://www.sciam.com for Scientific American articles related to quantum information science.

34. J. A. Wheeler and W. H. Zurek, eds. *Quantum Theory and Measurement*, Princeton Series in Physics (Princeton University Press, Princeton, NJ, 1983).

35. P. Jonsson, "Generation, Detection and Applications of Single Photons," Ph.D. thesis, Royal Institute of Technology, 2002; "Solid State Sources for Single Photons (S4P)," available at http://www.iota.u-psud.fr/~S4P/.

36. D. F. Walls and G. J. Milburn, *Quantum Optics* (Springer-Verlag, Berlin, 1995), p. 42.

37. L. Davidovich, Rev. Mod. Phys. **68**, 127 (1996).

38. U. Mets, in *Fluorescence Correlation Spectroscopy: Theory and Applications*, edited by R. Rigler and E. Elson, Springer Series in Chemical Physics, Vol. 65 (Springer, Berlin, 2001), pp. 346–359.

39. R. J. Hughes, G. L. Morgan, and C. G. Peterson, J. Mod. Opt. **47**, 533 (2000); R. J. Hughes *et al.*, New J. Phys. **4**, 43 (2002); J. G. Rarity *et al.*, New J. Phys. **4**, 82 (2002).

40. D. Stucki *et al.*, New J. Phys. **4**, 41 (2002); E. Klarreich, Nature **418**, 270 (2002).

41. A. V. Sergienko *et al.*, Phys. Rev. A **60**, R2622 (1999); B. C. Jacobs and J. D. Franson, Opt. Lett. **21**, 1854 (1996).

42. E. Knill, R. Laflamme, and G. J. Milburn, Nature **409**, 46 (2001); E. Knill, R. Laflamme, and G. Milburn, "Efficient Linear Optics Quantum Computation" (2000), available at http://arXiv.org/abs/quant-ph/0006088.

43. J. Calsamiglia, "Quantum Information Processing and Its Linear Optical Implementation," Ph.D. thesis, University of Helsinki, 2001.

44. Q. A. Turchette *et al.*, Phys. Rev. Lett. **75**, 4710 (1995).

45. C. K. Law, J. Mod. Opt. **44**, 2067 (1997).

46. N. J. Cerf, C. Adami, and P. G. Kwiat, Phys. Rev. A **57**, R1477 (1998).

47. J. C. Howell and J. A. Yeazell, Phys. Rev. Lett. **75**, 198 (2000).

48. *Ibid.*, Phys. Rev. A **61**, 052303 (2000).

49. *Ibid.*, 012304 (2000).

50. T. B. Pittman, B. C. Jacobs, and J. D. Franson, Phys. Rev. Lett. **88**, 257902 (2002).

51. *Ibid.*, Phys. Rev. A **64**, 062311 (2001).

52. A. Shields, Science **297**, 1821 (2002).

53. S. Benjamin, Science **290**, 2273 (2000).

54. H. J. Kimble, M. Dagenais, and L. Mandel, Phys. Rev. Lett. **39**, 691 (1977).

55. C. K. Hong and L. Mandel, Phys. Rev. Lett. **56**, 58 (1986).

56. F. Diedrich and H. Walther, Phys. Rev. Lett. **58**, 203 (1987).

57. P. Grangier, G. Roger, and A. Aspect, Europhys. Lett. **1**, 173 (1986).

58. W. P. Ambrose *et al.*, Chem. Phys. Lett. **269**, 365 (1997).

59. C. Kurtsiefer *et al.*, Phys. Rev. Lett. **85**, 290 (2000).

60. R. Brouri *et al.*, Opt. Lett. **25**, 1294 (2000).

61. S. Mayer, "N/V-Zentren als Einzel-Photonen-Quelle," Ph.D. thesis, Ludwig-Maximilians-Universität München, 2000.

62. L. Fleury *et al.*, Phys. Rev. Lett. **84**, 1148 (2000).

63. F. Treussart *et al.*, Opt. Lett. **26**, 1504 (2001).

64. F. De Martini, G. Di Giuseppe, and M. Marrocco, Phys. Rev. Lett. **76**, 900 (1996).

65. J. Kim *et al.*, Nature **397**, 500 (1999).

66. A. Imamoglu and Y. Yamamoto, Phys. Rev. Lett. **72**, 210 (1994).

67. E. Moreau *et al.*, Appl. Phys. Lett. **79**, 2865 (2001).

68. P. Michler *et al.*, Science **290**, 2282 (2000).

69. C. Santori *et al.*, Phys. Rev. Lett. **86**, 1502 (2001).

70. J. Hecht, Laser Focus World **38**, 20 (2002).

71. Z. Yuan *et al.*, Science **295**, 102 (2001).

72. C. Brunel *et al.*, Phys. Rev. Lett. **83**, 2722 (1999).

73. B. Lounis and W. E. Moerner, Nature **407**, 491 (2000).

74. F. Treussart *et al.*, Phys. Rev. Lett. **89**, 093601 (2002).

75. A. Beveratos *et al.*, Eur. Phys. J. D **18**, 191 (2002).

76. A. Beveratos *et al.*, Phys. Rev. Lett. **89**, 187901 (2002).

77. P. Michler *et al.*, Nature **406**, 968 (2000).

78. B. Lounis *et al.*, Chem. Phys. Lett. **329**, 399 (2000).

79. G. Messin *et al.*, Opt. Lett. **26**, 1891 (2001).

80. T. Basché *et al.*, eds. *Single-Molecule Optical Detection, Imaging and Spectroscopy* (VCH Publishers, Weinheim, 1997).

81. W. E. Moerner and M. Orrit, Science **283**, 1670 (1999).

82. W. E. Moerner, Science **277**, 1059 (1997).

83. T. Basché *et al.*, Phys. Rev. Lett. **69**, 1516 (1992).

84. L. Fleury *et al.*, Mol. Phys. **95**, 1333 (1998).

85. F. Kulzer *et al.*, Chem. Phys. **247**, 23 (1999).

86. S. Chandrasekhar, *Liquid Crystals*, Cambridge Monographs on Physics (Cambridge University Press, Cambridge, England, 1977).

87. E. Yablonovitch, Phys. Rev. Lett. **58**, 2059 (1987).

88. S. John, Phys. Rev. Lett. **58**, 2486 (1987).

89. E. Yablonovitch, J. Opt. Soc. Am. B **10**, 283 (1993).

90. P. R. Villeneuve and M. Piché, Prog. Quantum Electron. **18**, 153 (1994).

91. G. Kurizki and J. W. Haus, eds., J. Mod. Opt. (Special Issue: Photonic Band Structures) **41** (2) (1994).

92. S.-H. Chen, D. Katsis, A. W. Schmid, J. C. Mastrangelo, T. Tsutsui, and T. N. Blanton, Nature **397**, 506 (1999).

93. D. Katsis, A. W. Schmid, and S.-H. Chen, Liq. Cryst. **26**, 181 (1999).

94. T. J. Bunning and F. H. Kreuzer, Trends Polym. Sci. **3**, 318 (1995).

95. V. I. Kopp *et al.*, Opt. Lett. **23**, 1707 (1998).

96. I. P. Il'chishin *et al.*, JETP Lett. **32**, 24 (1980).

97. B. Taheri *et al.*, Mol. Cryst. Liq. Cryst. **358**, 73 (2001).

98. H. Finkelmann *et al.*, Adv. Mater. **13**, 1069 (2001).

99. O. D. Lavrentovich and M. Kleman, in *Chirality in Liquid Crystals*, edited by H.-S. Kitzerow and C. Bahr, Partially Ordered Systems (Springer, New York, 2001), pp. 115–158.

100. L. Ramos *et al.*, Phys. Rev. E **66**, 031711 (2002).

101. Y. Geng, A. Trajkovska, D. Katsis, J. J. Ou, S. W. Culligan, and S. H. Chen, J. Am. Chem. Soc. **124**, 8337 (2002).

102. R. Hanbury Brown and R. Q. Twiss, Nature **177**, 27 (1956).

103. A. Molski, Chem. Phys. Lett. **324**, 301 (2000).

EXAFS Measurements of Laser-Generated Shocks with an Imploded Target as a Radiation Source

Introduction

Recently, great interest has been shown in the study of dynamic material response to shocks of high pressure and high strain rate.[1,2] Shocks of up to ~1 Mbar and strain rates of ~10^7 to 10^8 s^{-1} were generated in metals (Al, Cu) by laser irradiation. The laser intensity in those experiments (~10^{11} W/cm^2) was high enough to raise the pressure above the Hugoniot elastic limit (HEL) but low enough for the compressed material to remain solid. Using Bragg and Laue x-ray diffraction, the experiments clearly showed the retention of crystallinity during the passage of the shock. Silicon under these conditions was found to compress elastically, i.e., only in the direction of shock compression. Copper, on the other hand, was found to compress equally in all dimensions, indicating the transition to plastic flow. These differences were explained in terms of the different velocity of dislocation propagation that gives rise to the elastic–plastic transition.

The goal of this work is to examine the use of EXAFS[3] (extended x-ray absorption fine structure) as a complementary characterization of such laser-shocked metals. EXAFS modulations above an absorption edge are due to the interference of the ejected photoelectron wave with the reflected wave from neighboring atoms. Thus, the interference translates into modulations in the cross section for photon absorption above the edge. The frequency of these modulations relates to the inter-particle distance, hence the density of the compressed material. The decay rate of the modulation with increasing photoelectron energy yields the MSRD (mean-square relative displacement) and can thus serve as a temperature diagnostic. EXAFS had originally been applied to crystalline materials but has since been widely used to study amorphous,[4–6] liquid,[7–9] heated,[8,10–17] or compressed[11,14–16,18,19] materials. In those steady-state experiments, the imposed temperature is known independently and the main emphasis is on studying the chemical structure. In this experiment the emphasis is on measuring the compression and temperature of the shocked material through the EXAFS spectrum itself. There is an important difference between the diffraction experiments and the present EXAFS experiment: EXAFS, which depends only on short-range order, does not require the use of single-crystal samples, as was the case in the diffraction experiments. In this experiment we use polycrystalline Ti foils in which the number of crystalline grains under the laser focal spot is very large. Thus, the shock direction is randomly distributed with respect to the atomic planes. It is known that the same stress can cause elastic or plastic deformation in the same crystal, depending on the orientation of the shock direction with respect to the crystal planes.[20] Since the transition to plastic flow depends on the propagation of dislocations along slip planes, we can expect a plastic response in some or most of the crystalline grains. Like in the shock experiments in silicon and copper cited above,[1,2] the shock pressure in our experiments (~0.4 Mbar) is much higher than the Ti HEL.[21] *The assumption of three-dimensional compression, required to relate the EXAFS-determined inter-atomic distance to the density, can be tested by comparison with the measurement of shock speed, which yields the compression (through the known Hugoniot).*

Most EXAFS experiments are performed with a synchrotron radiation source, and the spectrum due to a sample in steady state is slowly scanned. In laser experiments[22–24] the entire spectrum is recorded simultaneously during the short pulse (~ns) of the laser. This makes it challenging to obtain an EXAFS spectrum of high signal-to-noise ratio. In a previous paper[25] we have shown that a CH shell imploded by a multi-beam laser system constitutes a source of an intense and smooth spectrum of x-ray radiation, suitable for EXAFS measurements. The high source intensity enables us to work with a thick Ti foil (attenuation ~e^{-3} above the K edge), which increases the relative modulations in the observed signal. Using the 60-beam OMEGA laser,[26] the intensity from imploded shells around 5 keV was sufficient to obtain a good EXAFS spectrum above the K edge of Ti at 4.96 keV. Fitting a theoretical model to the measured EXAFS spectrum yielded the inter-particle distance and temperature in agreement with synchrotron results.[27,28] Those absorption experiments were performed on cold, unshocked Ti foils in order to test the reliability of the present method, which is here extended to the shocked case.

Titanium was chosen because of the following considerations: The EXAFS spectrum from a low-Z absorber, because of the high attenuation in our experiment, would be dominated by the second-order crystal diffraction (whose attenuation is much smaller). In Ti the second-order radiation (around ~10 keV) is too weak to affect the results. On the other hand, for a higher-Z absorber the imploding-target emission at the corresponding higher photon energy would be too weak. Titanium behavior is complicated, however, by phase transitions:[29] at normal conditions Ti crystallizes as hexagonal close packed (α-Ti); as the pressure rises, it transforms to a hexagonal phase (ω-Ti) at low temperatures, or to a body-centered cubic (β-Ti) at high temperatures. For shocked titanium a transition from α-Ti to ω-Ti has been shown[30] to occur at a pressure of ~0.12 Mbar; this value varies with the sample purity but it is clearly much lower than the pressure in this experiment (~0.4 Mbar). Following this transition there may be an additional transition of ω-Ti to β-Ti, but the Hugoniot shows no additional discontinuity up to ~1.2 Mbar[31] and static-pressure studies showed no such transition for pressures as high as 0.87 Mbar.[32] Recently, a new Ti phase (γ) has been discovered[33] but it is reached at a higher pressure (~1.1 Mbar) than relevant to this experiment. We next address the question of the time constant t_0 for the (α-Ti) to (ω-Ti) phase transition. Although previous phase transitions in Ti have been observed with much lower strain-rate shocks, a pressure dependence of t_0 has been determined[34] that can be extrapolated to the pressure (~0.4 Mbar) in this experiment. In the range of 0.05 to 0.09 Mbar, the time constant decreases exponentially with the pressure; extrapolating to $P = 0.4$ Mbar yields $t_0 \ll 1$ ns. The phase transition α-Ti to ω-Ti entails a 1.9% decrease in volume,[33] much smaller than the implied volume change due to the compression. However, the change in crystal structure strongly affects the EXAFS spectrum as the geometry of the nearest neighbors is now more complex.[35]

The theory of EXAFS[3] yields an expression for the normalized modulations $\chi(k) = \mu(k)/\mu_0(k) - 1$, where $\mu(k)$ is the absorption coefficient (or opacity) and $\mu_0(k)$ is the absorption of the isolated atom (i.e., without the EXAFS oscillations). $\mu_0(k)$ can be obtained by passing a smooth curve through the EXAFS oscillations. k is the wave number of the ejected photoelectron and is given by the de Broglie relation $\hbar^2 k^2/2m = E - E_K$, where E is the absorbed photon energy and E_K is the energy of the K edge. For low disorders and polycrystalline materials, the basic EXAFS theory,[3] assuming single-electron scattering and plane electron waves and neglecting multiple scattering, yields the following expression for the normalized modulations $\chi(k)$:

$$\chi(k) = \sum_j N_j S_0^2 F_j(k) \exp\left[-2\sigma^2 k^2 - 2R_j / \lambda(k)\right]$$

$$\times \sin\left[2kR_j + \phi_j(k)\right] / kR_j^2, \qquad (1)$$

where N_j is the number of atoms surrounding the absorbing atom at a distance R ($N_1 = 12$ in Ti). The sum over j relates to successive shells of atoms around the photo-absorbing atom. Only the first coordination shell will be of interest here because it suffices for determining the density; also, in the shocked material the contribution of higher shells essentially disappears. R is the interparticle distance, and the factor σ^2 (Debye–Waller factor) accounts for thermal vibrations, derived from a harmonic potential. σ^2 can also include static disorder $\left(\sigma_{\text{total}}^2 = \sigma_{\text{vibration}}^2 + \sigma_{\text{disorder}}^2\right)$, corresponding to a Gaussian distribution of pair distances. The backscattering amplitude $F(k)$ and phase-shift factor $\phi(k)$ for titanium were calculated by Teo and Lee.[36] McKale et al.[37] have improved these calculations by removing the assumption of photoelectron plane waves; their results differ from those of Teo and Lee, primarily for $k \le 3$. We have averaged the results of McKale et al. for scandium and vanadium (their calculations apply to every other element) and have made a minor adjustment to fit the Ti results of Teo and Lee at high wave numbers. The mean free path of the ejected electron for inelastic collisions in titanium, $\lambda(k)$, was taken from Blanche et al.[27] The vibration amplitude σ^2 and the interatomic distance R are treated as adjustable parameters in fitting Eq. (1) to the experimental EXAFS spectrum. In addition, the adjustable constant $S_0^2 (< 1)$ accounts for multi-electron effects such as relaxation of the core hole and excitation of other than the ejected photoelectron.[3] Finally, an adjustable energy shift ΔE is applied to the experimental points to account for uncertainties in chemical-bonding and core-relaxation effects. The edge energy ($k = 0$) is initially determined by the inflection point, i.e., the energy for which the derivative of the falling intensity above the edge is maximal. The distance R can yield the density of the absorber. The temperature can be found from the σ^2 value, which depends also on the density. Beni and Platzman[38] have calculated σ^2 as a function of temperature using the Debye model for the phonon density of states, including correlation between the motions of the central and neighboring atoms. We use the first term in their result (including a factor-of-2 correction[10]), neglecting the correlation term. Greegor and Lytle[10] have compared the results of Beni and Platzman[38] to their measurements (in copper) and have shown that neglecting the correlation term increases σ^2 by about 20%. We therefore reduced the uncorrelated results for Ti by 20%. As a check, we compared

the measured values[7] of σ^2 for Zn in the temperature range of 0.01 to 0.06 eV with those calculated by the procedure described here, and they agree to within a few percent. σ^2 depends on the density through the Debye temperature. Using an empirical model[39] we calculate the density dependence of the Debye temperature (in eV) as

$$\Theta_B = -14.79 + 50.39\left(\rho/\rho_s\right) + \left(\rho/\rho_s\right)^2, \qquad (2)$$

where ρ is the density and ρ_s is the solid density. We show in Fig. 94.38 the calculated σ^2 for Ti as a function of temperature and density. As seen, compression increases the amplitude of the EXAFS signal because of the decrease in σ^2. This is in addition to the increase because of the explicit $1/R^2$ dependence in Eq. (1). On the other hand, compression reduces the EXAFS signal because $\lambda(k)$ in Eq. (1) depends on the density ρ as $1/\rho$.
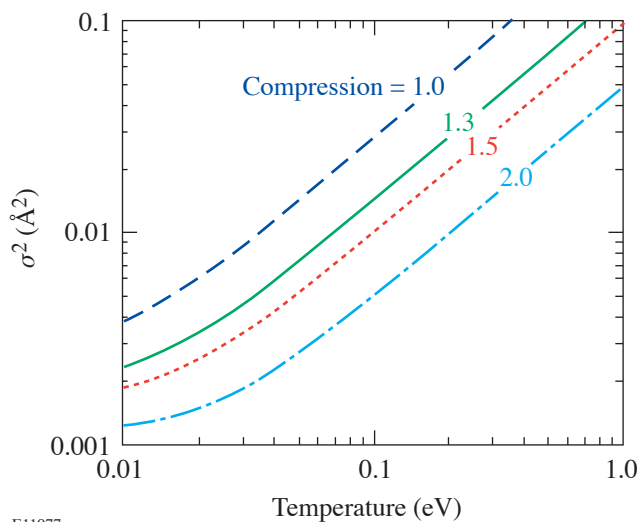
E11977

Figure 94.38
Calculated σ^2 due to thermal vibrations for Ti from the model of Beni and Platzman[38] making use of the density dependence of the Debye temperature from Ref. 39. Correlation was accounted for by reducing the first, uncorrelated term in Ref. 38 by 20%.

Although advanced EXAFS models have been developed,[40–42] the use of Eq. (1) is adequate for our experiments: curved-wave effects are included in the calculations[37] of phase shift and backscattering amplitude, multi-electron effects are accounted for by the S_0^2 factor, and multiple scattering is negligible for the first coordination shell,[43] the only one of interest here.

Experiment

Figure 94.39 shows a schematic view of the target used to measure EXAFS spectrum in laser-shocked targets. Fifty-seven beams of the OMEGA laser, of ~21-kJ total energy, are focused on an empty CH shell whose implosion generates the radiation source for measuring the absorption spectrum in Ti. The three remaining OMEGA beams are stacked and used to irradiate and launch a shock wave in Ti. The laser pulse shape was 1 ns square; thus the three stacked beams formed a 3-ns-long square pulse; these beams were focused onto the plane target in a 3.8-mm-diam focal spot, giving an irradiance of 0.5 TW/cm^2. A delay time for the three stacked beams with respect to the rest of the beams was adjusted so that peak implosion of the spherical target occurred when the shock had just traversed the Ti layer. The spherical target had a diameter ~940 μm and a thickness ~20 μm. The planar target consisted of 10-μm-thick polycrystalline Ti, coated on both sides with 17 μm of CH. The purpose of the front CH layer was to prevent laser heating and ablation of the Ti. The purpose of the back CH layer was to prevent the shock unloading at the back Ti surface. The thickness of the Ti layer d was the highest ($\mu_0 d \sim 3$) that still yielded significant x-ray signal after K-edge absorption. A thicker absorber yields higher EXAFS modulations in the observed intensity I since $(\Delta I/I) \sim (\mu_0 d)(\Delta\mu_0/\mu_0)$. From the point of view of signal-to-noise (S/N) ratio, the optimal value of $\mu_0 d$ depends on the source of noise: for photon noise ($\sim I^{1/2}$) it can be shown to be 2. When the noise is proportional to I, the S/N ratio continuously increases with $\mu_0 d$. We found the latter to be the case here. The CH thickness and laser pulse length were chosen to minimize nonuniformity in the Ti properties in the direction of the shock (see Fig. 94.43 later in article).

The heat shield (0.5-mm-thick CH foil) minimizes the heating of the Ti layer due to radiation from the imploding spherical target. It attenuates the EXAFS-producing radiation at ~5 keV by a factor of ~2.5 while very strongly attenuating the softer radiation, which can heat the Ti foil. The functioning of the heat shield was tested (see below) by measuring the EXAFS spectrum when the three shock-launching beams were not fired.

Two x-ray spectrometers measured the spectrum on calibrated film.[44] One x-ray spectrometer (XRS-I) measured the EXAFS spectrum, the other (XRS-II) the incident spectrum I_0. A typical I_0 spectrum is shown in Fig. 2(a) of Ref. 25. To cross-calibrate the two spectrometers, a 10-μm-thick Ti foil was placed on some shots in front of XRS-II, and its EXAFS spectrum was compared with that obtained in XRS-I without launching a shock. The spectral resolution of the spectrometer

is limited by the source size. The FWHM size of the core seen at 5 keV (Fig. 1 in Ref. 25) is $D \sim 100$ μm; this translates to a spectral resolution $\Delta E = ED/tg(\Theta_B)L$, where L is the distance from the target to the film and Θ_B is the Bragg angle. This yields a resolution of ~5 eV, much smaller than a typical EXAFS modulation period (~60 eV).

Although the EXAFS measurement is time integrated, a meaningful shock diagnosis can be obtained without streaking the spectrum in time because the x-ray pulse width is very short. We previously showed[25] that the emission from the spherical target above the Ti K edge (~5 keV) comes mostly from the compressed core, whereas the emission from the laser-absorption region is much weaker. This was seen in both the time-resolved spectrum as well as the space-resolved spectrum. The former showed that the pulse width of the x-ray emission at ~5 keV was only ~120 ps [Fig. 2(b) in Ref. 25], much shorter than the shock transit time through the Ti (~2 ns).

The implosion of the spherical target has to be timed so as to probe the Ti layer after it is traversed by the shock. This is because the EXAFS spectrum of a partly shocked foil is dominated by the low-temperature region ahead of the shock front. The delay of the shock-launching beam with respect to the implosion beams is given by the difference τ(implosion) $- \tau$ (Ti), where t (implosion) is the compression time of the spherical target and τ (Ti) is the shock arrival time at the back of the Ti layer. Both these times have been measured; they are also known from simulations by the hydrodynamic code *LASNEX*.[45] The implosion time is determined by streaking the soft-x-ray emission from the spherical target. Since the emission above the Ti K edge (~5 keV) is completely dominated by the compressed core, in order to see the coronal emission during the rising part of the laser, we streak the spectrum at the softer energy of ~3 keV (see Fig. 94.40), where the compressed-core emission is completely saturated. The indicated compression time is ~1.7 ns.

The time τ(Ti) is determined experimentally by the method of active shock breakout (ASBO).[46] Figure 94.41 shows the corresponding experimental configuration and a sample result. An EXAFS target (Fig. 94.39) was irradiated at the same intensity as in the EXAFS experiment. A frequency-tripled YAG laser, synchronized with OMEGA, irradiated the backside of the target and interfered with the reflected beam. Figure 94.41 shows the interference fringes measured by a streak camera, viewing the central portion of the focal spot. Also shown is a series of simultaneously recorded fiducial time pulses marking the time scale; the time $t = 0$ corresponds to the start of the laser pulse. Initially, the laser is reflected from the backside of the Ti foil. When the shock reaches this surface [at time τ (Ti)], the reflection is seen to be disrupted. This is the
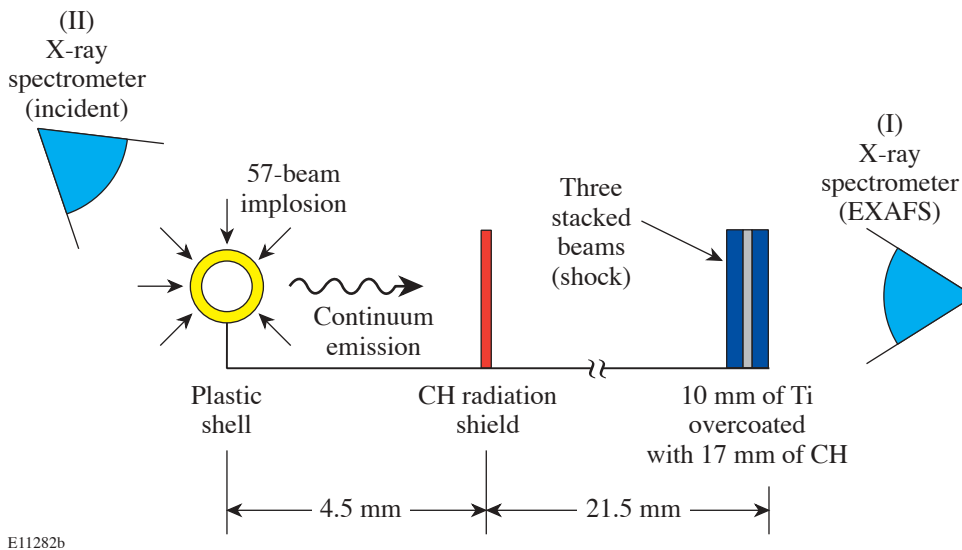

E11282b

Figure 94.39
Schematic view of the target. The imploding spherical target serves as a radiation source for EXAFS measurements. X-ray spectrometer I measures the EXAFS spectrum; x-ray spectrometer II measures the incident spectrum I_0. The heat shield minimizes the heating of the shocked Ti layer due to radiation from the imploding spherical target.

optimal time for EXAFS probing. Subsequent to this, a weaker reflection from the backside of the CH layer is seen; when the shock reaches that surface, at time τ(CH), ablation sets in, the laser is strongly absorbed, and reflection disappears. It is not mandatory to know τ(Ti) with great precision in setting the

delay between the shock-launching beam and the backlighter beams. This is because we repeat the experiment for different time delays around the expected optimal value; when the shock arrives at the back surface of the Ti layer, the EXAFS spectrum clearly changes into a lower-intensity, faster-decaying spectrum.
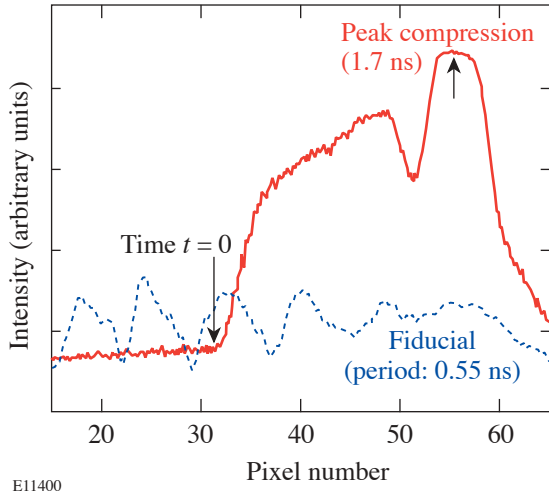
The ASBO data can also be used to determine the shock velocity, i.e., the shock strength. Since the time τ(Ti) includes the time of shock travel through the front CH layer, we can use the difference τ(CH) − τ(Ti) to find the net transit time through the Ti layer. For that we assume that the travel time through the two CH layers is the same. This was verified by code simulations to be correct to within a few percent. For an irradiance of 0.5 TW/cm^2 (the case analyzed by EXAFS below) the shock velocity in the Ti layer was found to be ~6.3 km/s, which, according to the Ti Hugoniot,[31,47] corresponds to a pressure of 0.4 Mbar and compression of 1.28. *An agreement of the density as measured by EXAFS and the density derived from the shock speed through the Hugoniot (as is the case below) is a confirmation of the assumption of 3-D compression.*

Finally, the ASBO data show the velocity nonuniformity across the shock front to be ±10%, which, according to the Hugoniot of Ti, translates into a nonuniformity of ±4% in the pressure as well as in the density. *LASNEX* runs show that the

E11400

Figure 94.40
Streaked x-ray spectral intensity around ~3 keV emitted by the imploding spherical shell. The streak is used to determine the implosion time, which is required for determining the EXAFS probing time.

E11860a
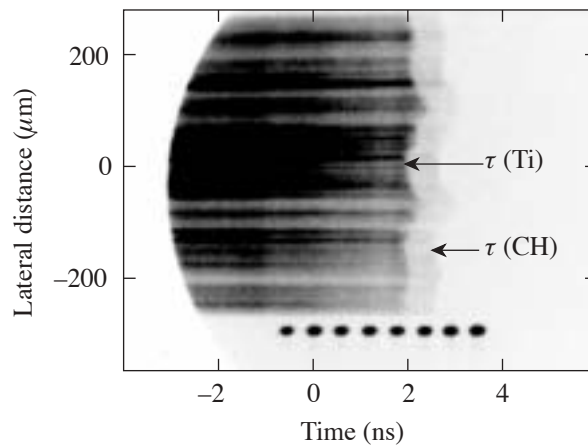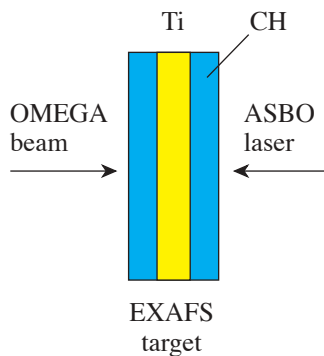
Figure 94.41
Active shock breakout (ASBO) measurement of the arrival time τ(Ti) of the laser-launched shock at the back surface of the Ti layer. Time $t = 0$ corresponds to the start of the laser pulse. This measurement is also used to assess the shock nonuniformity and to confirm (through the Hugoniot) the EXAFS-measured compression.

average density variation during the probing time interval (~120 ps) is less than 2%, as is the density variation along the shock direction (Fig. 94.43). These uncertainties are much smaller than the change in density due to the compression, as shown below.

Hydrodynamic Simulations

To determine the expected shock strength and the properties of the shocked Ti for a given laser irradiation, the hydrodynamic code *LASNEX* was used for one-dimensional simulations. It includes the "quotidian" equation of state[39] (QEOS), based on the Thomas–Fermi equation of state with empirical corrections. As an indication of its validity at low temperatures we compare in Fig. 94.42 curves of QEOS pressures at constant Ti compression with experimental points[33] obtained recently for Ti in a diamond anvil cell at room temperature and the same compressions. The agreement is quite good; however, the curves also show the low sensitivity to the temperature, which reduces the precision in the temperature prediction.
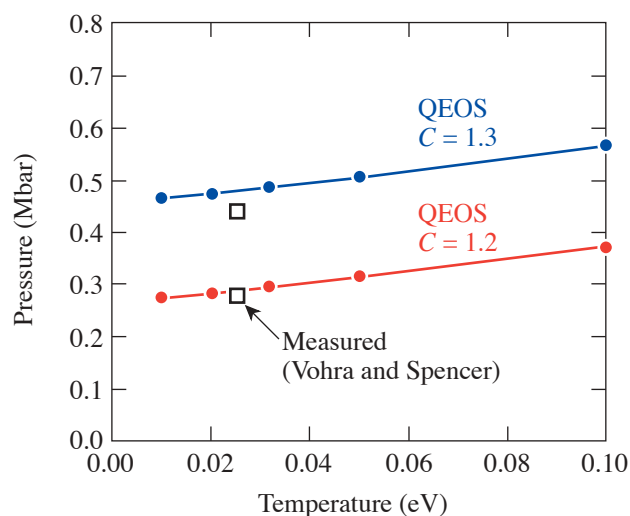
Figure 94.42
QEOS curves for two compression values in Ti. Experimental values obtained in a diamond anvil cell at room temperature for the same compression values are also shown.[33]

The *LASNEX*-calculated profiles of density, pressure, and temperature for a laser irradiance of 0.5 TW/cm^2 are shown in Fig. 94.43 at the time of arrival of the shock at the rear surface of the Ti layer, namely 3.5 ns. These simulations correspond to the experimental results discussed below. The profiles, particularly that of the density, are seen to be quite uniform throughout the Ti. The average value of density within the Ti (~5.6 g/cm^2) and the average value of pressure (~0.4 Mbar) are

consistent with the measured[31,47] Hugoniot of Ti. As will be shown in the next section, the measured EXAFS spectrum at about the time 3.5 ns yields a compression of 1.3 (assuming three-dimensional compression), as compared with a compression of 1.25 in these simulations. Code runs with an initial temperature higher than room temperature showed that the temperature due to radiation preheat can simply be added to the calculated temperature profiles.
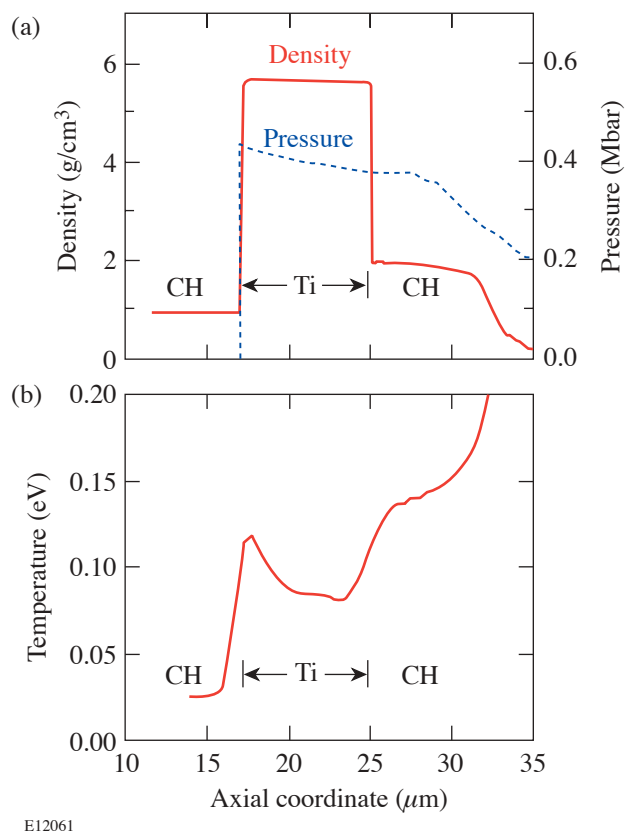
Figure 94.43
LASNEX-calculated profiles of (a) density and pressure and (b) temperature for a laser irradiance of 0.5 TW/cm^2 at the time of arrival of the shock at the back surface of the Ti layer, namely 3.5 ns. The laser is incident from the right.

Results and Analysis

1. Radiation Heating

The extraction of the experimental $\chi(k)$ to be compared with Eq. (1) follows the standard procedure.[3] First, the absorption coefficient $\mu = \log(I_0/I)$ is computed from the measured intensities. As explained before, no correction for the finite spectral resolution (~5 eV) was required. Likewise, higher-harmonic contribution to the crystal diffraction could be ignored: the spectrum emitted by the implosion had a characteristic temperature ~1 keV; thus the second-order radiation at 10 keV

was weaker than the first order by a factor of $\sim e^5$, in addition to its lower crystal reflectivity. The normalized EXAFS spectrum $\chi(k)$ was calculated using the McMaster adjustment:[48]

$$\chi(k) = \left\{[\mu(k) - \mu_0(k)]/\Delta\mu\right\}\left[\Delta\mu^{th}(k=0)/\Delta\mu^{th}(k)\right], \quad (3)$$

where $\Delta\mu$ is the measured jump at the K edge and $\Delta\mu^{th}(k)$ is the theoretical net K-shell absorption.

To study the effect of shocks on the Ti metal, the effect of radiation heating should be minimal. This was verified by measuring the EXAFS spectrum with the target of Fig. 94.39 but without launching a shock. Figure 94.44 shows the measured normalized EXAFS spectrum $\chi(k)$ for such a shot. Next, the $\chi(k)$ due to the first coordination shell is extracted as explained in Ref. 25: $k\chi(k)$ is Fourier transformed to the real space and the first peak is filtered and transformed back to the k space. We use $k\chi(k)$ to de-emphasize the low-k region, where the theory is imprecise. We next fit Eq. (1) to the filtered spectrum while varying R, σ^2, S_0^2, and ΔE_0. Figure 94.45 shows the best fit. Before performing the fit, the theoretical profile was subjected to the same Fourier filtering as the experimental spectrum (in particular, using the same k range); this increases the quality of the fit. The best fit was obtained with $R = 2.93$ Å, $\sigma^2 = 0.011$ Å^2, $S_0^2 = 0.86$, and $\Delta E = 13$ eV. The value of σ^2 corresponds according to Fig. 94.38 to $T = 40$ meV. Thus the radiation heating above room temperature amounts to only ~ 15 meV. As shown below, this is much
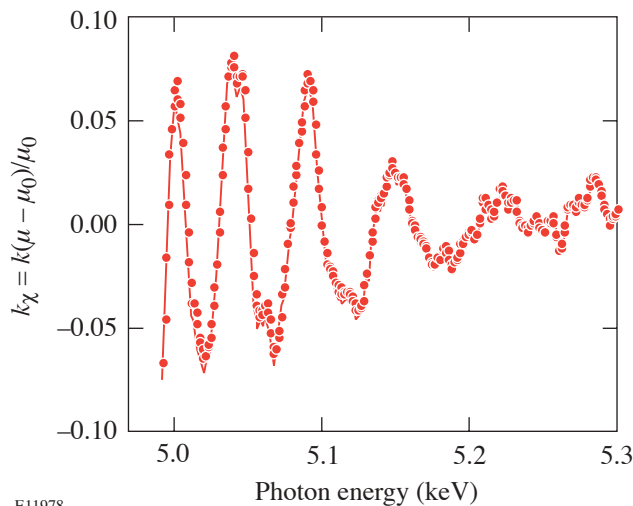
E11980
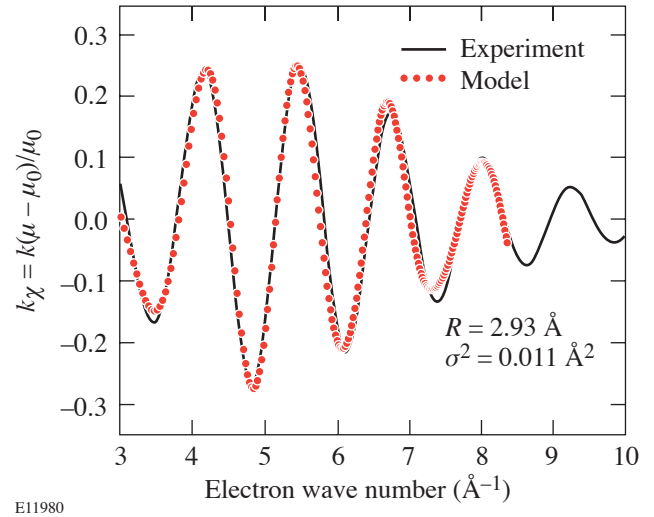
Figure 94.45
Fitting of the model [Eq. (1)] to the observed $k\chi(k)$ EXAFS spectrum from Fig. 94.42. The parameter values (R and σ^2) giving the best fit are shown. The value of R agrees with the known value for Ti at normal conditions. σ^2 corresponds to a temperature of ~ 40 meV.

smaller than the shock heating. Since the incident x-ray intensity in successive shots is not entirely reproducible, we normalize the heating in each shot by the corresponding intensity of x-ray emission at 5 keV. The explanation of the fitting and the calculation of the error bars are explained in the Appendix.

2. Shock Compression

Shock-compression experiments using the 3-ns, 0.5-TW/cm^2 laser irradiation have been performed by varying the shock probing time, given by the delay between the shock-launching beams and the compression beams. The appropriate shock probing time for a 3-ns laser pulse, an irradiation of 0.5 TW/cm^2, and the target described above was found to be ~ 3.5 ns, both through ASBO measurements and *LASNEX* code simulations. In successive shots we probed the shocked Ti both before and after that time. At around a probing time of ~ 3.5 ns the EXAFS clearly changed to a faster-decaying spectrum: the number of clearly visible modulations dropped from ~ 6 to ~ 3. The results at a probing time ~ 3.5 ns indeed show a compression of the Ti layer. To illustrate the compression directly we compare in Fig. 94.46 the measured absorption spectra (before Fourier filtering) for two probing times: before the shock enters the Ti layer (marked "before shock arrival") and when the shock has just traversed the Ti layer (marked "after shock arrival"). The lengthening of the EXAFS period of modulation in the after-shock case is evidence of compression. The two shots were identical except for the different delay time. The

E11978

Figure 94.44
Normalized EXAFS spectrum $\chi(k)$ before Fourier filtering for an unshocked shot, used to determine the temperature rise due to radiation heating.

curve marked before shock is shifted by 5 eV toward higher wave numbers for a clearer demonstration of the lengthening. The effect of the shock is also seen in increasing the damping rate of the modulations. Figure 94.47 shows the fitting of Eq. (1) to the Fourier-filtered experimental spectrum. The value of R for the best fit is (2.68 ± 0.05) Å, which is smaller by a factor of ~1.1 than the value $R = 2.92$ Å for an unperturbed Ti. The difference between the two values is much larger than the uncertainty in R. Assuming the compression is three-dimensional, this corresponds to a volume compression by a factor of ~1.3 or a density of 5.8 g/cm^3. This agrees with the compression value derived above from the measured shock velocity (1.28) as well as with the average compression (1.25) of the profile calculated by *LASNEX* (Fig. 94.43). This agreement supports the assumption of three-dimensionality, which was also postulated above, based on the fact that a polycrystalline Ti sample was used in this experiment.

The value of σ^2 (namely, 0.033) is much higher than in the unshocked case (Fig. 94.45). According to Fig. 94.38, this value would correspond to a temperature of ~0.24 eV, much higher than the value ~0.09 predicted by *LASNEX* (Fig. 94.43). We conclude that σ^2 has a contribution from static disorder in addition to thermal vibrations, due possibly to the α-Ti to

ω-Ti phase transformation. A large σ^2 value has also been found in EXAFS measurements applied to various disordered systems.[5,6,15,17] In particular, it has been shown[15] that a Ge crystal transformation from diamond type to white-tin type at 0.11 Mbar is accompanied by a quadrupling in the value of σ^2. Similarly, a doubling in the value of σ^2 was found[17] to accompany the order–disorder transition in CuI; finally, we cite measurements[16] on compressed Ga close to room temperature where, because of phase transformation, values of σ^2 comparable to the result of Fig. 94.47 have been measured. It should be emphasized that the increase in σ^2 cannot be due to melting. First, the melting temperature of Ti at normal conditions is ~0.17 eV, but at a compression of 1.3 it rises to ~0.3 eV as calculated by the Lindemann law,[49] thus certainly higher than the temperature in the shocked Ti. Moreover, experiments have shown that melting does not cause an increase in σ^2 beyond that associated with the increase in temperature.[9]

In the initial α-Ti crystal each atom is surrounded by 12 atoms at a distance of 2.92 Å. In the more-complex ω-Ti geometry[35] the arrangement of neighboring atoms is of two kinds, described as site A and site B. For every atom in site A there are two atoms in site B. Site-A atoms have 14 nearest neighbors at a distance of 2.92 Å. Site-B atoms have three
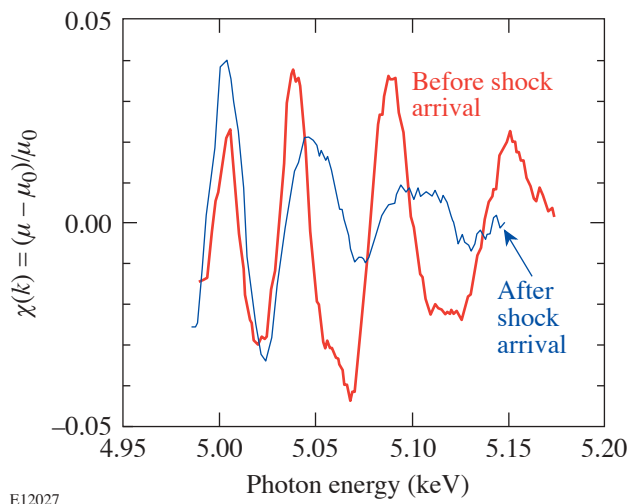
Figure 94.46
Demonstration of shock compression based on the lengthening of the EXAFS period of modulation. The two normalized EXAFS spectra (shown before Fourier filtering) correspond to different probing times from otherwise identical shots. The curve marked "after shock arrival" corresponds to the time when the shock has just traversed the Ti layer. The curve marked "before shock arrival" corresponds to a time before the shock entered the Ti layer.
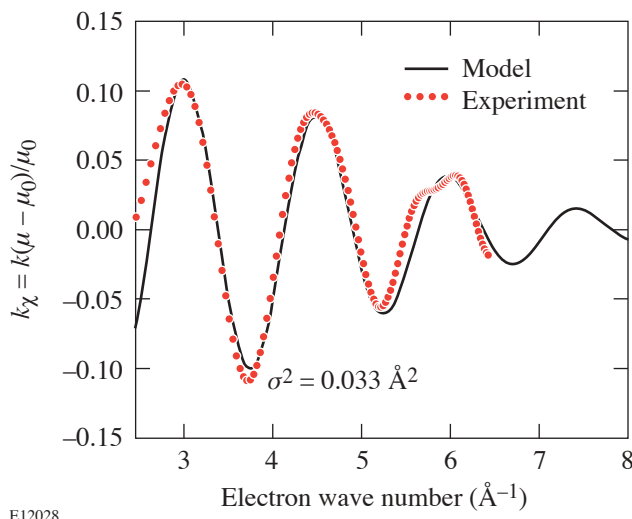
Figure 94.47
Fitting of the model [Eq. (1)] to the observed $k\chi(k)$ EXAFS spectrum (derived from the curve labeled "after shock arrival" in Fig. 94.44, after Fourier filtering). The parameter values giving the best fit are shown. The interatomic distance R yields a compression of 1.3 (assuming to be three-dimensional) and the factor $\sigma^2 = \sigma^2_{\text{therm}} + \sigma^2_{\text{stat}}$ contains both the temperature-dependent vibrations term and a static disorder term.

neighbors at a distance of 2.667 Å, six neighbors at a distance of 2.845 Å, and two atoms at a distance of 3.023 Å. Thus, there is a spread of ~0.3 Å (or ~10%) in the first-shell distances. This has the effect of adding a disorder term to the thermal disorder due to crystal vibration. The different distances translate to EXAFS modulation of different frequencies. The beating of these frequencies when calculating the total EXAFS spectrum gives rise to a decreasing amplitude. Thus, EXAFS spectra can be used to study *dynamic* α-Ti to ω-Ti phase transformation in shock compression. On the other hand, to reliably extract the temperature value from the EXAFS spectrum, a metal that does not undergo a phase transformation should be used. For example, in vanadium no phase transformation has been found up to pressures of 1 Mbar.[29] A smaller σ^2 value in a comparable shocked vanadium experiment would support the conclusion that a phase transformation in the titanium experiment has actually taken place.

To assess the observability of EXAFS in future titanium experiments we plot in Fig. 94.48 the contours of $\max(|\chi|)$ in the compression–temperature space. We divide the contour-value scale into three regions: (a) $\max(|\chi|) > 0.05$, termed high; (b) $0.03 < \max(|\chi|) < 0.05$, termed marginal; and (c) $\max(|\chi|) < 0.03$, termed low. EXAFS can readily be measured in the first region and only marginally in the second [for solid titanium at room temperature $\max(|\chi|) \sim 0.06$]. To show what part of the compression–temperature space can be ac-

cessed by shocks we superimpose on the contours in Fig. 94.48 the values along the principal Hugoniot of Ti.[31,47] As seen, strong shocks are not readily measurable with EXAFS. On the other hand, isentropic (low-temperature) compressions of metals are much more suitable for EXAFS measurements. Figure 94.48 also shows the calculated isentrope that passes through the Hugoniot point corresponding to the present experiment (Fig. 94.47). It was obtained by using the Cowan model for the density dependence of the Gruneisen (γ) of Ti,[39] normalized to the experimental value (~1.17) at solid density.[30] Obviously, even a near-isentropic compression will be much easier to diagnose with EXAFS than a shock of comparable compression.

Further understanding of high-strain-rate shock compression of metals can be gained in future experiments by (a) performing similar experiments on single-crystal samples and comparing EXAFS and multidirectional diffraction measurements, (b) employing a target material that does not undergo phase transformation below ~1-Mbar pressure (e.g., vanadium[29]), and (c) performing near-isentropic compression experiments where higher densities at lower temperatures can be achieved.
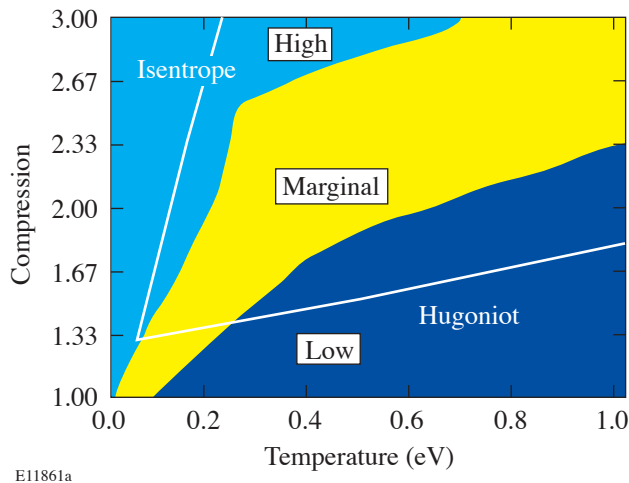
Figure 94.48
Regions of observability of EXAFS in compressed titanium. High: $\max(|\chi|) > 0.05$; marginal: $0.03 < \max(|\chi|) < 0.05$; and low: $\max(|\chi|) < 0.03$. The Hugoniot for Ti[31,46] is shown as well as the isentrope, both passing through the point corresponding to the present experiment.

Appendix A: Fit Optimization and Error Analysis

The fitting of the model [Eq. (1)] to the experimental EXAFS spectrum is achieved by minimizing the X^2 (chi squared) function. To determine the uncertainty in the EXAFS fitting parameters R and σ^2 we use the inverse-Hessian method.[50] We actually vary two other parameters in the fitting, ΔE_0 and the amplitude multiplier S_0^2, but since we are mainly interested in the uncertainty in R and σ^2, we simplify the error calculation to the latter two parameters. The adjustment of S_0^2 and ΔE_0 is done by trial and error, and then the best values of R and σ^2 are determined by minimizing the two-dimensional X^2. We make use of the definition

$$X^2 = \sum_{j=1}^{N} \frac{\left[k\chi(\exp) - k\chi(\text{theory}) \right]^2}{N\delta^2}, \tag{A1}$$

where δ is the mean root square of the noise in the data. The film data are digitized into a 2-D array of pixels s_{ij}. The signal is the average of m rows s_i in the direction of dispersion. As in Fig. 5 of Ref. 25, the noise is obtained by the average over the differences between adjacent pixel rows:

$$\sigma_{\text{noise}} = \sum_{i=1}^{m/2} \left(s_{2i-1} - s_{2i}\right)/m. \qquad \text{(A2)}$$

Here the random components of the measured signals add up, whereas the net signal cancels out. The two-dimensional matrix $X^2(R, \sigma^2)$ is used to find the best values of the parameters R and σ^2 as well as to derive the Hessian matrix $H_{ik} = \delta^2 \chi^2 / \delta a_i \delta a_k$, where $a_1 = R$ and $a_2 = \sigma^2$. The standard deviation in the parameters is obtained from C, the inverse matrix of H: $\Delta R = (C_{11})^{1/2}$ and $\Delta \sigma^2 = (C_{22})^{1/2}$. For the unshocked case (Fig. 94.45) we find $\Delta R = \pm 0.013$ Å or a relative error of ~0.5% and $\Delta \sigma^2 = \pm 0.002$ Å^2 or a relative error of ~20%. This is in line with reported uncertainties in synchrotron experiments. The actual uncertainty in R can be higher because of imprecision in the x-ray wavelength scale, which is ~1%. This is of no concern here, however, because the interest is in shock-induced changes in R, which are of the order of ~10%.

To illustrate the error-calculation results we show in Fig. 94.49 the variation of X^2 with R for the optimal value of σ^2 and with σ^2 for the optimal value of R. The minimum value of X^2 is close to 1, which indicates that the errors in the experimental points are random. The vertical lines show the brackets of uncertainty derived from the two-dimensional Hessian analysis. For shocked-Ti experiments the uncertain-

ties are higher: $R = 2.66 \pm 0.05$ Å or a relative error of ~2% and $\sigma^2 = 0.033 \pm 0.008$ Å^2 or a relative error of ~25%. The poor fit in Fig. 94.47 (mainly in R) indicates the inadequacy of Eq. (1) for the shocked result. Because of the large disorder contribution σ_{stat} (due possibly to a phase transition in Ti), a detailed EXAFS calculation relevant to the crystallographic structure of shocked Ti should be carried out.

REFERENCES

1. D. H. Kalantar *et al.*, Phys. Plasmas **7**, 1999 (2000).

2. L. Loveridge-Smith, A. Allen, J. Belak, T. Boehly, A. Hauer, B. Holian, D. Kalantar, G. Kyrala, R. W. Lee, P. Lomdahl, M. A. Meyers, D. Paisley, S. Pollaine, B. Remington, D. C. Swift, S. Weber, and J. S. Wark, Phys. Rev. Lett. **86**, 2349 (2001).

3. P. A. Lee *et al.*, Rev. Mod. Phys. **53**, 769 (1981).

4. K. Sakurai *et al.*, Appl. Phys. Lett. **57**, 2660 (1990).

5. M. L. Fdez–Gubieda *et al.*, Phys. Rev. B **53**, 620 (1996).

6. M. C. Ridgway *et al.*, Nucl. Instrum. Methods Phys. Res. B **147**, 148 (1999).

7. E. D. Crozier and A. J. Seary, Can. J. Phys. **58**, 1388 (1980); E. D. Crozier, in *EXAFS Spectroscopy: Techniques and Applications*, edited by B. K. Teo and D. C. Joy (Plenum Press, New York, 1981), Chap. 6, pp. 89–101.

8. G. Aquilanti *et al.*, J. Synchrotron Rad. **6**, 251 (1999).

9. Y. Katayama, O. Shimomura, and K. Tsuji, J. Non-Cryst. Solids **250–252**, 537 (1999).

10. R. B. Greegor and F. W. Lytle, Phys. Rev. B **20**, 4902 (1979).

11. K. Tamura *et al.*, J. Non-Cryst. Solids **150**, 351 (1992).

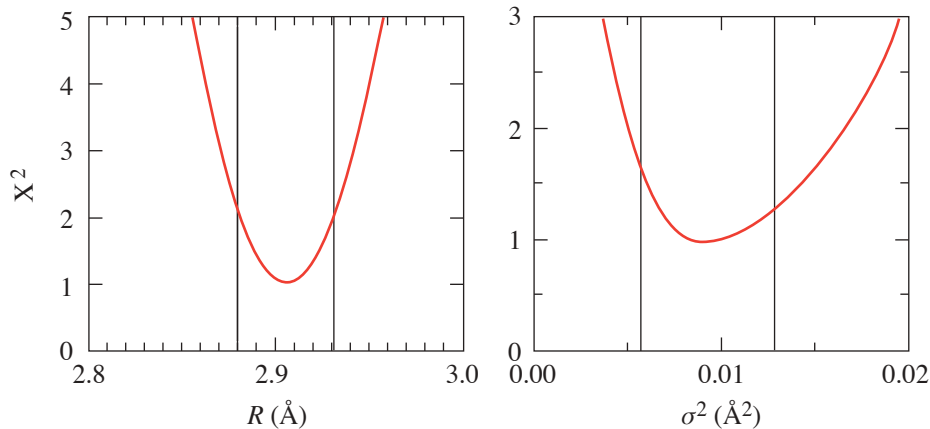12. Y. Nishihata *et al.*, J. Phys., Condens. Matter **6**, 9317 (1994).

Figure 94.49
EXAFS spectrum fitting for the unshocked case (Fig. 94.43): the variation of X^2 with R for the optimal value of σ^2 and with σ^2 for the optimal value of R. The vertical lines show the standard deviation obtained from an inverse-Hessian analysis of X^2.

E11981

13. G. Dalba and P. Fornasini, J. Synchrotron Radiat. **4**, 243 (1997).

14. Y. Soldo *et al.*, Phys. Rev. B **57**, 258 (1998).

15. A. Yoshiasa *et al.*, J. Synchrotron Rad. **6**, 43 (1999).

16. L. Comez *et al.*, Phys. Rev. B **65**, 014114 (2002).

17. A. Trapananti, A. Di Cicco, and M. Minicucci, Phys. Rev. B **66**, 014202 (2002).

18. R. C. Albers, A. K. McMahan, and J. E. Müller, Phys. Rev. B **31**, 3435 (1985).

19. A. Sadoc, J. P. Itie, and A. Polian, Philos. Mag. A, Phys. Condens. Matter Struct. Defects Mech. Prop. **80**, 2057 (2000).

20. P. A. Rigg and Y. M. Gupta, Phys. Rev. B **63**, 094112 (2001).

21. A. Hopkins and N. S. Brar, in *Shock Compression of Condensed Matter – 1999, AIP Conference Proceedings 505*, edited by M. D. Furnish, L. C. Chhabildas, and R. S. Hixson (American Institute of Physics, New York, 2000), pp. 423–426.

22. R. W. Eason *et al.*, J. Phys. C, Solid State Phys. **17**, 5067 (1984).

23. B. A. Shiwai *et al.*, Laser Part. Beams **10**, 41 (1992).

24. B. Yaakobi, F. J. Marshall, D. K. Bradley, J. A. Delettrez, R. S. Craxton, and R. Epstein, Phys. Plasmas **4**, 3021 (1997).

25. B. Yaakobi, F. J. Marshall, T. R. Boehly, R. P. J. Town, and D. D. Meyerhofer, J. Opt. Soc. Am. B **20**, 238 (2003).

26. T. R. Boehly, R. S. Craxton, T. H. Hinterman, J. H. Kelly, T. J. Kessler, S. A. Kumpan, S. A. Letzring, R. L. McCrory, S. F. B. Morse, W. Seka, S. Skupsky, J. M. Soures, and C. P. Verdon, Rev. Sci. Instrum. **66**, 508 (1995).

27. G. Blanche *et al.*, Ultramicroscopy **50**, 141 (1993).

28. A. Balzarotti, M. De Crescenzi, and L. Incoccia, Phys. Rev. B **25**, 6349 (1982).

29. D. A. Young, *Phase Diagrams of the Elements* (University of California Press, Berkeley, CA, 1991).

30. C. W. Greeff, D. R. Trinkle, and R. C. Albers, J. Appl. Phys. **90**, 2221 (2001).

31. R. G. McQueen *et al.*, in *High-Velocity Impact Phenomena*, edited by R. Kinslow (Academic Press, New York, 1970), Chap. VII, pp. 293–417.

32. H. Xia *et al.*, Phys. Rev. B **42**, 6737 (1990).

33. Y. K. Vohra and P. T. Spencer, Phys. Rev. Lett. **86**, 3068 (2001).

34. A. K. Singh, M. Mohan, and C. Divakar, J. Appl. Phys. **53**, 1221 (1982).

35. H. Dammak, A. Dunlop, and D. Lesueur, Philos. Mag. A, Phys. Condens. Matter Struct. Defects Mech. Prop. **79**, 147 (1999).

36. B.-K. Teo and P. A. Lee, J. Am. Chem. Soc. **101**, 2815 (1979).

37. A. G. McKale *et al.*, J. Am. Chem. Soc. **110**, 3763 (1988).

38. G. Beni and P. M. Platzman, Phys. Rev. B **14**, 1514 (1976).

39. R. M. More *et al.*, Phys. Fluids **31**, 3059 (1988).

40. P. A. Lee and J. B. Pendry, Phys. Rev. B **11**, 2795 (1975).

41. J. Mustre de Leon *et al.*, Phys. Rev. B **44**, 4146 (1991).

42. J. J. Rehr and R. C. Albers, Rev. Mod. Phys. **72**, 621 (2000).

43. E. A. Stern, B. A. Bunker, and S. M. Heald, Phys. Rev. B **21**, 5521 (1980).

44. B. L. Henke *et al.*, J. Opt. Soc. Am. B **3**, 1540 (1986).

45. G. B. Zimmerman and W. L. Kruer, Comments Plasma Phys. Control. Fusion **2**, 51 (1975).

46. P. M. Celliers *et al.*, Appl. Phys. Lett. **73**, 1320 (1998).

47. R. F. Trunin, G. V. Simakov, and A. B. Medvedev, Teplofiz. Vys. Temp. **37**, 881 (1999).

48. N. Dimakis and G. Bunker, Phys. Rev. B **58**, 2467 (1998).

49. J. A. Moriarty, D. A. Young, and M. Ross, Phys. Rev. B **30**, 578 (1984).

50. W. H. Press *et al.*, *Numerical Recipes: The Art of Scientific Computing* (Cambridge University Press, Cambridge, England, 1987), Chap. 14, pp. 498–546.

Modeling Temperature and Pressure Gradients During Cooling of Thin-Walled Cryogenic Targets

Introduction

High-quality targets must be provided to achieve successful results from OMEGA cryogenic experiments.[1] One type of target is a thin-walled polymer capsule with a fuel layer of solid deuterium (D_2) or deuterium/tritium (DT) ice, approximately 100 μm thick, uniformly distributed on the inner wall of the capsule.[2] To create the fuel layer, the capsule is placed in a room-temperature pressure vessel and slowly pressurized, filling the capsule by permeation through the polymer wall.[3] The capsule is slowly cooled to the critical point (~38.3 K for D_2) to first liquefy the gas, and then further cooled to freeze it. The mass of ice is made uniform through layering techniques.[4] Because of the capsules' fragile nature and the great amount of time required to fill them, the cooling process is a critical phase of operation for providing cryogenic targets.

The filling and cooling of the capsules takes place in the permeation cell. The permeation cell is a pressure vessel constructed of A-286, a high-strength Ni-based superalloy, which contains an insert bearing the capsules called the target rack. The permeation cell contains two parts: (1) an outer surface that carries the mechanical load designed to contain up to 1500 atm and (2) an inner surface that is the outer wall of the pressure vessel. This inner surface has a heater and silicon-diode temperature sensors bonded to it. The outer surfaces are actively cooled by helium gas at 8 K flowing through a tube wound around the outside of the permeation cell. The temperature inside the permeation cell is measured by silicon temperature sensors imbedded at various locations and is maintained by regulating the helium flow and the power to the heater on the core around the target rack. The capsules are fixed in "C-mounts" between four threads of spider silk and placed into the target rack, which is inserted into the center of the permeation cell.[5] The target rack is designed to minimize free volume around the capsule and is constructed of high-conductivity copper to minimize temperature gradients.

This article presents the results of both a steady-state analysis and a transient analysis of the pressure differences across the wall of a thin-walled capsule during the cooling process. The analyses were separated to quantify the effects that each phenomenon contributes. The steady-state contribution to the pressure difference arises from two sources: (1) the different thermal contractions of the materials that comprise the permeation cell and capsule and (2) the room-temperature volume of gas in the line connecting the permeation cell to the isolation valve. An optimum value for the room-temperature volume has been found that minimizes the burst and buckle pressures and allows for 1- and 3-μm-wall capsules to be filled. The transient analysis considered the pressure differences across the capsule wall that arise from temperature changes to the permeation cell. A 3-μm-wall capsule can withstand changes of 1 K at warmer temperatures, while a 1-μm-wall capsule should not be subjected to sudden temperature changes of more than 0.1 K. A cooling program that incorporates permeability at higher temperatures and safely maintains the capsule within the critical burst and buckle pressures allows the time to reach the frozen state to be reduced by over 30%.

Effect of Thermal Contraction and Room-Temperature Volume

Targets to be filled with D_2 or DT are held at room temperature while the pressure is raised at a slow, steady rate, typically to 1000 atm. The pressurization rate is based on the permeability of the capsule wall and its strength against buckling. To assure the capsule's survival, the pressurization rate is kept below P_{buckle}/τ, where P_{buckle} is the buckling pressure and τ is the permeation time constant. For a glow discharge polymer (GDP) capsule of 920-μm diameter with a 3-μm wall, $P_{buckle} \cong 1$ atm and $\tau \cong 30$ s, which allows a 1000-atm fill in 11 h. It is assumed, for safety, that the fill proceeds 30% more slowly than the maximum rate. If the wall thickness is 1 μm, $P_{buckle} \cong 0.1$ atm and $\tau \cong 10$ s, which requires 36 h for a similar fill. When the GDP capsules are fabricated, modifying the deposition conditions for the GDP[6] can result in increased P_{buckle} along with higher permeability, which should allow slightly more rapid filling. After filling, a valve is closed, which isolates the permeation cell from the compressor, and the permeation cell is slowly cooled. The cooling proceeds slowly in order to (1) minimize thermal gradients in the permeation

cell and (2) allow some permeation through the capsule wall in response to a pressure differential that develops during the cooling process.

The pressure differential across the capsule wall arises partly because of a small room-temperature volume connected to the permeation cell, and partly because of differences in the thermal contraction between the polymer capsule wall and the metals of the permeation cell. The small room-temperature volume formed by the isolation valve and the tube connecting this valve to the permeation cell exists because of the unavailability of a suitable cryogenic valve. This room-temperature volume generates an external pressure on the capsule because the increasing density of the gas, as it cools, draws some of the less-dense room-temperature gas into the permeation cell. Simultaneously, the thermal contraction of both the polymer of the capsule wall, which is nearly four times greater than the contraction of the stainless steel of the permeation cell, and the copper of the target rack tends to create an excess internal pressure in the capsule.

To assess these competing effects, the pressure across the capsule wall during the cooldown is calculated for various values of room-temperature volume. These calculations use the NIST equation of state for deuterium,[7] which expresses pressure as a 24-term function of density and temperature. Starting with room-temperature volumes for the permeation cell, the copper target rack, and the small external volume, the molar content is calculated, assuming a 1000-atm fill. At each reduced temperature, the volumes of the cooled elements are recalculated based on the thermal contraction values for copper and stainless steel.[8] The portion of the connecting tube between the room-temperature volume and the permeation cell that has a thermal gradient on it—one-quarter as large as the room-temperature volume—is treated as being part of the room-temperature volume. While varying the temperature of the permeation cell, the pressure and density in the cell are determined by solving three simultaneous equations: (1) conservation of the sum of the molar content of the permeation cell and the room-temperature volume, taking thermal contraction into account; (2) equating the pressure in the permeation cell with that in the room-temperature volume; and (3) applying the deuterium equation of state.

To calculate the pressure in the capsule during the cooldown, a temperature is arbitrarily selected below which the capsule is assumed to be impermeable. This strategy is justified by the sharp decrease in permeability with temperature generally exhibited by polymers, following the Arrhenius

relation. The activation energy for this process has not been measured for the GDP shell material, so the temperature at which the shell becomes effectively impermeable is unknown; however, comparison to polystyrene,[9] which has a similar value of room-temperature permeability, suggests this temperature is in the range of 160 K to 240 K, depending on wall thickness and cooling rate. Within this temperature range, the permeation time constants of capsules with wall thicknesses of 1 to 3 μm range from 10 to 60 min. At lower temperatures, no significant permeation occurs with practical rates of cooling, such as 0.1 K/min. Vapor-deposited polyimide, which is less permeable,[10] becomes effectively impermeable in the temperature range of 220 K to 290 K, if it is previously unstrained. The thermal contraction of GDP is estimated by scaling the polystyrene data[9] with a contraction value measured for a GDP sample cooled from room temperature to 77 K. The length of this flat sample was found to decrease by 0.99% when immersed in liquid nitrogen, compared to 1.32% for the polystyrene data. To estimate the GDP contraction as a function of temperature, the polystyrene data are multiplied by 0.75, the ratio of the GDP value to the polystyrene value at 77 K.

The results of these calculations are shown in Figs. 94.50–94.53. In Fig. 94.50, it is seen that if the room-temperature volume is zero (i.e., if there was a cryogenically cooled isolation valve), a substantial bursting pressure is generated. It is also seen that if there was no shell contraction, the pressure differential generated would be external—a buckling pressure. Comparing Fig. 94.51 to Fig. 94.50, it is seen that adding a relatively small room-temperature volume of 0.3 cc changes the result from a strong bursting pressure to a strong buckling pressure. In Fig. 94.52, an effective compromise between these cases is shown. Reducing the warm volume to 0.11 cc yields a tolerable buckling pressure that a thin-walled capsule should survive and a similarly modest bursting pressure. This conclusion seems to hold regardless of what temperature in the range 160 K to 240 K best represents the effective point at which the capsule becomes impermeable. Other values of warm volume were tried, and 0.11 cc was found to be an optimum value. The volume actually achieved, however, after insertion of volume reducers is estimated to be 0.17 cc. Figure 94.53 plots the pressure differential across the capsule as a function of temperature for various temperatures at which the capsule could become impermeable. A positive pressure differential exceeding 1.5 atm develops, easily buckling a capsule with a 1-μm wall.

The expected buckling pressures shown in Fig. 94.53 for capsules with 1-μm and 3-μm wall thickness are calculated
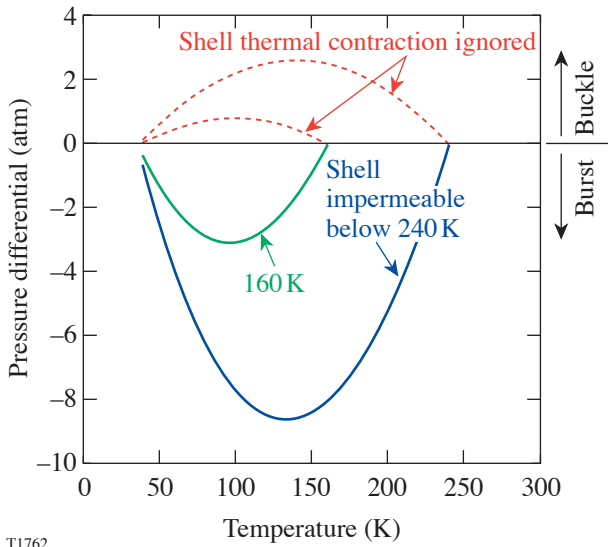
T1762

Figure 94.50
The calculated pressure differential across a capsule wall (assumed inelastic) is plotted for the case of zero room-temperature volume. The capsule is permeated with 1000 atm of D_2 and then cooled slowly to 25 K or lower. The dashed lines indicate the excess external pressure (buckling pressure) that would occur if thermal contraction of the permeation cell is taken into account, but not thermal contraction of the capsule. The solid lines include capsule contraction and show a large bursting pressure. If the capsule becomes impermeable at 240 K, a very large burst pressure is generated, while permeability at temperatures down to 160 K, followed by impermeability at lower temperatures, produces more-modest internal pressures.
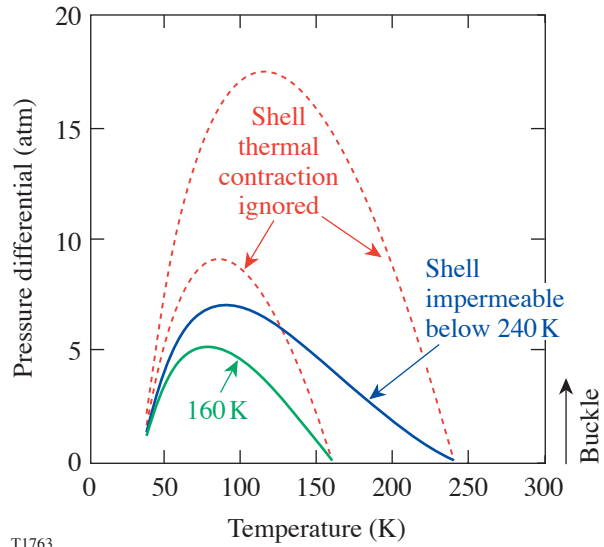
T1763

Figure 94.51
The calculated pressure differential across a capsule wall is plotted for a realistic room-temperature volume of 0.3 cc and a permeation cell volume of 5 cc. The dashed lines ignore thermal contraction and the solid lines include it. An excess pressure external to the capsule arises that would cause any thin-walled capsule to buckle. An inelastic capsule is assumed. The room-temperature volume is reduced from this value by insertion of spacers.
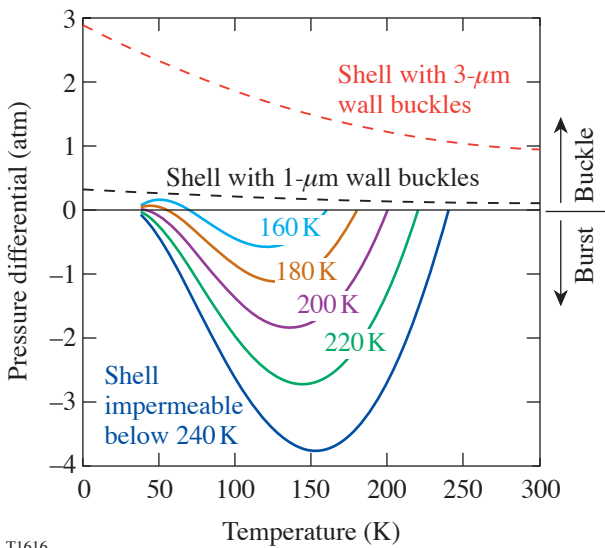
T1616

Figure 94.52
The calculated pressure differential across a capsule wall is plotted for a small value of room temperature volume for various temperatures at which the capsule could become impermeable. The dashed lines indicate the buckling pressure of capsules with 1- and 3-μm walls. Reducing the room-temperature volume to 0.11 cc reduces the buckling pressure to a level that is survivable by an inelastic shell with a 1-μm wall. While this volume appears optimal, it would be difficult to achieve such a small volume.

using values of Young's modulus inferred from measuring the buckling pressures of a group of GDP capsules at various temperatures. It is found that Young's modulus increases significantly upon cooling, reaching a value at 10 K of 2.5× the value at room temperature.
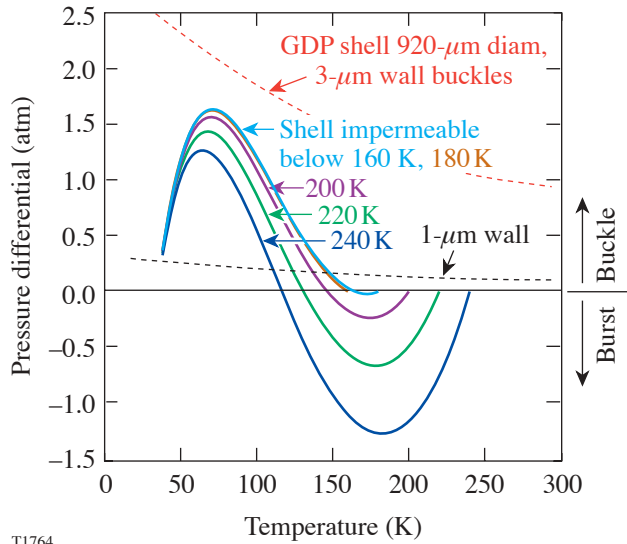
T1764

Figure 94.53
The calculated pressure differential across an inelastic capsule wall is plotted for an achievable room-temperature volume of 0.17 cc for various temperatures at which the capsule could become impermeable. The dashed lines show the buckling pressures for capsules with 1- and 3-μm walls. The thicker-walled capsules would survive, while the thinner-walled ones would not.

Effect of Shell Elasticity

The preceding calculations do not take into account the expansion or shrinkage of the capsule due to internal or external pressure. Taking into account dimensional change due to elasticity reduces the resulting differential pressure on the capsule wall,[11] rendering it less vulnerable to bursting or buckling. The calculations assume the capsule wall is perfectly spherical, uniform in thickness, and homogeneous. The fractional change in the radius r is given[12] by

$$\frac{\Delta r}{r} = \frac{r \, \Delta P (1-\nu)}{2 \, E w},$$

(1)

where ΔP is the pressure differential across the wall, ν is Poisson's ratio of the capsule material (the polystyrene value, 0.35, is used here), E is Young's modulus, and w is the wall thickness. While deuterium at the densities of a typical target

fill is far from an ideal gas, it is useful to consider the functional dependence of the pressure differential on elasticity for the ideal gas case. If a pressure differential ΔP_i is applied across a capsule wall, which thereupon undergoes elastic expansion or contraction, the final pressure differential is readily found to be, in the ideal gas case, for $\Delta r \ll r$,

$$\Delta P_f \cong \frac{\Delta P_i}{1 + (P + \Delta P_i) \dfrac{3r(1-\nu)}{2 \, E w}},$$

(2)

where P is the initial pressure inside and outside the capsule. This solution is useful as a check on the non-ideal-gas solution at its low-pressure limit.

To calculate ΔP resulting from a change in the pressure external to the capsule for the non-ideal-gas case, Eq. (1) is solved by applying the deuterium equation of state along with the requirement that the molar content of the capsule is un-changed. The result, dependent on temperature and wall thick-ness, is shown in Fig. 94.54 for the case of a 0.1-atm change in the external pressure. Applying this method to the pressure differential that results from thermal contraction and a room-
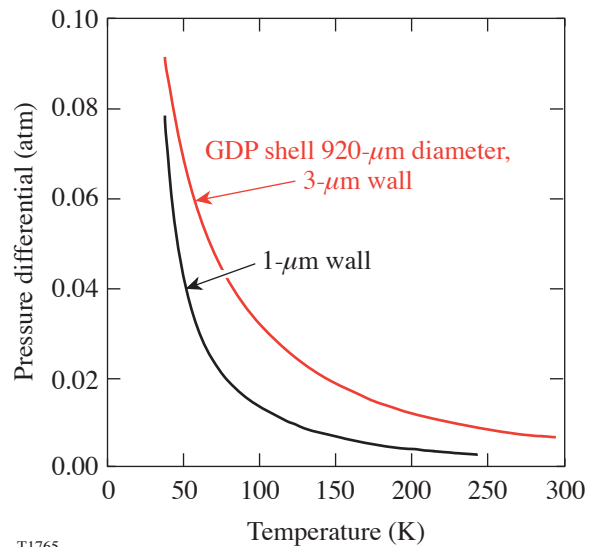
T1765

Figure 94.54
Pressure differential across the wall of an elastic capsule (GDP) that has expanded or contracted due to a 0.1-atm change in external pressure. The capsule diameter is 920 μm, and the wall thickness is 1 or 3 μm. At such a high gas density (~25 mol/L), external pressure changes are substantially attenuated.

temperature volume, the data in Fig. 94.53 are transformed into Fig. 94.55. For a room-temperature volume of 0.17 cc, the maximum pressure differential is reduced from 1.6 atm to 0.5 atm but is still enough to buckle a shell with a 1-μm wall. The buckling problem could be solved by reducing the warm volume to 0.11 cc or by adjusting thermal gradients in the permeation cell. These calculations, showing reduced vulnerability to failure due to capsule elasticity, assume the capsule is perfectly spherical and of uniform wall thickness, and have not been tested experimentally.
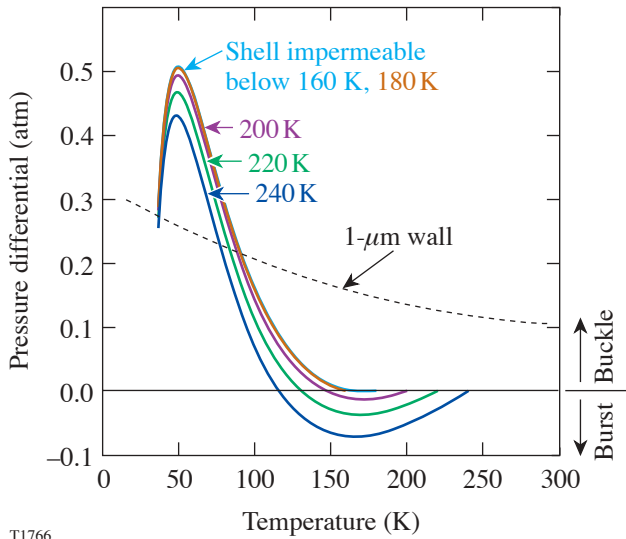
Figure 94.55
Pressure differential across an elastic capsule (GDP) wall of 1-μm thickness and 920-μm diameter, and a room-temperature volume of 0.17 cc. The capsule's buckling pressure (dashed line) is also plotted. While the maximum external pressure is reduced by more than a factor of 3 from the case of the inelastic shell (Fig. 94.53), the capsule's buckling pressure would still be exceeded.

Modeling the Transient Cooling Phase

A computational fluid dynamics (CFD) program is used to calculate the temperature profiles and heat flows inside the permeation cell. Only through modeling can the thermal conditions and the forces on the capsule during the transient cooling phase be quantified. When cooling is enacted, the thermal gradients change inside the permeation cell and therefore across the capsule wall. This temperature difference creates a pressure difference that leads to either a burst or buckling pressure on the capsule. Exceeding the material properties causes the capsule to fail by either bursting or collapsing. As stated previously, the failure pressure of thin-walled capsules is small, and significant pressure differences can occur during transient cooling processes if the cooling rate

is too large. The CFD simulation is used to calculate the resulting pressure difference across the capsule wall caused by cooling steps throughout the temperature range from 294 K to 40 K. These results are used to determine a cooling program that could successfully cool capsules until the fuel freezes while avoiding a pressure difference that may destroy the capsule. Reducing the typically lengthy cooling time increases target production and saves operator effort. A maximized cooling rate is much more important when filling with DT; reducing the cooling time will minimize He[3] buildup and capsule deterioration.

The permeation cell and its components are recreated as a two-dimensional axisymmetric model, shown in Fig. 94.56. The model is comprised of the A-286 superalloy body, lid, and core, the copper target rack, and deuterium gas in the space
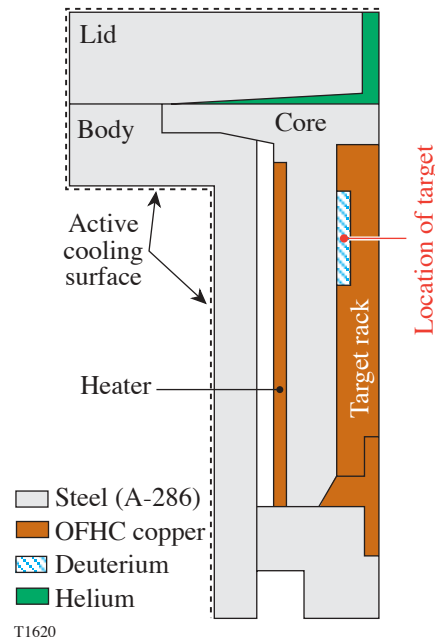
Figure 94.56
A two-dimensional axisymmetric representation of the permeation cell. The properties of the temperature-dependent materials are accounted for in the model. The capsule is located in the center of the gas space around the target rack. The boundary conditions are held on the outer cooling surfaces of the model, and the temperatures are implemented by changing the power to the heater. The averages gas temperatures external and internal to the capsule wall are recorded. The corresponding external and internal pressures, which are a function of temperature and density, are calculated from the deuterium equation of state.

surrounding the capsule and target rack. The capsule is located in the center of the deuterium gas space in the notch of the target rack. The solutions are generated using *FLUENT* computational fluid dynamics software.[13]

The following solution procedure is used to determine the pressure difference across the capsule wall. Temperature boundary conditions are set on the outer surfaces of the model (on the lid and body) and on the heater, as shown in Fig. 94.56. The permeation cell is initially considered isothermal. This assumption is applicable for deuterium—not DT, which generates heat—and is an approximation of the actual conditions. The solver uses the temperature-dependent material properties of the components and gas, which are listed in Table 94.I. These properties span a wide range over the temperature range from 294 K to 40 K. To commence the simulation, the temperature setting on the silicon diode is lowered to enact a cooling step. The temperature in each volume element is recorded as the simulation progresses, and a temperature profile in the permeation cell is generated. The simulation is run until a steady-state final temperature profile develops. This is assumed when the average capsule temperature reaches a steady value. From the instantaneous temperature in each volume element of the model, the time instantaneous and volume-averaged temperatures on either side of the capsule wall are calculated. These average temperatures are converted into average gas pressures from the deuterium equation of state. The average internal and external pressures of the capsule yield the bursting pressure as a function of time.

Cooling steps in increments of 0.125, 0.5, and 1 K are performed at temperatures through the temperature range from 294 K to 40 K. The size of the increments was chosen due to the accuracy of the sensors and the magnitude of actual cooling increments. (The temperature resolution of the sensor is 1 K at 300 K and 0.5 K at 100 K.) After a cooling step is made, the temperature of the gas inside the capsule lags behind that of the external gas and the magnitude of the difference depends on the temperature-dependent physical properties of the gas. The thermal diffusivities of the steel and deuterium are plotted in Fig. 94.57. The gas, which has a thermal diffusivity one to two orders of magnitude less than that of the metals, responds more slowly to temperature changes, and the difference increases at lower temperatures. The difference (ΔT) between the average external (to the capsule) and internal temperatures for three

T1775a
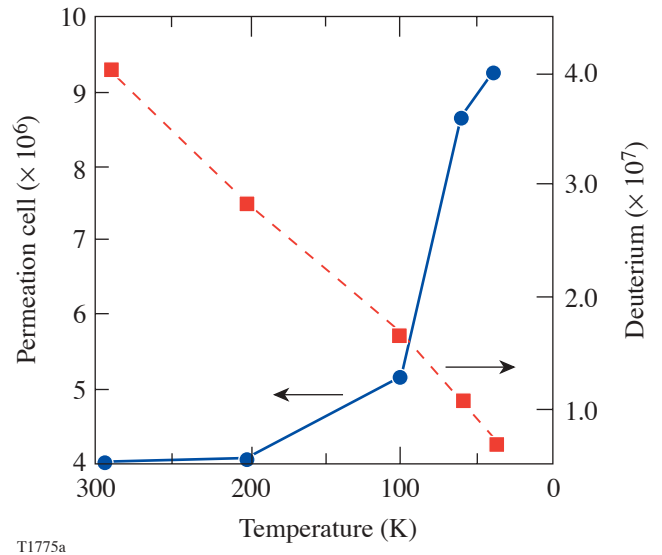
Figure 94.57
The thermal diffusivities of the steel and deuterium as a function of temperature are plotted. The gas, which has a thermal diffusivity one to two orders of magnitude less than that of the metals, responds more slowly to temperature changes, and the difference between the thermal diffusivity of the gas and steel increases at lower temperatures.

Table 94.I: Temperature-dependent properties of materials in the permeation cell model.

	294 K		100 K		40 K	
	C_p	k	C_p	k	C_p	k
Steel	503	16.3	216	9	40	3
Copper	381	388	253	500	60	1000
Deuterium (1000 atm @ 294 K)	7790	0.32	8900	0.15	14300	0.098
C_p = heat capacity (J/kg K)						
k = thermal conductivity (W/m K)						

different cooling steps is shown as a function of time in Figs. 94.58(a)–94.58(c). The largest average ΔT of about −0.2 K for a temperature change of 1.0 K occurs about 10 to 20 s after the change is made, depending at which temperature it occurs. As the temperature of the gas external to the capsule equilibrates, ΔT approaches zero in less than 100 s. The values of ΔT shown in the figures are negative for the case of cooling. It is possible, however, that ΔT becomes positive if the permeation cell was warmed (for example, a cooling power fluctuation or a control error).

The calculated temperature profiles are converted to pressure differences (ΔP) across the capsule wall. For temperature changes made in increments of 0.125, 0.5, and 1.0 K, the temporal pressure difference at temperatures through the cooling cycle are shown in Figs. 94.59(a)–94.59(c), respectively. Since the external temperature is less than the internal temperature, and likewise for the pressures, a burst pressure develops inside the capsule. The pressure gradient reaches a maximum ΔP_{max} before dissipating as the temperatures across the wall equilibrate and/or permeation takes place. In all three cases, more severe pressure gradients occur at lower temperatures. This is explained by the increase of heat capacity and decrease of thermal conductivity of deuterium at reduced temperatures. The gas responds more slowly to thermal changes as the thermal diffusivity decreases. Therefore, as the difference

between the external and internal temperatures increases, so does the pressure difference. As shown, the induced burst pressure approaches 0.9 atm for a temperature change of 1.0 K. This is well within the limits of thin-walled plastic capsules. As mentioned in the previous paragraph, it is possible that ΔP becomes positive if the permeation cell was warmed. If this occurs, a buckling pressure would be applied on the capsule. For a 1-μm-wall GDP capsule, P_{buckle} is ~0.1 to 0.2 atm, and a warming of 0.125 K causes a buckling pressure very near the failure limit. It is therefore essential that 1-μm capsules are not warmed suddenly by more than 0.1 K.

No single cooling step of 1.0 K causes a pressure difference that would burst a capsule of these dimensions. A series of temperature changes, however, in which the next step occurs before the pressures equilibrate can cause ΔP to exceed its bursting pressure. After each cooling step, an amount of time elapses before ΔP vanishes due to temperature equilibration (assuming no permeability). The equilibration times, shown in Fig. 94.60, increase at the colder temperatures of the cooling program. This effect is also attributed to a lower thermal diffusivity of the gas. This suggests that greater consideration must be taken in this temperature regime, namely a slower cooling rate. Likewise, the cooling rate (and associated depressurization rate) may be increased in the initial stages of the cooling program where temperatures are higher.

T1783
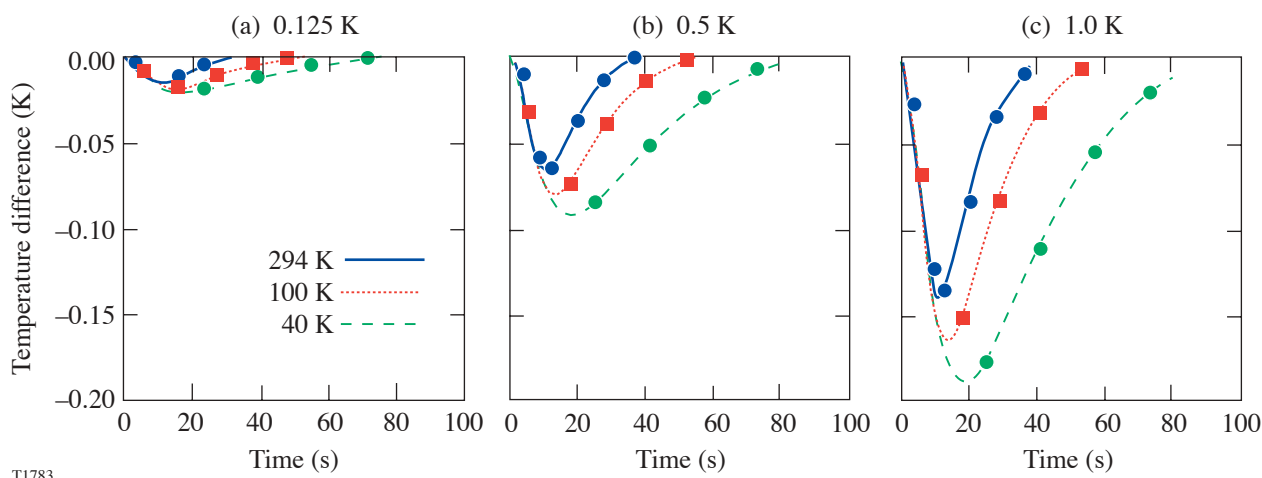
Figure 94.58
The difference (ΔT) between the average external (to the capsule) and internal temperatures for cooling steps of (a) 0.125 K, (b) 0.5 K, and (c) 1.0 K is plotted as a function of time for various temperatures. The largest average ΔT of nearly −0.2 K for a temperature change of 1 K occurs about 10 to 20 s after the change is made, depending at which temperature it occurs. As the temperature of the gas external to the capsule equilibrates, ΔT approaches zero in less than 100 s. The values of ΔT shown in the three figures are negative for the case of cooling. It is possible, however, that ΔT becomes positive if the permeation cell was warmed.

The permeability of the capsule material affects the pressure gradients across its wall. As time elapses, the pressure difference between the external and internal gas will be reduced as the temperatures equilibrate and permeation occurs. Permeation through a polystyrene capsule is temperature dependent and permeability follows the Arrhenius relation:[9]

$$K_p = 1.18 \times 10^{-12} \exp(-1535/T),$$

where K_p is in units of mol/m s Pa and T is in K. The permeation time constant τ of deuterium through polystyrene is given by the equation

$$\tau = wD/6\,K_p RT,$$

where w and D are the capsule's wall thickness and diameter, respectively, and R is the gas constant. (Vapor-deposited polyimide capsules can be less permeable.) Since the gas outside the capsule cools first and reduces pressure, an overpressure inside the capsule occurs for each temperature change. A succession of cooling steps can be viewed as a depressurization rate on the capsule. The maximum-allowable depressurization rate a capsule may experience is expressed as

T1785

Figure 94.60
The amount of time required for the pressure difference to equilibrate across the capsule wall after a cooling step, assuming no permeation, as a function of temperature. Curves for the three different cooling steps are shown. The time increases at lower temperatures due to the increase in thermal diffusivity of the gas.
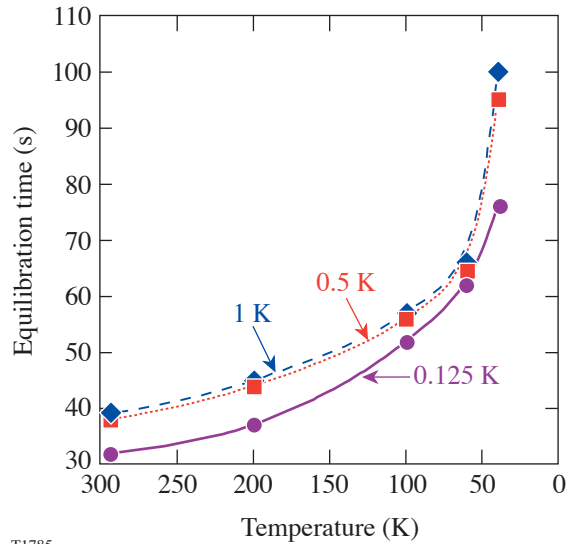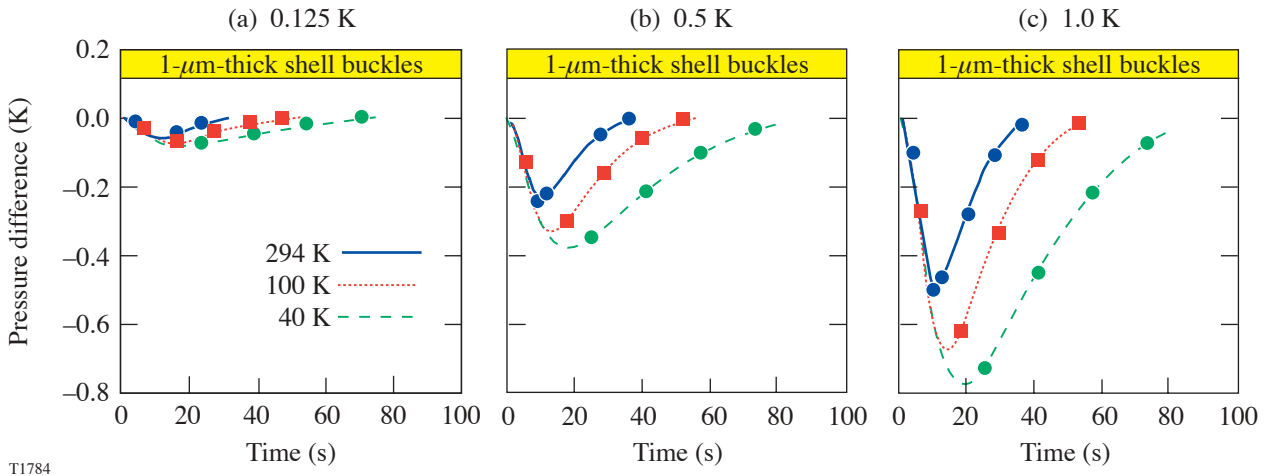

T1784

Figure 94.59
The difference (ΔP) between the external (to the capsule) and the internal gas pressures that arise from cooling steps of (a) 0.125 K, (b) 0.5 K, and (c) 1.0 K is plotted as a function of time for various temperatures. Negative values of ΔP indicate a burst pressure. The external and internal gas pressures, which are a function of temperature and density, are calculated from the deuterium equation of state. The peak ΔP occurs at 10 to 20 s and is more pronounced at lower temperatures. The values of ΔP shown in the three figures are negative for the case of cooling. It is possible, however, that ΔP becomes positive (representing a buckling pressure) if the permeation cell was warmed. The dashed line indicates the value of ΔP at which a 1-μm-wall GDP capsule will buckle. Capsules with a 1-μm-thick wall would easily buckle from positive temperature changes of 0.5 K and 1 K and are near the limit for temperature changes of 0.125 K.

$\sim (P_{burst}/\tau)$, where P_{burst} is the capsule's bursting pressure. The capsule would fail if the bursting pressure was reached while depressurizing at this rate. Assuming a 920-μm-diam capsule with a 3-μm-thick wall and material properties of GDP, the capsule's bursting pressure is ~5.7 atm. Since τ is inversely proportional to temperature and permeability, the maximum-allowable depressurization rate decreases at lower temperatures; thus, cooling should be slowed to prevent capsule breakage. A plot of allowable depressurization rates $(dP*/dt)$ is shown in Fig. 94.61, where, as a safety concern, $(dP*/dt)$ is one-half the maximum value. At the temperature at which the capsule becomes impermeable, $(dP*/dt)$ approaches zero because τ approaches infinity. However, low depressurization rates (~0.1 K/min) are possible because the capsule never reaches P_{burst} before the pressures are balanced by temperature equilibration.

Currently, gas-filled capsules are cooled at a rate of 0.1 K/min from room temperature until the fuel liquefies. Thus, it takes about 45 h to complete the process. A faster cooling program may be achieved by analyzing the pressure differ-
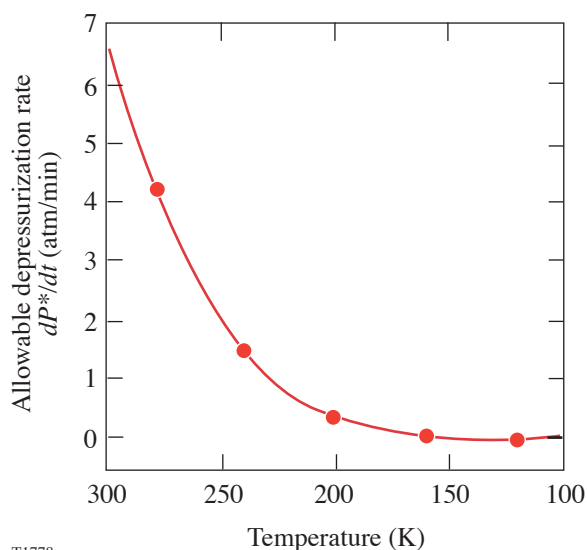
ences on the capsule via modeling. From the cooling-induced pressure differences shown in Figs. 94.59(a)–94.59(c), the maximum pressure difference occurs ~10 to 20 s after the cooling step. From the initial descent portion of each curve (until ΔP_{max}), one can calculate the depressurization rate of the gas outside the capsule that arises from a temperature change. The goal then is to make cooling steps that maintain the depressurization rate below the allowable value $(dP*/dt)$ shown in Fig. 94.61 at each temperature. As shown in Fig. 94.59(c), from 294 K to 255 K, a cooling step of 1 K can be made, which results in ΔP_{max} of 0.48 atm in 10 s. This gives a depressurization rate of 2.9 atm/min, which can be converted back into a cooling rate. To minimize the total cooldown time, a subsequent cooling step should be made at the time ΔP_{max} is reached, about 10 s for the 294-K curve in Fig 94.59(c). Thus a cooling rate of 5 K/min can be performed safely. According to Fig. 94.61, in the temperature range from 255 K to 240 K, it is required that $(dP*/dt)$ be less than ~2 atm/min. From the 294-K curve in Fig. 94.59(b), a cooling step of 0.5 K causes ΔP_{max} of 0.24 atm at 11 s. The use of the 294-K curve at these temperatures is justified because the initial slopes of the 294-K and 200-K curves (the latter is not shown) that cover this temperature range are essentially similar. This corresponds to a depressurization rate of 1.31 atm/min, which is safely within the limit. If another cooling step is made at 11 s (the time when ΔP_{max} is reached), then the subsequent cooling rate is 2.7 K/min. This procedure was continued in a likewise fashion to further choose temperature changes below 240 K that maintain the depressurization rate below $(dP*/dt)$ as cooling progresses. These calculations yield an acceptable cooling program to 40 K, shown in Fig. 94.62, where the minimum rate of 0.1 K/min is used below 200 K. For comparison, the cooldown program used in actual experiments of 0.1 K/min throughout the entire temperature range from 294 K to 40 K is also plotted in the figure. With the revised cooling program, which takes into account permeation at higher temperatures, the total cooling time has dropped from 2450 min to 1670 min, a savings of over 14 h (34% of the total time).

T1778a

Figure 94.61

Allowable depressurization rates $(dP*/dt)$ for a 920-μm-diam, 3-μm-thick-wall capsule as a function of temperature. The allowable rate was one-half the maximum rate for safety considerations. The curve is based on the relationship $(dP/dt) \sim (P_{burst}/\tau)$. The permeability values of polystyrene were used to calculate τ because the temperature-dependent permeability of GDP has not been measured. This approximation is used because of the generally similar Arrhenius behavior of polymers and the similar values of permeability of polystyrene and GDP at room temperature.

When considering the buckling pressure caused by the steady-state effects described earlier (thermal contraction mismatch and room-temperature gas volume) and the burst pressure caused by transient cooling, it is conceivable that one could balance these contributions to develop a faster cooling program. Note that capsules are more susceptible to buckling than bursting. As shown in Fig. 94.55, a dangerous buckle pressure of about 0.2 to 0.5 atm arises while cooling from 100 K to 50 K. In this regime, a cooling step of 0.5 K, which causes a burst pressure of about 0.3 atm, may be used to offset
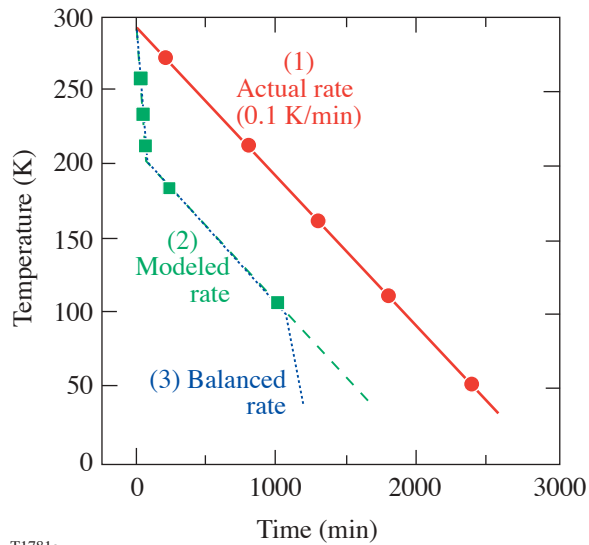
Figure 94.62

Temperature program for cooling a gas-filled capsule to freezing. Three different programs are plotted: (1) the currently used experimental rate (0.1 K/min), (2) a faster rate that accounts for permeation at higher temperatures to offset pressure differences, and (3) a proposed faster rate that accounts for permeation at higher temperatures and allows cooling-induced burst pressures and steady-state-effect buckle pressures to counterbalance each other.

buckling pressure. If a step is made every minute, allowing for the pressure to equilibrate, it is plausible that the total cooling time may be halved to ~1200 min, as shown in Fig. 94.62.

Summary

An analysis of the temperature and pressure gradients in the permeation cell that occur during the cooling of thin-walled cryogenic targets has been presented. Both steady-state and transient effects may cause the capsule to fail during cooling. The steady-state contribution to the pressure difference arises from three sources: (1) the thermal contraction of the materials that comprise the capsule and the permeation cell, (2) the room-temperature volume of gas in the line connecting the permeation cell to the isolation valve, and (3) elastic deformation of the capsule. An optimum value for the room-temperature volume has been found that minimizes the burst and buckle pressures. The transient analysis considered the pressure differences across the capsule wall that arise from temperature changes to the permeation cell. A 3-μm-wall capsule can withstand changes of 1 K at warmer temperatures, while a 1-μm-wall capsule should not be subjected to sudden temperature changes of more than 0.1 K. A cooling program that incorporates permeability at higher temperatures and safely maintains the capsule within the critical burst and buckle pressures allows the time to reach the frozen state to be reduced by over 30%.

REFERENCES

1. Laboratory for Laser Energetics LLE Review **90**, 49, NTIS document No. DOE/SF/19460-437 (2002). Copies may be obtained from the National Technical Information Service, Springfield, VA 22161.

2. D. D. Meyerhofer, C. Chiritescu, T. J. B. Collins, J. A. Delettrez, R. Epstein, V. Yu. Glebov, D. R. Harding, R. L. Keck, S. J. Loucks, L. D. Lund, R. L. McCrory, P. W. McKenty, F. J. Marshall, S. F. B. Morse, S. P. Regan, P. B. Radha, S. Roberts, W. Seka, S. Skupsky, V. A. Smalyuk, C. Sorce, C. Stoeckl, J. M. Soures, R. P. J. Town, J. A. Frenje, C. K. Li, R. D. Petrasso, F. H. Séguin, K. Fletcher, C. Padalino, C. Freeman, N. Izumi, R. Lerche, T. W. Phillips, and T. C. Sangster, presented at the 14th Target Fabrication Meeting, West Point, NY, 15–19 July 2001.

3. Laboratory for Laser Energetics LLE Review **81**, 6, NTIS document No. DOE/SF/19460-335 (1999). Copies may be obtained from the National Technical Information Service, Springfield, VA 22161.

4. M. D. Wittman, D. R. Harding, P. W. McKenty, H. Huang, L. S. Iwan, T. J. Kessler, L. Elasky, and J. Sailer, presented at the 14th Target Fabrication Meeting, West Point, NY, 15–19 July 2001.

5. S. G. Noyes, M. J. Bonino, D. Turner, J. Tidu, and D. R. Harding, presented at the 14th Target Fabrication Meeting, West Point, NY, 15–19 July 2001.

6. A. Nikroo *et al.*, Fusion Sci. Technol. **41**, 214 (2002).

7. R. Prydz, K. D. Timmerhaus, and R. B. Stewart, in *Advances in Cryogenic Engineering*, edited by K. D. Timmerhaus (Plenum Press, New York, 1968), Vol. 13, pp. 384–396.

8. G. K. White, *Experimental Techniques in Low-Temperature Physics*, 2nd ed., Monographs on the Physics and Chemistry of Materials (Clarendon Press, Oxford, 1968), p. 377.

9. L. A. Scott, R. G. Schneggenburger, and P. R. Anderson, J. Vac. Sci. Technol. A **4**, 1155 (1986).

10. F.-Y. Tsai, D. R. Harding, S. H. Chen, T. N. Blanton, and E. L. Alfonso, Fusion Sci. Technol. **41**, 178 (2002).

11. R. Stephens, General Atomics, private communication (2001).

12. W. C. Young, in *Roark's Formulas for Stress & Strain*, 6th ed. (McGraw-Hill, New York, 1989), p. 523.

13. *FLUENT* (version 6.0.20), Fluent USA Inc., Lebanon, NH 03766.

Development of an Elementary Climate Model: Two-Layer Cellular Case

Introduction

The recent gradual increase in Earth's average temperature[1] is generating intense interest in both public and scientific circles. It is important that physicists understand the basic energetics in climatology. While excellent climatology texts such as Hartmann's[2] exist, materials generally available to the undergraduate physics major and instructor lack a systematic physical treatment and an unavoidable terminology barrier exists. The comprehensive and readable work of Peixoto and Oort,[3] written by and for physicists, is at a level too demanding for introductory study. We concentrate solely on some aspects of the basic energy transfer to establish a level suitable for undergraduate teaching; more sophisticated treatments do exist.[4–7]

Despite the complexities of the real atmosphere, the global average temperature of 288 K (Ref. 2, p. 2) may be estimated with remarkably few modifications of the classic homogeneous blackbody model of Earth.[2,8–11] One purpose of developing this article has been to build on our earlier elementary model[9] as realistically as possible, retaining both a physics style and a reasonable mathematical and computational level. We thought it would be of interest to see whether the two-layer model of the energy fluxes could be employed on a regional basis, for which we consider Earth's surface covered by a layer of 864 noninteracting cells. Here we will show that it does appear to be a consistent theory that can provide certain insights. In particular, we find that the cellular radiative energy transports clearly dominate the cellular nonradiative energy flux. We show that this flux has a strong systematic dependence on latitude and time of year. Thus, for this article we wish to avoid using a more precise radiative model of the atmosphere. Also, all heat transmission through the earth's surface is neglected. This precludes a quantitative prediction of the phase difference between the cyclical variations of the solar flux and the surface temperature.

We first briefly review the two-layer model in order to set up notation. In our earlier work[9] the two layers of the Arrhenius model were called, informally, the atmosphere and the surface. Except for one nonradiative flux S_{NR}, all energy transfers were modeled as radiative. The model makes use of the fact that the incoming solar radiation and the outgoing terrestrial radiation occupy distinct spectral regions called respectively, for convenience, UV and IR. The upper layer, at temperature T_A, has a UV reflectivity and absorptivity, r_A and a, respectively, and an IR absorptivity ε. The symbols a and ε are used here in place of f and g in the original article but all other notation is preserved. The surface, at temperature T_E, has a UV reflectivity r_S and is assumed to absorb all incident IR. The solar radiation has a flux $S_0 = 342$ W/m² when averaged over time and over the surface of the earth. When the UV radiation hits the upper layer, a part r_A is reflected and the part that enters the layer is $(1-r_A)$. Of this part, $a(1-r_A)$ is absorbed. In this first pass, the surface therefore receives $(1-r_A)(1-a)$, of which r_S is reflected, leaving $(1-r_A)(1-a)(1-r_S)$ as the fraction of original incident solar flux to be absorbed at the surface. Following this logic, a diagram can be constructed showing all the fractions of absorbed and reflected radiation including the term S_{NR} for nonradiative energy transfer (Fig. 94.63). When multiple reflections are included, a factor $k_M = \left(1 - r_A r_S\right)^{-1}$ appears in terms involving reflections between the surface and atmosphere. The nonradiative flux S_{NR}, which served as an arbitrary model parameter in the global calculation, will be seen to play a much greater role in the current work.

The energy-balance equations for the upper and surface layers take the form

$$2\varepsilon S_A - \varepsilon S_E = AS_0 + S_{NR} \tag{1a}$$

and

$$-\varepsilon S_A + S_E = BS_0 - S_{NR}, \tag{1b}$$

respectively. These equations express net incoming UV and nonradiative flux on the right-hand sides and net outgoing IR flux on the left. Here S_A and S_E are defined as the ideal Stefan–Boltzmann fluxes $S_A = \sigma T_A^4$ and $S_E = \sigma T_E^4$, where $\sigma = 5.67 \times 10^{-8}$ W/m² K⁻⁴. The quantities A and B correspond to the fractions of S_0 ultimately absorbed by the atmosphere and
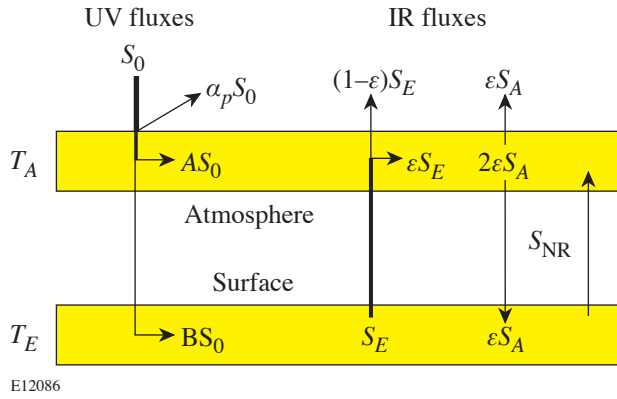
E12086

Figure 94.63
Movement of radiative and nonradiative energy in the two-layer scheme. Horizontal arrows indicate deposition in the layer. Lighter arrows represent radiation that is either reflected or passed through a layer unabsorbed. Multiple reflections of UV radiation are accounted for by the factor k_M in Eqs. (1a) and (1b) in the text. The factors α_p, A, and B are the overall fractions of S_0 that are reflected, absorbed by the upper layer, and absorbed by the lower layer, respectively. Other symbols are defined in the text.

surface, respectively,

$$A = a(1 - r_A) + ak_M(1 - r_A)^2 (1 - a)r_S \qquad (2a)$$

and

$$B = k_M(1 - r_A)(1 - r_S)(1 - a) \qquad (2b)$$

Global and time averages of all the parameters are inserted, and Eqs. (1) are easily solved for S_A and S_E, from which temperatures T_A and T_E are then obtained. This original model was used to investigate broadly the effect of non-solar-related energy sources at the surface.

The following sections (1) extend the model by introducing coarsely grained surface features and locally time averaged fluxes in 864 noninteracting cells; (2) compute and discuss zonal (latitudinal) averages; and (3) summarize and discuss the limitations of the model and possibilities for its further development.

Cellular Model

1. Rationale and Design

We choose the grid scheme used by Hansen *et al.*[12] in which the earth's surface is divided into 864 cells of dimension 8° × 10° (latitude by longitude). We then assume that Eqs. (1) are satisfied within each cell. The next step is to extend the computations from globally time-averaged to locally time-

averaged parameters. For each of the 864 cells, the land fraction and the annually averaged parameters for observed total cloud cover fraction, calculated incoming annual average solar radiation, and land and sea reflectivities are stored. All parameters are determined at the center of the cell, and the values are applied to the entire area of the cell. The energy-balance equations are then solved at each location. For comparison to global values, the local values are weighted by fractional cell area and summed. Our model does not take into account changes in atmospheric components, the parameters' temperature dependence,[11] or any geothermal variations.

All programming is done using MATLAB™, an array-based language with simple commands. In the MATLAB environment, each computation is performed simultaneously on each cell in an identical manner. A very useful source for MATLAB programming styles is the Appendix of a text by Borse.[13]

Before solving the energy-balance equations for the temperatures and emissions of the two layers, the input parameters must be specified. These values have been gathered from different sources. The land fraction $f_{land}(n)$ is taken directly from Hansen *et al.*[12] It is shown by the contours in Fig. 94.64, which establishes the scale and resolution of subsequent maps.

E12087
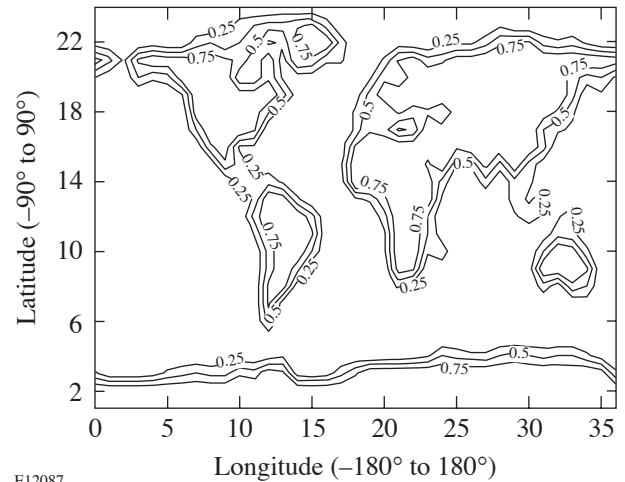
Figure 94.64
Global land fraction plotted with contours at 0.25, 0.5, and 0.75. This map may be used as a template in the study of Figs. 94.66, 94.67, and 94.69. It also gives a good indication of the resolution afforded by our 864-cell calculations. Horizontal axis: ticks correspond to centers of 10° cells located (centered) at longitudes −180°(1), −170°(2), ..., 0°(19), ..., +170°(36). Vertical axis: ticks correspond to centers of 8° cells at latitudes −84°(2), −76°(3), ..., −4°(12), +4°(13), ..., +84°(23). The bottom and top rows correspond to centers of 2° cells at −89°(1) and +89°(24), respectively.

The 18-year-average annual cloud fraction coverage was taken from data collected by satellites from 1983 to 2001 under the International Satellite Cloud Climatology Project.[14] Similarly, surface reflectivities (r_S) were estimated by using the ISCCP surface reflectivities in coordination with Table 4.2 in Hartmann.[2] Hartmann specifies albedo ranges and typical values for distinct land types. Table 94.II shows the land types, albedo ranges, and typical albedo values. The estimates of r_S are shown in Table 94.III.

It might appear that a serious approximation is being made in neglecting net annual lateral transport of energy. Lateral heat flows, however, will be effectively redirected into a vertical heat flux; the quantity S_{NR} will contain this contribution. Consider, for example, a horizontal wind, carrying water vapor from one cell to the next. When the vapor precipitates in the

form of rain, it releases latent energy. That energy release contributes to the vertical energy balance in the (receptor) cell. This energy enters "horizontally" into the cell. Similarly, in some nearby cell, some vertical energy flux went into evaporation, and that cell suffers an energy loss if the water vapor is transported out of the cell. Since our cells are large, we do not expect the horizontal energy transport to cover more than one or two cells, for local disturbances. Consequently there may be a correlation between a loss of S_{NR} in one cell and a gain in S_{NR} in a nearby cell. The annual latitude dependence of S_{NR}, which will be discussed in the last section, may well be made up of such transport contributions. A less obvious but very significant assumption is that the theory continues to work at latitudes having long periods of low solar irradiance, when cloud cover may vary significantly between polar winter and summer periods. This requires negative values of S_{NR} to maintain flux

Table 94.II: Land types and their associated albedo ranges (in percentages) deduced from a map [Fig. 5.14, by Dickinson (Ref. 18); Table 4.2 by Hartmann (Ref. 2)].

Land type (Dickinson)	Land type (Hartmann)	Albedo range	Typical value
Tundra and desert	Dry soil/desert	20–35	30
Grass and shrub	Short green vegetation	10–20	17
Crop	Dry vegetation	20–30	25
Wetland and irrigated	Short green vegetation	10–20	17
Evergreen tree	Coniferous forest	10–15	12
Deciduous tree	Deciduous forest	15–25	17

Table 94.III: Corrected values for land and sea reflectivities in the high latitudes (see text). A negative latitude corresponds to the southern hemisphere. For −76° to −89° r_{land} is set at 0.6 because of the year-round Antarctic ice. The latitude −68° reflectivity is set slightly lower than Antarctica as a result of a lack of permanent ice. In latitudes 68° to the north pole, r gradually increases, taking seasonal snow and ice into account. r_{sea} at 60° and −60° is set at 0.3 to avoid a sharp jump from water set at 0.1 in the mid-latitudes to the higher polar values for ice and snow cover. These values are rough estimates for partial and seasonal snow and ice cover. Fresh snow can have an albedo up to 0.9, old, melting snow up to 0.65, and sea ice without snow cover up to 0.4 (see Ref. 2, Table 4.2, p. 88). Values not shown (—) are longitude dependent and are taken directly from satellite data in detail.

Latitude (°)	−89	−84	−76	−68	−60	−52 to 52	60	68	76	84	89
r (land)	0.6	0.6	0.6	0.55	—	—	—	0.4	0.5	0.55	0.6
r (sea)	0.6	0.6	0.6	0.55	0.3	—	0.3	0.4	0.5	0.55	0.6

balance. Negative values of S_{NR} may represent fluxes from a missing reservoir layer, which is planned for a future refinement of the model.

2. Cellular Values of Parameters

    The value of a parameter g that depends on the choice of cell will be written $g(n)$, where, unless otherwise specified, n is an arbitrarily assigned cell number. To calculate the incoming solar radiative flux to a cell, we use astronomical definitions and notations to track the sun's position relative to a cell's midpoint every two weeks throughout the year. The incident radiation is the solar radiation at the distance to the earth, 1368 W/m² multiplied by the sine of $H(n)$, where $H(n)$ is the angle of the sun from the horizon of the surface area in cell n,

$$S_0(n) = 1368 \sin H(n,t,t') \ \left(\text{Wm}^{-2}\right). \qquad (3)$$

Here (see Appendix and Ref. 2, pp. 29–31 and 347–349)

$$\sin H(n,t,t') = \sin \delta(t') \sin \beta(n) + \cos \delta(t') \cos \beta(n) \cos t, \qquad (4)$$

where β is the latitude, δ is the sun's declination angle, t' is the time elapsed since the vernal equinox, and t is the hour angle. During the average over 24-h periods, the angle t is limited by sunrise and sunset conditions, i.e., there is no contribution when $\sin H$ is negative. The annual average of S_0 as a function of latitude computed from Eq. (3) is plotted in Fig. 94.65,
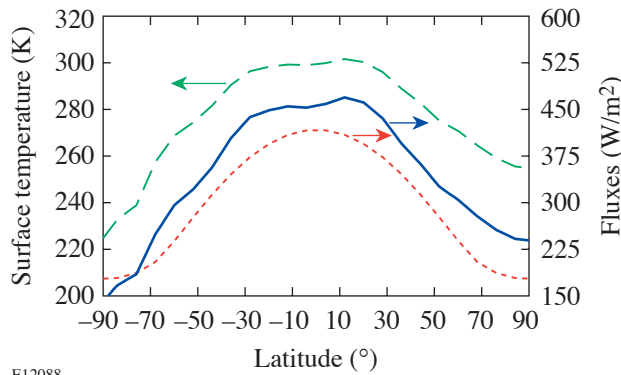
E12088

Figure 94.65
Average annual insolation (lower curve, right-hand scale), outward infrared flux at the surface (solid curve, right-hand scale), and surface temperature (upper curve, left-hand scale) as a function of latitude. The latter two are latitude averages based on satellite data.[15]

along with the observed S_E and T_E. Equation (3) is adequate for the purposes of our average annual model. Monthly averages require a slight correction resulting from Earth's orbital eccentricity (see, e. g., Hartmann[2]). The annual average solar irradiance ranges from a minimum of 176 W/m² at the poles to 416 W/m² at the equator, with a global annual average of 342 W/m².

The UV parameters A and B [Eqs. (2a) and (2b)] also become cell dependent. There are three relevant cell-varying parameters, the UV reflectivities and the absorptivity of the cloud layer. The surface reflectivity $r_S(n)$ of cell n is taken from sea and land reflectances weighted by the corresponding surface-type fractions,

$$r_s(n) = f_{\text{land}}(n) r_{\text{land}} + \left[1 - f_{\text{land}}(n)\right] r_{\text{sea}}. \qquad (5)$$

This formula was used only in high-latitude regions ($|\text{lat}| \geq 60°$). Remaining reflectivities came from ISCCP data.[14,15] The atmospheric reflectivities are similarly found to be

$$r_A(n) = f_{\text{cloud}}(n) r_{\text{cloud}} + \left[1 - f_{\text{cloud}}(n)\right] r_{\text{clear}}, \qquad (6)$$

where the clear air albedo (r_{clear}) can be assumed as 0.15 (Ref. 2, page 75). The planetary albedo $\alpha_P(n)$ is the fraction of original incident UV that leaves the system. On our model [see Ref. 5, Eq. (B3)] it is given by

$$\alpha_P(n) = r_A(n) + k_M(n) \left[1 - a(n)\right]^2 \left[1 - r_A(n)\right]^2 r_S(n), \qquad (7)$$

which depends upon two unknowns: $a(n)$, the atmospheric UV absorptivity, and r_{cloud} [through r_A, Eq. (6)]. For absorptivity, the expression corresponding to (6) is

$$a(n) = f_{\text{cloud}}(n) a_{\text{cloud}} + \left[1 - f_{\text{cloud}}(n)\right] a_{\text{clear}}. \qquad (8)$$

If we assume that clear air absorbs no UV radiation, we have

$$a(n) \cong f_{\text{cloud}}(n) a_{\text{cloud}}. \qquad (9)$$

To determine r_{cloud} and a_{cloud}, we impose a set of reasonable planetary albedo values [Ref. 2, Fig. 2.9(a), p. 33] as a constraint upon Eq. (7). Values of r_{cloud} and a_{cloud} were varied at intervals of 0.01 until we had the greatest number of matches

with the known $\alpha_P(n)$. With this bare minimum of free parameters, a match to observed values occurred in 711 of the 864 cells. Most of the unmatched (meaning more than 15% difference from the Hartmann) values were near the poles. The resulting $r_{cloud} = 0.27$ and $a_{cloud} = 0.06$ are in reasonable agreement with the parameters found in Ref. 9. These produce not only a good localized match but also give the commonly accepted global planetary albedo of 0.30 when averaged. Once adopted, these values of r_{cloud} and a_{cloud} are not changed in the course of the calculations.

The cellular IR absorptivity $\varepsilon(n)$, which is also the cellular IR emissivity, is taken to have the same form as the UV absorptivity, Eq. (8). Parameters used were $\varepsilon_{cloud} = 1$ and $\varepsilon_{clear} = 0.90$.

Application of the Model

1. Predicting $T_E(n)$

We now generalize Eqs. (1a) and (1b) to the cellular case:

$$2\varepsilon S_A(n) - \varepsilon S_E(n) = A(n) S_0(n) + S_{NR}(n) \qquad (10a)$$

and

$$-\varepsilon S_A(n) + S_E(n) = B(n) S_0(n) - S_{NR}(n). \qquad (10b)$$

$A(n)$ and $B(n)$ are given by equations identical to Eqs. (2a) and (2b) in which certain parameters are made cell dependent, as discussed above.

Our first attempt with the cellular model was a direct 864-cell extension of the methodology of the earlier one-cell or one-dimensional two-layer model. We refer to this application of the model as "T_E predictive." We allowed the annual average value of $S_{NR}(n)$ to depend on land and sea fraction and took it to be proportional to the solar input, as follows:

$$S_{NR}(n) = \left[0.03 f_{land}(n) + 0.16 f_{sea}(n)\right] \cdot S_0(n). \qquad (11)$$

From the solution of each pair of Eqs. (10a) and (10b) for $S_E(n)$, $T_E(n)$ was calculated on the basis of the assumed $S_{NR}(n)$. The numerical coefficients in Eq. (11) were chosen by an extensive search of parameter space to produce the observed global average temperatures ($T_E = 288$ K, $T_A = 250$ K). This flux has a global average of 42.3 W/m^2, an improvement on the one-dimensional model[9] in that the latter had been unable to

accommodate *any* non-zero average S_{NR} without compromising other assumed input parameters. We emphasize that the only completely arbitrary parameters in the fit were the two numerical coefficients in Eq. (11). We consider this remarkable; it endorses the general reasonableness of the elementary two-temperature model for individual cells. The form of Eq. (11) also suggests a global asymmetry in the distribution of S_{NR}. We will return to this later.

The preliminary cell results are shown in Fig. 94.66(a) and are compared with measured values [satellite data;[15]

Figure 94.66
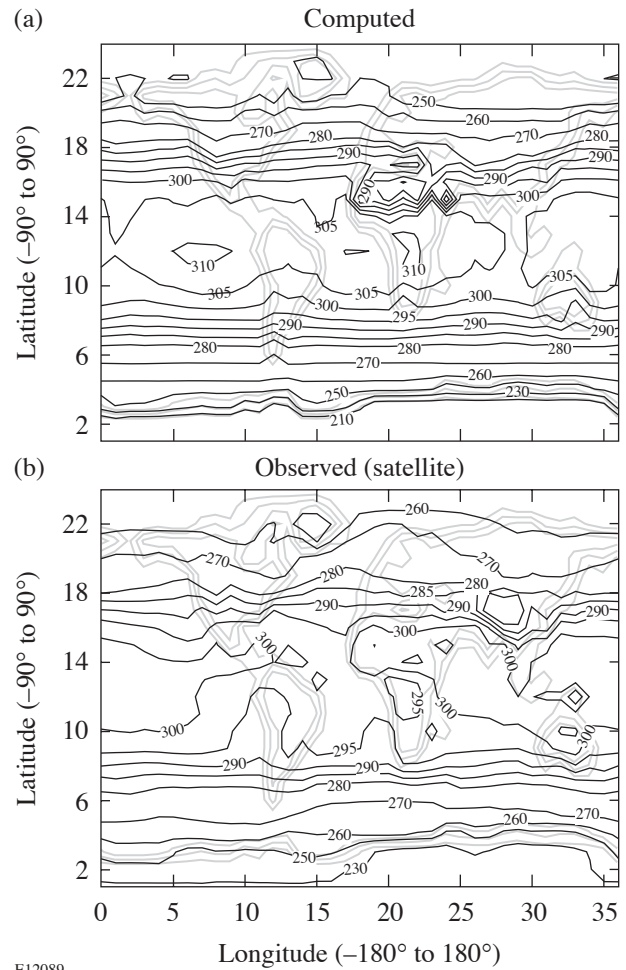(a) Computed "T_E-predictive mode" surface temperatures (in K) using a direct cellular extension of the elementary model of Ref. 9, as described in the text. The average nonradiative flux is 40 W/m^2 and the average surface temperature is 288 K. (b) Observed surface temperatures, defined as those obtained by satellite,[15] with an average of 288 K. (See the caption of Fig. 94.64 for the key to the axes.)

Fig. 94.66(b)]. These diagrams show how a set of calculated locally determined temperatures [Fig. 94.66(a)] having the correct global average may disagree significantly from observed local values [Fig. 94.66(b)] having the same global average. While this is not the least bit surprising, a comparison of the two parts of Fig. 94.66 provides a qualitative evaluation of the errors that occur in the making of simple models. The agreement is closer than one might reasonably expect from simplistic models but the determined set is far from unique.

2. Predicting $S_{NR}(n)$

Because of the difficulty choosing the coefficients of Eq. (11) to produce a match with observations [Figs. 94.66(a) and 94.66(b)], we made a major change in operational procedure. The linear Eqs. (1a) and (1b) or (10a) and (10b) lend themselves equally to computing any two of the quantities S_{NR}, S_A, and S_E, given the third one and S_0 as an input. Therefore, instead of adjusting the value of S_{NR} to predict observed local surface temperatures, we did the opposite: taking $T_E(n)$ as a known input parameter from ISCCP satellite data[11] and $S_0(n)$ from Eq. (3), we used the balance equations to calculate $S_A(n)$ and $S_{NR}(n)$. This "S_{NR}-predictive" mode of calculation is accomplished most easily by combining the two flux Eqs. (10a) and (10b):

$$S_{NR}(n) = \left[A(n) + 2B(n) \right] S_0(n) - (2 - \varepsilon) S_E(n). \quad (12)$$

Recall that $S_E(n) = \sigma T_E(n)^4$. Eliminating S_E from (10a) and (10b) results in the companion equation for S_A:

$$\varepsilon(2 - \varepsilon) S_A(n)$$

$$= \left[A(n) + \varepsilon B(n) \right] S_0(n) + (1 - \varepsilon) S_{NR}(n). \quad (13)$$

The results for the annual average of $S_{NR}(n)$, calculated from the observed surface temperature $T_E(n)$, are shown in Fig. 94.67(a). $S_{NR}(n)$ and $S_A(n)$ have global averages of 64 and 236 W/m^2 (the latter corresponding to $T_A = 254$ K), respectively. In the earlier noncellular model,[9] the highest value of S_{NR} that could be obtained without unreasonable parameters was 40 W/m^2, and in the above T_E-predictive mode it was 42.3 W/m^2, so the S_{NR}-predictive mode result 64 W/m^2 represents a further improvement. The generally quoted global average of S_{NR} is 102 to 105 W/m^2.[16,17] $S_{NR}(n)$ appears to be most negative at the higher latitudes and most positive near the

equator. A negative value of $S_{NR}(n)$ corresponds to nonradiative energy transfer from the atmospheric layer to the surface layer or a lateral flow into the cell, as discussed earlier.

A distinctive feature of our results is the prominent drop of S_{NR} in the regions of the Sahara and Saudi Arabia [Fig. 94.67(a), at matrix elements (20–25, 14–16)]. Its cause is a confluence of strong effects on the two terms in Eq. (12): relatively high surface reflectivity and low cloud cover, which reduce the first term, and relatively high temperature, which increases the absolute value of the (negative) second

Figure 94.67
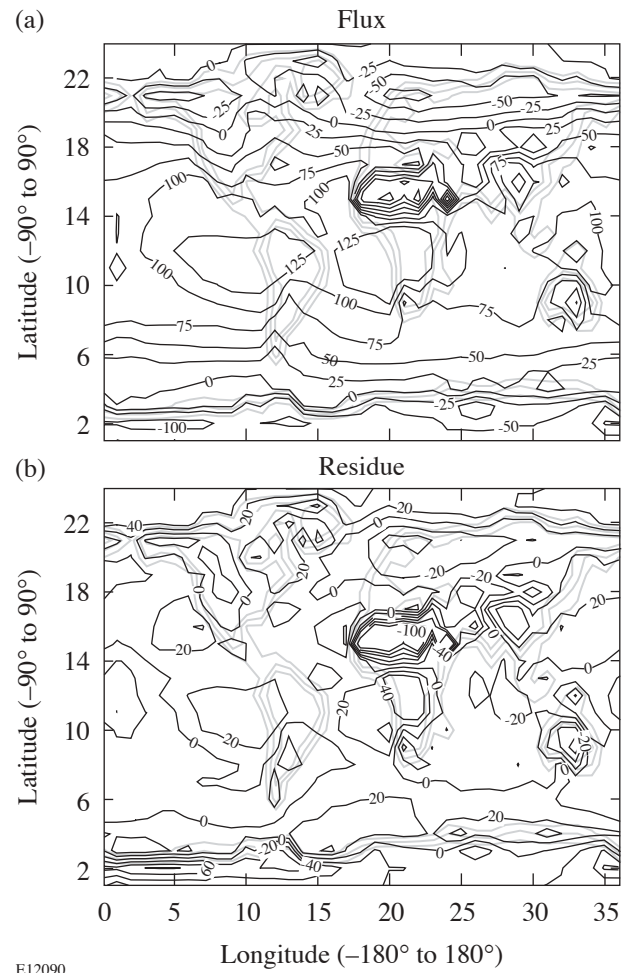(a) Computed "S_{NR}-predictive mode" nonradiative flux $S_{NR}(n)$ (in W/m^2) using the cellular model but with surface temperatures as input. (b) $\delta S_{NR}(n)$, the residue after subtracting the annual average value of $S_{NR}(n)$ as a function of latitude [see Eq. (16)]. The one region of large residuals corresponds to the Sahara desert region. (See the caption of Fig. 94.64 for the key to the axes.)

term. A similar but milder dip appears in the eastern region of Australia.

Figures 94.67 and 94.68 reveal a possible smooth dependence of $S_{NR}(n)$ on latitude. Figure 94.67(b) shows the residues $\delta S_{NR}(n)$ after latitude averages are removed, as discussed in the next section.

3. The Zonal Average of S_{NR}

"Zonal" averages are made over cells lying within zones having the same latitude. Following convention,[18] we denote zonal averages by angular brackets $\langle...\rangle$. If the area of cell $n = (p,q)$ is $A(p,q)$, where p is the latitude cell index and q is the longitude cell index, we have, for example,

$$\langle S_{NR}(p)\rangle = \frac{1}{A(p)}\sum_q A(p,q)S_{NR}(p,q), \qquad (14)$$

where $A(p)$ is the total area of zone p,

$$A(p) = \sum_q A(p,q). \qquad (15)$$

For convenience the latitude index p will be converted into the latitude β, measured in degrees, at the center of the cell and we will write, again for example, $S_{NR}(\beta) = \langle S_{NR}(p)\rangle$.

The zonal averages $S_{NR}(\beta)$ are shown explicitly in Fig. 94.68, where a very regular latitude dependence emerges clearly. Indeed, $S_{NR}(\beta)$ can be represented to within ± 9 W/m^2 by

$$S_{NR}^{fit}(\beta) = 40 + 80\cos 2(\beta + \Delta) - 10\sin 6|\beta|, \qquad (16)$$

with $\Delta = 5°$. In Fig. 94.68 the residuals between $S_{NR}(\beta)$ and its fit are also shown. When this zonal average is removed from the cellular results of Fig. 94.67(a), the residuals [Fig. 94.67(b)] are obtained. They are noteworthy for their general smoothness and for their relatively small size, which is of the order of 5%–10% of the solar input at the surface.

It is not surprising that $S_{NR}(\beta)$ has an asymmetry between the northern and southern hemispheres. In retrospect we see that the *ad hoc* form, Eq. (11), used in the T_E-predictive calculation, was biased toward the southern hemisphere, where
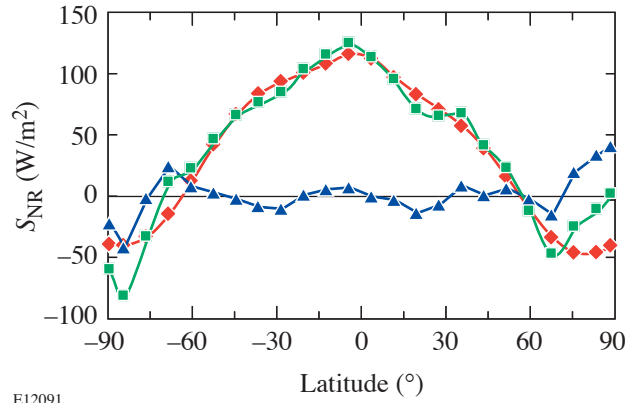

Figure 94.68
Distribution of S_{NR} by latitude. Squares represent the "experimental" values based on our model, and diamonds are the numerical fit, Eq. (16). Triangles are the residuals.

the sea fraction is dominant. Figure 94.69 shows the 18-year-average surface reflectivity in months 1 and 7 (Ref. 10), giving further insight into the peculiarities of S_{NR}. The reflectivities are slightly higher in the northern temperate zone than in the southern. In the polar regions, the times of greater solar irradiance may not occur when the surface reflectance is at its average value. Indeed, the polar regions are generally rather anomalous. We have not concerned ourselves too much with them because the model, generally limited to dealing with annual averages, lacks the ability to describe accurately the effect of Arctic and Antarctic nights in which $S_0(n) = 0$. There is some seasonal variation in the cloud cover data, which may be responsible for the fact that the interesting term $-10\sin 6|\beta|$ does not hold in the polar regions. One is tempted to speculate on the origin of the sinusoidal term: the insolation does not have a pure $\cos\beta$ dependence because of the inclination of Earth's axis to the plane of its orbit, and Hadley cells[19] may play a role in it.

The existence of extensive databases provides the student an opportunity to explore many other effects through the medium of this theory. As an example, we have used data from ISCCP[14] consisting of averages of the measured parameters at each month over an 18-year period. For each month, the average $S_{NR}(\beta,t)$ was calculated and compared to $S_{NR}(\beta)$ by looking at the difference between the two. This difference also appears to follow a trend that is most clear in the region between latitudes $-60°$ and $+60°$. For this region the difference is approximately linear and oscillates about $\beta = 0°$ with a period of one year. The difference itself can be fitted well to

$$\Delta S_{\mathrm{NR}}(\beta, t) = -285 \cdot (\beta/60°) \cdot \sin(30°t) \qquad (17)$$

(where $t = 0$, September 15; $t = 1$, October 15; etc.).

Now, we have shown that the annual average S_{NR} follows Eq. (16), and the difference between monthly and annual values follows Eq. (17), so the monthly S_{NR} can be written as

$$S_{\mathrm{NR}}^{\mathrm{fit}}(\beta, t)$$

$$= 40 + 80 \cos 2(\beta + \Delta) - 10 \sin 6|\beta| + \Delta S_{\mathrm{NR}}(\beta, t) \qquad (18)$$

in the specified region $-60° \le \beta \le +60°$. For the month of January, the values of S_{NR} calculated directly from the data are compared to those given by Eq. (18) in Fig. 94.70. The fitting is very close to the calculated values in the region $-30° \le \beta \le +45°$. The discrepancies of up to 50 W/m^2 outside this region are most likely due to the hemispheric asymmetry of S_{NR}. This asymmetry was ignored in Eq. (17), which is antisymmetric about $\beta = 0°$ and uses a perfectly sinusoidal maximum value for $\beta = \pm 60°$. The calculations from data, however, show that during the southern summer, $S_{\mathrm{NR}}(-60°, t)$ increases to close to 400 W/m^2, but in the northern summer $S_{\mathrm{NR}}(+60°, t)$ does not even reach 300 W/m^2. Also, at any month, the value of $S_{\mathrm{NR}}(60°, t)$ does not equal $S_{\mathrm{NR}}(-60°, t)$, as in Eq. (17), leading to an over- or underestimation of S_{NR} from Eq. (18).

(a) January

(b) July
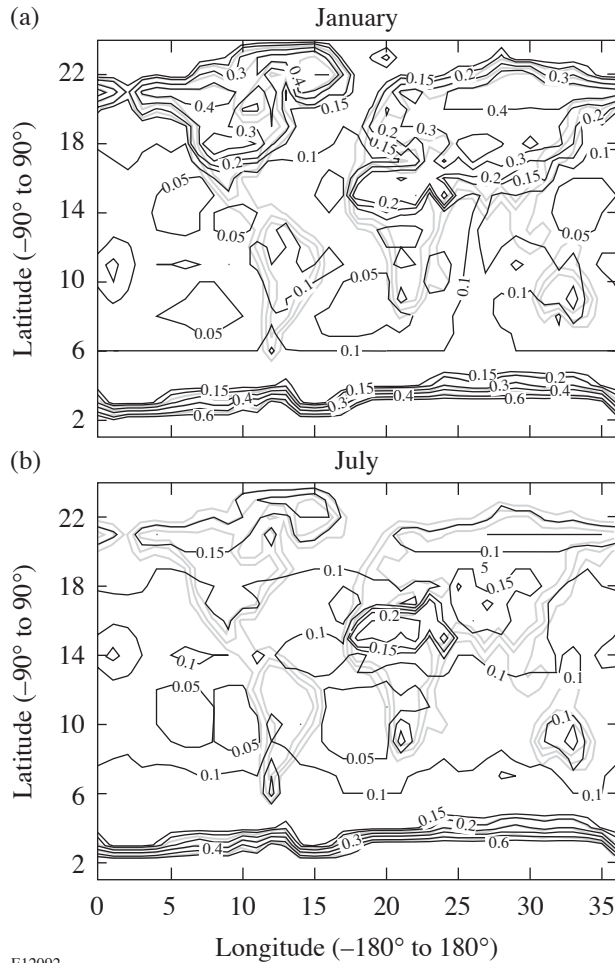
Figure 94.69
Comparison of surface reflectivities in the months of January (a) and July (b). The asymmetry between the northern and southern hemispheres seen in many climatological studies can be appreciated from the variability in the north polar region and the near-invariance in the south polar region. (See the caption of Fig. 94.64 for the key to the axes.)

E12092

E12093
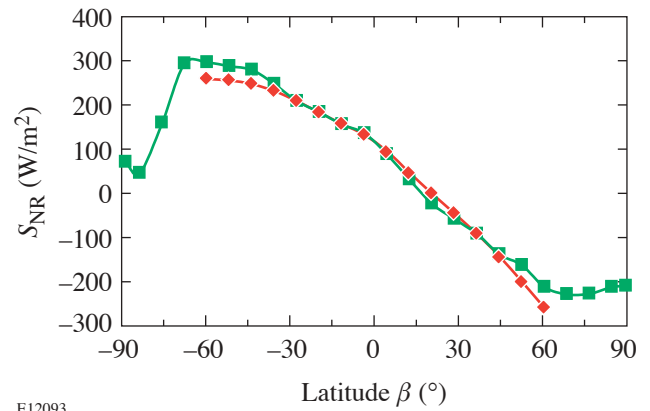
Figure 94.70
A sample determination of nonradiative flux S_{NR} for the month of January (18-year average). Diamonds: values determined from our model calculation. Squares: values determined from the fitting function, Eq. (18). The fit is meant to be valid for latitudes satisfying $-60° \le \beta \le +60°$.

Finally, in Fig. 94.71 we compare averages of S_{NR} over two months in succession (February and March 1995). The 18-year average for the respective months has been subtracted, and the polar regions have been omitted from the diagram because average monthly variations in reflectivities and cloud cover

(a)

February 1995

(b)

March 1995

E12095

Figure 94.71

(a) The monthly values of S_{NR} for February 1995 minus the 18-year average value of S_{NR} for February, for the temperate zones. Large deviations, ~50 W/m^2, in large-scale "weather" patterns are seen. (b) Similar to (a), for March 1995. Comparing with February, it can be seen that some nonradiative "weather cells" (indicated by shading) persist for at least a month and some (indicated by stippling) are more ephemeral. The largest features cover 10 to 20 cells, each computed independently.

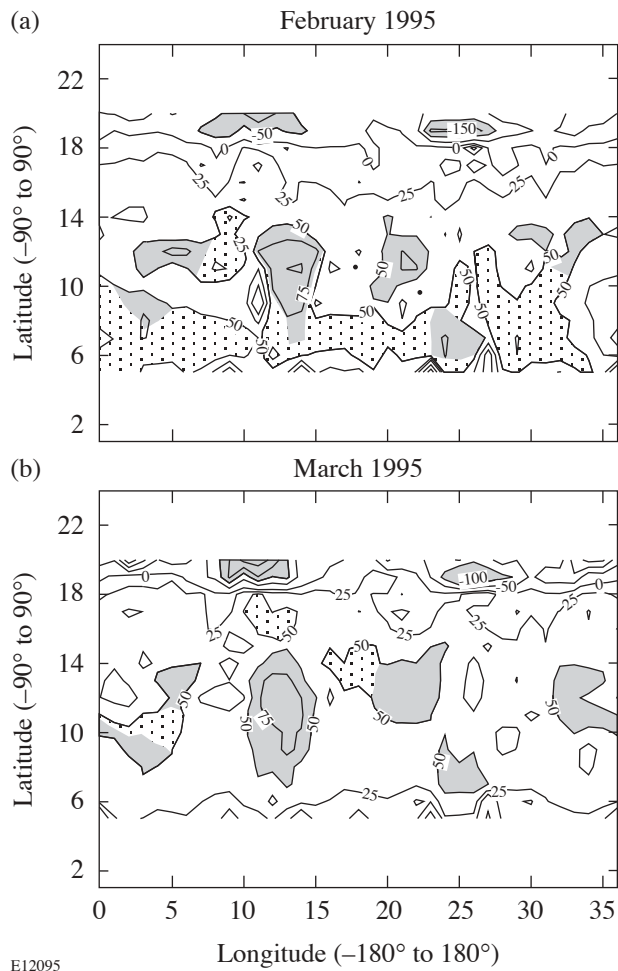may be large. Deviations of the order of 50 W/m^2 show the presence of large-scale, persistent nonradiative "weather systems," each of which is composed of about 20 independent cells. These systems produce deviations in S_{NR} much larger than those shown in Fig 94.67(b). The figures serve to illustrate east–west nonradiative energy transport. Only when averages are taken over the 18-year database do the smooth results given by Eqs. (17) and (18) and Figs. 94.68 and 94.70 result.

Summary and Discussion

The two-level global model of Ref. 9 has been applied locally; that is, each cell in a grid has been assumed to have annual average temperatures and the fluxes have been determined by the cell's own parameters and average insolation. The observed local planetary albedo is used as a control on the modeled surface and atmospheric reflectivities. In the model's more successful (S_{NR}-predictive) implementation, the set of surface temperatures is used as input; the nonradiative flux from the surface S_{NR} and the ideal atmospheric radiative flux S_A are the principal outputs. The globally averaged S_{NR} is predicted to be about 64% of its usually quoted global value of 102 to 105 W/m^2, an improvement over T_E-predictive models using assumed nonradiative fluxes, where values of only 0%–40% were possible.

The value of the globally averaged atmospheric radiative flux S_A is 236 W/m^2, adequate to maintain overall radiative balance with an effective atmospheric radiative temperature of $T_A = 254$ K (recall that the emissivity is taken as 0.89, as in Ref. 9). Since our model assigns only this one temperature to the atmosphere, it is constrained to predict that the downward IR flux is identical to the upward flux. In the real atmosphere, a temperature gradient exists and the lower layers most effective in radiating downward are at a higher temperature. The downward flux should thus be greater than εS_A, as is observed.[18] We are developing a three-temperature version of our model, to be the subject of a future article in the series, and according to preliminary estimates, an appropriately larger value of S_{NR} will be obtained that will balance the extra downward IR.

Having noted a correlation between $S_{NR}(n)$ and latitude, we examined its zonal average. A clear asymmetry resulted between the northern and southern hemispheres, illustrating the effect of asymmetry of the hemispheric land masses and the differences in reflectivity parameters resulting from the nature of the Arctic and Antarctica. Fittings of other data sets to develop formulae for individual components of S_{NR} are discussed by Budyko.[5]

We emphasize the accessibility of both the data and our model representations to students interested in applying the elementary aspects of climatology to real data. As suggestions for future workers: (1) It would be interesting to use databases averaged over different periods of time to see if long-term differences in the form of Eqs. (17) and (18) result. (2) A study of the form, structure, and persistence of these large-scale

monthly "weather patterns" during an El Niño cycle should be informative.

Appendix A: Spherical Astronomy Fundamentals

The altitude H of the sun can be found by applying the law of cosines[20] to the observer's spherical triangle ΔZNS, where Z is the observer's zenith, N is the north celestial pole, and S is the sun. Then arc ZS is $90°-H$; arc NZ is $90°-\beta$, where β is the latitude; and arc NS is $90°-\delta$, where δ is the *declination* of the sun, available from a table lookup in, e.g., Ref. 21.

List of symbols and abbreviations. [Note: symbols of the form $T_A(n)$ are not included. The meaning of such a symbol is "the value of T_A in cell n."]

A	UV atmospheric input parameter [Eq. 2(a)]		r_{sea}	Reflectivity of the sea portion of a cell
$A(p)$	Area of a band of cells of latitude index p		S_0	Solar constant averaged globally and over time, 342 Wm^{-2}
$A(p,q)$	Area of a cell of latitude index p and longitude index q		S_A	Ideal radiative flux in the atmosphere or upper atmosphere layer, σT_A^4
a	Atmosphere's absorptivity in the UV		S_E	Ideal radiative flux in the surface layer, σT_E^4
a_{clear}	Absorptivity of cloudless air in the UV		S_{NR}	Net nonradiative flux upward from the surface
a_{cloud}	Absorptivity of air with clouds in the UV		t	Solar hour angle (see Appendix)
B	UV surface input parameter [Eq. 2(b)]		T'	Time elapsed since the vernal equinox
f_{cloud}	Fraction (of a cell area) consisting of cloud		T_A	Effective radiative temperature of the upper model layer, representing that of the atmosphere
f_{land}	Fraction (of a cell area) consisting of land		T_E	Temperature of the lower model layer, representing that of the surface of Earth
H	Horizon angle of the sun		UV	Refers to that part of the spectrum of the sun that is absorbed by the atmosphere; roughly wavelengths shorter than 600 nm
IR	Refers to that part of the spectrum with wavelengths longer than 600 nm; largely not absorbing the sun's spectrum but absorbing much of Earth's		α_P	Planetary albedo
k_M	Multiple reflection parameter		β	Latitude associated with a set of cells
n	Cell label, also in matrix style p, q		δ	Solar declination angle
p, q	Latitude and longitude cell indexes, respectively		Δ	Fitting parameter (phase shift); see **Summary and Discussion**.
r_A	Reflectivity of the atmosphere in the UV		ε	Atmosphere's absorptivity (and emissivity) in the IR
r_{clear}	Reflectivity of clear air		$\varepsilon_{\text{clear}}$	Clear air absorptivity (and emissivity) in the IR
r_{cloud}	Reflectivity of the cloud portion of a cell		$\varepsilon_{\text{cloud}}$	Cloud absorptivity (and emissivity) in the IR
r_{land}	Reflectivity of the land portion of a cell		σ	Stefan–Boltzmann constant, 5.67×10^{-8} Wm^{-2} K^{-4}
r_S	Reflectivity of the surface in the UV			

The angle ∠*SNZ* is called the sun's *hour angle H*; instead of being measured in degrees, it is measured in time units from 12:00 noon (1 h = 15°). It is negative (positive) when the sun is in the eastern (western) half of the sky. These quantities are related by the spherical law of cosines:

$$\sin H = \sin \beta \, \sin \delta + \cos \beta \, \cos \delta \, \cos t, \qquad (A1)$$

At sunrise, $H = 0$; the equation determines the time at sunrise $t = -t_0$. At sunset, again $H = 0$ and $t = +t_0$. The length of daylight is then $2t_0$.

The declination of the sun can also be approximated. The sun moves along a great circle, called the *ecliptic*, which is inclined at an angle $i = 23.44°$ to the celestial equator. At the vernal equinox (~March 21) the sun is at a point *V*, one of the two intersections of the celestial equator and the ecliptic, and is moving from negative to positive declination. Let the point *P* be on the celestial equator, with arc *NSP* = 90°. Consider the spherical triangle *VSP*. The angle ∠*SVP* = *i* and the angle ∠*SPV* = 90°. The arc *VS* is *approximately* $\Omega t'$, where $\Omega = 360°/1$ yr and t' is the time elapsed since the vernal equinox. From the spherical law of sines for *VSP* one has

$$\sin \delta = \sin i \, \sin \Omega'. \qquad (A2)$$

Since the sun moves slightly faster (slower) on the ecliptic than average when we are at perihelion, January (aphelion, July), this is only an approximate relation.

REFERENCES

1. J. Hansen *et al.*, Proc. Natl. Acad. Sci. USA **97**, 9875 (2000).

2. D. L. Hartmann, *Global Physical Climatology*, International Geophysics, Vol. 56 (Academic Press, San Diego, 1994).

3. J. P. Peixoto and A. H. Oort, *Physics of Climate* (American Institute of Physics, New York, 1992).

4. M. I. Budyko, Tellus **21**, 611 (1969).

5. M. I. Budyko, *The Earth's Climate, Past and Future*, International Geophysics Series, Vol. 29 (Academic Press, New York, 1982).

6. K. E. Trenberth, J. M. Caron, and D. P. Stepaniak, Clim. Dyn. **17**, 259 (2001).

7. K. E. Trenberth and J. M. Caron, J. Clim. **14**, 3433 (2001).

8. C. Kittle and H. Kroemer, *Thermal Physics*, 2nd ed. (W. H. Freeman, San Francisco, 1980), pp. 115–116.

9. R. S. Knox, Am. J. Phys. **67**, 1227 (1999).

10. S. Arrhenius, Phil. Mag. **41**, 237 (1896).

11. J. R. Barker and M. H. Ross, Am. J. Phys. **67**, 1216 (1999).

12. J. Hansen *et al.*, Mon. Weather Rev. **111**, 609 (1983).

13. G. J. Borse, *Numerical Methods with MATLAB®: A Resource for Scientists and Engineers* (PWS Publishing, Boston, 1997).

14. C. Brest (technical contact), "ISCCP D2 Monthly Means and Climatology," data sets retrieved 21 January 2002 from the International Satellite Cloud Climatology Project, available at http://isccp.giss.nasa.gov/products/browsed2.html.

15. The ISCCP data for r_S was not used in regions above ±52° latitude because the data sometimes are greater than unity as a result of glaring and the angle of the satellite to the northern and southern polar regions. This being inconsistent with our definition of a reflection coefficient, the surface reflectivities in these regions were estimated from the Hartmann[2] Table 4.2.

16. J. T. Kiehl and K. E. Trenberth, Bull. Am. Meteorol. Soc. **78**, 197 (1997).

17. See M. I. Budyko, *The Earth's Climate, Past and Future*, International Geophysics Series, Vol. 29 (Academic Press, New York, 1982), p. 70.

18. R. E. Dickinson, in *Climate System Modeling*, edited by K. E. Trenberth (Cambridge University Press, Cambridge, England, 1992), Chap. 5, pp. 149–171.

19. See D. L. Hartmann, *Global Physical Climatology*, International Geophysics, Vol. 56 (Academic Press, San Diego, 1994), pp. 152–154.

20. W. M. Smart, *Text-Book on Spherical Astronomy* (Cambridge University Press, Cambridge, England, 1947).

21. R. Gupta, ed. *Observer's Handbook* (The Royal Astronomical Society of Canada, Toronto, 2002).

Publications and Conference Presentations

Publications

G. P. Agrawal and D. N. Maywar, "Semiconductor Optical Amplifiers with Bragg Gratings," in *Nonlinear Photonic Crystals*, edited by R. E. Slusher and B. J. Eggleton, Springer Series in Photonics, Vol. 10 (Springer-Verlag, Berlin, 2003), Chap. 13, pp. 285–300.

G. Chen, Y. Du, S. Wang, A. E. Marino, L. L. Gregg, S. R. Arrasmith, and S. D. Jacobs, "Effect of SnO on Chemical Durability of Phosphate Glasses," Glass Technol. **43C**, 97 (2002).

Y. Geng, S. W. Culligan, A. Trajkovska, J. U. Wallace, and S. H. Chen, "Monodisperse Oligofluorenes Forming Glassy-Nematic Films for Polarized Blue Emission," Chem. Mater. **15**, 542 (2003).

V. Yu. Glebov, C. Stoeckl, T. C. Sangster, D. D. Meyerhofer, P. B. Radha, S. Padalino, L. Baumgart, R. Coburn, and J. Fuschino, "Carbon Activation Diagnostic for Tertiary Neutron Measurements," Rev. Sci. Instrum. **74**, 1717 (2003).

O. V. Gotchev, P. A. Jaanimagi, J. P. Knauer, F. J. Marshall, D. D. Meyerhofer, N. Bassett, and J. B. Oliver, "High-Throughput, High-Resolution, Kirkpatrick–Baez Microscope for Advanced Streaked Imaging of ICF Experiments on OMEGA," Rev. Sci. Instrum. **74**, 2178 (2003).

Q. Guo, X. Teng, S. Rahman, and H. Yang, "Patterned Langmuir–Blodgett Films of Monodisperse Nanoparticles of Iron Oxide Using Soft Lithography," J. Am. Chem. Soc. **125**, 630 (2003).

R. D. Petrasso, J. A. Frenje, C. K. Li, F. H. Séguin, J. R. Rygg, B.-E. Schwartz, S. Kurebayashi, P. B. Radha, C. Stoeckl, J. M. Soures, J. A. Delettrez, V. Yu. Glebov, D. D. Meyerhofer, and T. C. Sangster, "Measuring Implosion Dynamics through ρR Evolution in Inertial Confinement Fusion Experiments," Phys. Rev. Lett. **90**, 095002 (2003).

F. H. Séguin, J. A. Frenje, C. K. Li, D. G. Hicks, S. Kurebayashi, J. R. Rygg, B.-E. Schwartz, R. D. Petrasso, S. Roberts, J. M. Soures, D. D. Meyerhofer, T. C. Sangster, J. P. Knauer, C. Sorce, V. Yu. Glebov, C. Stoeckl, T. W. Phillips, R. J. Leeper, K. Fletcher, and S. Padalino, "Spectrometry of Charged Particles from Inertial Confinement Fusion Plasmas," Rev. Sci. Instrum. **74**, 975 (2003).

V. A. Smalyuk, S. B. Dumanis, F. J. Marshall, J. A. Delettrez, D. D. Meyerhofer, S. P. Regan, T. C. Sangster, B. Yaakobi, and J. A. Koch, "Radial Structure of Shell Modulations Near Peak Compression of Spherical Implosions," Phys. Plasmas **10**, 830 (2003).

C. Stoeckl, V. Yu. Glebov, S. Roberts, T. C. Sangster, R. A. Lerche, R. L. Griffith, and C. Sorce, "Ten-Inch Manipulator-Based Neutron Temporal Diagnostic for Cryogenic Experiments on OMEGA," Rev. Sci. Instrum. **74**, 1713 (2003).

F.-Y. Tsai, D. R. Harding, S. H. Chen, and T. N. Blanton, "High-Permeability Fluorinated Polyimide Microcapsules by Vapor-Deposition Polymerization," Polymer **44**, 995 (2003).

B. Yaakobi, F. J. Marshall, T. R. Boehly, R. P. J. Town, and D. D. Meyerhofer, "Extended X-Ray Absorption Fine Structure Experiments Using a Laser-Imploded Target as a Radiation Source," J. Opt. Soc. Am. B **20**, 238 (2003).

X. Zheng, Y. Xu, R. Sobolewski, R. Adam, M. Mikulics, M. Siegel, and P. Kordos, "Femtosecond Response of a Free-standing LT-GaAs Photoconductive Switch," Appl. Opt. **42**, 1726 (2003).

Forthcoming Publications

A. Babushkin, M. J. Harvey, and M. D. Skeldon, "The Output Signal-to-Noise Ratio of a Nd:YLF Regenerative Amplifier," to be published in Applied Optics.

G. N. Gol'tsman, K. Smirnov, P. Kouminov, B. Voronov, N. Kaurova, V. Drakinsky, J. Zhang, A. Verevkin, and R. Sobolewski, "Fabrication of Nanostructured Superconducting Single-Photon Detectors," to be published in IEEE Transactions on Applied Superconductivity.

V. N. Goncharov, J. P. Knauer, P. W. McKenty, T. C. Sangster, S. Skupsky, R. Betti, R. L. McCrory, and D. D. Meyerhofer, "Improved Performance of Direct-Drive ICF Target Designs with Adiabat Shaping Using an Intensity Picket," to be published in Physics of Plasmas (invited).

C. K. Li, F. H. Séguin, J. A. Frenje, S. Kurebayashi, J. R. Rygg, B. E. Schwartz, R. D. Petrasso, R. L. Keck, J. A. Delettrez, P. W. McKenty, F. J. Marshall, D. D. Meyerhofer, P. B. Radha, T. C. Sangster, J. M. Soures, and C. Stoeckl, "Capsule Areal-Density Asymmetries and Time Evolution Inferred from 14.7-MeV Proton Line Structure in OMEGA D^{3}He Implosions," to be published in Physics of Plasmas (invited).

D. L. McCrorey, R. C. Mancini, V. A. Smalyuk, S. P. Regan, and B. Yaakobi, "Spectroscopic Determination of Compressed-Shell Conditions in OMEGA Implosions Based on Ti K-Shell Line Absorption Analysis," to be published in Review of Scientific Instruments.

R. L. McCrory, D. D. Meyerhofer, R. Betti, T. R. Boehly, R. S. Craxton, T. J. B. Collins, J. A. Delettrez, R. Epstein, V. Yu. Glebov, V. N. Goncharov, D. R. Harding, R. L. Keck, J. H. Kelly, J. P. Knauer, S. J. Loucks, L. Lund, J. A. Marozas, P. W. McKenty, F. J. Marshall, S. F. B. Morse, P. B. Radha, S. P. Regan, S. Roberts, W. Seka, S. Skupsky, V. A. Smalyuk, C. Sorce, C. Stoeckl, J. M. Soures, R. P. J. Town, B. Yaakobi, J. A. Frenje, C. K. Li, R. D. Petrasso, F. H. Séguin, K. Fletcher, S. Padalino, C. Freeman, and C. Sangster, "Direct-Drive Inertial Confinement Fusion Research at the Laboratory for Laser Energetics," to be published in the proceedings of *Current Trends in International Fusion Research: A Review*.

R. L. McCrory, D. D. Meyerhofer, S. J. Loucks, S. Skupsky, R. E. Bahr, R. Betti, T. R. Boehly, R. S. Craxton, T. J. B. Collins, J. A. Delettrez, W. R. Donaldson, R. Epstein, J. A. Frenje, V. Yu. Glebov, V. N. Goncharov, D. R. Harding, P. A. Jaanimagi, R. L. Keck, J. H. Kelly, T. J. Kessler, J. P. Knauer, C. K. Li, L. D. Lund, J. A. Marozas, P. W. McKenty, F. J. Marshall, S. F. B. Morse, R. D. Petrasso, P. B. Radha, S. P. Regan, S. Roberts, T. C. Sangster, F. H. Séguin, W. Seka, V. A. Smalyuk, C. Sorce, J. M. Soures, C. Stoeckl, R. P. J. Town, B. Yaakobi, and J. D. Zuegel, "Progress in Direct-Drive Inertial Confinement Fusion Research at the Laboratory for Laser Energetics," to be published in Nuclear Fusion.

S. Papernov and A. W. Schmid, "Damage Behavior of SiO$_2$ Thin Films Containing Gold Nanoparticles Lodged on a Predetermined Distance from the Film Surface," to be published in the *Proceedings of the XXXIV Annual Symposium on Optical Materials for High Power Lasers*.

T. C. Sangster, J. A. Delettrez, R. Epstein, V. Yu. Glebov, V. N. Goncharov, D. R. Harding, J. P. Knauer, R. L. Keck, J. D. Kilkenny, S. J. Loucks, L. D. Lund, R. L. McCrory, P. W. McKenty, F. J. Marshall, D. D. Meyerhofer, S. F. B. Morse, S. P. Regan, P. B. Radha, S. Roberts, W. Seka, S. Skupsky, V. A. Smalyuk, C. Sorce, J. M. Soures, C. Stoeckl, K. A. Thorp, J. A. Frenje, C. K. Li, R. D. Petrasso, F. H. Séguin, K. A. Fletcher, S. Padalino, C. Freeman, N. Izumi, J. A. Koch, R. A. Lerche, M. J. Moran, T. W. Phillips, and G. J. Schmid, "Direct-Drive Cryogenic Target Implosion Performance on OMEGA," to be published in Physics of Plasmas (invited).

V. A. Smalyuk, J. A. Delettrez, V. Yu. Glebov, V. N. Goncharov, J. P. Knauer, F. J. Marshall, D. D. Meyerhofer, P. B. Radha, S. P. Regan, T. C. Sangster, S. Skupsky, J. M. Soures, C. Stoeckl, R. P. J. Town, B. Yaakobi, J. A. Frenje, C. K. Li, R. D. Petrasso, F. H. Séguin, D. L. McCrorey, and R. C. Mancini, "Hydrodynamic Growth of Shell Modulations in the Deceleration Phase of Spherical Direct-Drive Implosions," to be published in Physics of Plasmas (invited).

V. A. Smalyuk, P. B. Radha, J. A. Delettrez, V. Yu. Glebov, V. N. Goncharov, D. D. Meyerhofer, S. P. Regan, S. Roberts, T. C. Sangster, J. M. Soures, C. Stoeckl, J. A. Frenje, C. K. Li, R. D. Petrasso, and F. H. Séguin, "Time-Resolved Areal-Density Measurements with Proton Spectroscopy in Spherical Implosions," to be published in Physical Review Letters.

R. Sobolewski, A. Verevkin, G. N. Gol'tsman, A. Lipatov, and K. Wilsher, "Ultrafast Superconducting Single-Photon Optical Detectors and Their Applications," to be published in IEEE Transactions on Applied Superconductivity.

A. Sunahara, J. A. Delettrez, C. Stoeckl, R. W. Short, and S. Skupsky, "Time-Dependent Electron-Thermal-Flux Inhibition in Direct-Drive Laser Implosion," to be published in Physical Review Letters.

F.-Y. Tsai, T. N. Blanton, D. R. Harding, and S. H. Chen, "Temperature Dependency of the Properties of Vapor-Deposited Polyimide," to be published in the Journal of Applied Physics.

Y. Xu, M. Khafizov, A. Plecenik, P. Kús, L. Satrapinsky, and R. Sobolewski, "Femtosecond Optical Characterization of MgB_2 Superconducting Thin Films," to be published in IEEE Transactions on Applied Superconductivity.

J. Zhang, W. Slysz, A. Verevkin, R. Sobolewski, O. Okunev, G. Chulkova, A. Lipatov, and G. N. Gol'tsman, "Time Delay of the Resistive-State Formation in Superconducting NbN Stripes Excited by Single Optical Photons," to be published in Physical Review B.

J. Zhang, W. Slysz, A. Verevkin, O. Okunev, G. Chulkova, A. Korneev, A. Lipatov, G. N. Gol'tsman, and R. Sobolewski, "Response-Time Characterization of NbN Superconducting Single-Photon Detectors," to be published in IEEE Transactions on Applied Superconductivity.

X. Zheng, S. Wu, R. Sobolewski, R. Adam, M. Mikulics, P. Kordos, and M. Siegel, "Electro-Optic Sampling System with a Single-Crystal 4-N, N-Dimethylamino-4′-N′-Methyl-Stilbazolium Tosylate Sensor," to be published in Applied Physics Letters.

Conference Presentations

S. D. Jacobs, "Innovations in Polishing of Precision Optics," EOS 2003 International Workshop on Extreme Optics and Sensors, Tokyo, Japan, 14–17 January 2003 (invited).

———

J. Li, W. R. Donaldson, and T. Y. Hsiang, "Very Fast Metal–Semiconductor–Metal Ultraviolet Photodetectors on GaN with Submicron Finger Width," Ultrafast Electronics and Optoelectronics, Washington, DC, 15–17 January 2003.

———

I. A. Begishev, V. Bagnoud, M. J. Guardalben, L. J. Waxer, J. Puth, and J. D. Zuegel, "Optimization of an Optical Parametric Chirped-Pulse Amplification System for the OMEGA EP Laser System," 2003 Advanced Solid-State Photonics, San Antonio, TX, 2–5 February 2003.

———

The following presentations were made at the 5th International Workshop on Laser Plasma Interaction Physics, Banff, Alberta, Canada, 19–22 February 2003:

W. Seka, H. Baldis, S. Depierreux, R. S. Craxton, S. P. Regan, C. Stoeckl, and R. W. Short, "Experimental Observations of the Landau Cutoff for Electron Plasma Waves Driven by the TPD Instability."

R. W. Short, "On the Role of Electron-Acoustic Waves in Two-Plasmon Decay."

———

C. Dorrer and D. N. Maywar, "800-GHz RF Spectrum Analyzer for Optical Signals," Optical Fiber Communication, Atlanta, GA, 23–28 March 2003.

———

R. L. McCrory, D. D. Meyerhofer, S. J. Loucks, S. Skupsky, R. E. Bahr, R. Betti, T. R. Boehly, R. S. Craxton, T. J. B. Collins, J. A. Delettrez, W. R. Donaldson, R. Epstein, J. A. Frenje, V. Yu. Glebov, V. N. Goncharov, D. R. Harding, P. A. Jaanimagi, R. L. Keck, J. H. Kelly, T. J. Kessler, J. D. Kilkenny, J. P. Knauer, C. K. Li, L. D. Lund, J. A. Marozas, P. W. McKenty, F. J. Marshall, S. F. B. Morse, R. D. Petrasso, P. B. Radha, S. P. Regan, S. Roberts, T. C. Sangster, F. H. Séguin, W. Seka, V. A. Smalyuk, J. M. Soures, C. Stoeckl, K. A. Thorp, B. Yaakobi, and J. D. Zuegel, "Direct-Drive Inertial Fusion Research at the University of Rochester's Laboratory for Laser Energetics: A Review," 5th Symposium of the Current Trends in International Fusion Research: A Review, Washington, DC, 24–28 March 2003.

The following presentations were made at the Workshop on Experience in the Management of Wastes from Fusion Facilities, Abington, United Kingdom, 25–26 March 2003:

W. T. Shmayda, "Recovery and Enrichment of Tritium from Organic and Aqueous Liquid Waste Streams."

W. T. Shmayda, "Metal Decontamination."

S. G. Lukishova, A. W. Schmid, A. J. McNamara, R. W. Boyd, and C. R. Stroud, "Dye-Doped Cholesteric-Liquid-Crystal Single Photon Source," NIST Workshop on Single Photon Detectors, Applications, and Measurement Methods, Gaithersburg, MD, 31 March–1 April 2003.